

Technische Universität München  
Fakultät für Physik  
Max-Planck-Institut für Plasmaphysik (IPP)

## **Study of the Sawtooth Instability and its Control in the ASDEX Upgrade Tokamak**

**Anja Maria Mück**

Vollständiger Abdruck der von der Fakultät für Physik  
der Technischen Universität München  
zur Erlangung des akademischen Grades eines  
Doktors der Naturwissenschaften (Dr.rer.nat.)  
genehmigten Dissertation.

Vorsitzender: Univ.-Prof. Dr. H. Friedrich

Prüfer der Dissertation: 1. Hon.-Prof. Dr. R. Wilhelm  
2. Univ.-Prof. Dr. K. Krischer

Die Dissertation wurde am 11.12.2003 bei der  
Technischen Universität München eingereicht und  
durch die Fakultät für Physik am 26.02.2004 angenommen.

# Zusammenfassung

Der nächste grosse Schritt in der Fusionsforschung ist der Bau von ITER, dem internationalen Thermonuklearen Experiment Reaktor in Internationaler Zusammenarbeit. Mit ITER soll gezeigt werden, dass ein Fusionskraftwerk realisiert werden kann. Die Fusionsrate wird wesentlich höher sein als in den derzeitigen Experimenten. Durch die höhere Anzahl von Fusionsprozessen wird auch die Anzahl der Fusionsprodukte ansteigen. Ein Fusionsprodukt ist das  $\alpha$ -Teilchen, ein schnelles Ion. Es ist bekannt, dass schnelle Teilchen einen stabilisierenden Einfluss auf die sogenannte Sägezahninstabilität ausübt. Unter einem Sägezahn versteht man ein langsames Anwachsen der zentralen Plasmatemperatur gefolgt von einem schnellen Zusammenbruch. Anschliessend erholt sich das Plasma, die Temperatur steigt erneut, bis sie einbricht. Die Zeit zwischen zwei Einbrüchen nennt man Sägezahnperiode. Auf der einen Seite können Sägezähne von Nutzen sein beim Transport von Heliumasche und Verunreinigungen aus dem Plasmazentrum, auf der anderen Seite wird Energie aus dem Plasmazentrum ausgeworfen und damit der zentrale Druck limitiert. Zusätzlich dienen Sägezähne als sogenannte Saatinseln für eine weitere Plasmainstabilität, die Neoklassische Tearingmode (NTM), welche zu einer Verschlechterung des Plasmaeinschlusses führt. Durch die Stabilisierung der Sägezähne, das heisst durch Verlängerung der Sägezahnperiode, durch die  $\alpha$ -Teilchen werden große Sägezähne erwartet. Dies ist im Hinblick auf Stationarität unerwünscht.

Die Soft X-Ray Diagnostik (SXR), die weiche Röntgenstrahlen misst, ist ein wichtiges Hilfsmittel zur Untersuchung von Sägezähnen, da das Plasma aufgrund seiner hohen Temperatur in diesem Bereich strahlt. Ein Umbau und die Entwicklung eines neuen SXR Systems war Teil dieser Arbeit.

Es wurde der Einfluss von lokaler Elektron Zyklotron Resonanzheizung (ECRH) und Elektron Zyklotron Stromtrieb (ECCD) auf die Sägezahnperiode an ASDEX Upgrade untersucht. Das Plasma in diesem Experimenten wurde hauptsächlich durch Neutral Teilchen Injektion (NBI) geheizt. Die Gesamtheizleistung wurde zunächst so gewählt, dass keine NTMs auftreten. Es wurde gezeigt, dass durch ECCD in Richtung des Hauptplasmastroms mit Deposition ausserhalb des Plasmazentrums die Sägezahnperiode vergrössert werden kann. Sägezähne konnten sogar für die maximale Dauer eines ECCD Pulses komplett stabilisiert werden. Sie verschwinden mit Einsetzen des Pulses und kehren wieder zurück nach dessen Ende. Dasselbe konnte erreicht werden durch zentrale Deposition von ECCD mit Stromtrieb entgegen des Hauptplasmastroms. Allerdings sind die physikalischen Prozess die zu der jeweiligen Stabilisierung führen unterschiedlich. Mit zentraler ECCD Deposition in Richtung des Hauptplasmastroms kann die Sägezahnperiode verkleinert werden. Mit steigender ECR Leistung wird die Sägezahnperiode geringer. Damit ist ECCD ein geeignetes Instrument zur Kontrolle von Sägezähnen.

Die Erkenntnis, wie man Sägezähne kontrollieren kann, wurde auf Plasmen mit höherer Gesamtheizung angewandt. In einer Entladung wurde während eines gesamten ECCD Pulses das Auftreten einer NTM verhindert. Die Verhinderung von NTMs durch lokale ECCD in Richtung des Hauptplasmastroms, deponiert ausserhalb des Plasmazentrums, wurde somit gezeigt. Durch die weit geringere ECR Leistung verglichen mit der Gesamtheizleistung hat diese Methode grosses Potential im Hinblick auf ITER.



# Contents

<b>1</b>	<b>Introduction</b>	<b>1</b>
<b>2</b>	<b>Theory</b>	<b>9</b>
2.1	Magnetohydrodynamics . . . . .	9
2.1.1	The MHD Equilibrium for Toroidal Geometry . . . . .	10
2.1.2	Ideal MHD Instabilities . . . . .	12
2.1.3	Adiabatic Invariants and Banana Orbits . . . . .	14
2.1.4	Resistive MHD Instabilities . . . . .	16
2.1.5	The Fishbone Instability . . . . .	17
2.2	Theory of the Sawtooth Instability . . . . .	18
2.2.1	Theory by Kadomtsev . . . . .	18
2.2.2	Theory by Porcelli . . . . .	21
2.2.3	Theory by Zakharov . . . . .	26
2.3	Neoclassical Tearing Mode Instability . . . . .	28
2.4	Plasma Heating . . . . .	31
2.4.1	Electron Cyclotron Resonance Heating and Current Drive . . . . .	31
2.4.2	TORBEAM Code . . . . .	33
2.4.3	Neutral Beam Heating . . . . .	34
<b>3</b>	<b>Soft X-Ray Diagnostic</b>	<b>37</b>
3.1	Theory of the Soft X-Ray Diagnostic . . . . .	37
3.2	Soft X-Ray Diagnostic in ASDEX Upgrade . . . . .	39
3.3	Development of a New SXR System . . . . .	40
3.3.1	Calculation of Camera Geometry . . . . .	41
<b>4</b>	<b>Sawtooth Stabilization Experiments</b>	<b>47</b>
4.1	Influence of Sawteeth with NBI . . . . .	48
4.2	Influence of Co-ECCD on Sawteeth . . . . .	50
4.3	Influence of Counter-ECCD on Sawteeth . . . . .	55

4.4	Influence of ECRH on Sawteeth . . . . .	59
<b>5</b>	<b>NTM Control by sawtooth stabilization</b>	<b>61</b>
5.1	Central ECR deposition . . . . .	61
5.2	Off-axis ECR deposition . . . . .	64
5.3	Beta feedback control . . . . .	66
<b>6</b>	<b>Interpretation with ASTRA</b>	<b>71</b>
6.1	ASTRA Transport Code . . . . .	71
6.1.1	Definition of Variables . . . . .	71
6.2	Modelling of Sawtooth Stabilization with the Porcelli Model . . . . .	74
6.3	Modelling of Central Counter-ECCD Deposition . . . . .	82
<b>7</b>	<b>Conclusions and Outlook</b>	<b>85</b>
<b>A</b>	<b>The Tokamak ASDEX Upgrade</b>	<b>89</b>
<b>B</b>	<b>Dispersion Relation</b>	<b>93</b>
<b>C</b>	<b>Kadomtsev Model</b>	<b>97</b>
<b>D</b>	<b>Sawtooth Period Scans without Normalization</b>	<b>99</b>
<b>E</b>	<b>Mode Amplitude Analysis</b>	<b>101</b>
<b>F</b>	<b>Acknowledgement</b>	<b>109</b>

# Chapter 1

## Introduction

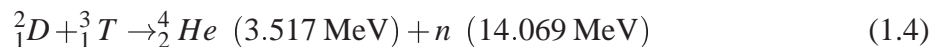
During the last century, industrialization has continued throughout the world and linked with this enormous development has come an increasing demand for energy. Energy sources like wind or water power are not sufficient and raw materials like coal, natural gas or crude oil are exhaustible. Burning these materials leads to high pollution of the atmosphere by releasing impurities and gases like carbon dioxide. A different approach is using nuclear power like fission. In Germany today, fission is no longer supported by the public and government. New ways of producing a long lasting energy source have to be found, for example fusion.

Fusion is possible due to the energy, released by fusing light nuclei. The maximum in the bonding energy for iron enables energy production by splitting atomic nuclei with an atomic mass number higher than iron and by fusing lighter nuclei. The biggest fusion energy sources known are stars, like the sun. The sun produces its energy by fusing four hydrogen atoms to helium in three steps [1]:



Reaction 1.3 is the most likely reaction. Less likely reactions using beryllium, lithium and boron become more important the higher the plasma temperatures ( $T_e > 1$  keV with  $1 \text{ keV} \approx 11600 \text{ K}$ ) [1], [3]. The fusion processes in the stars are very slow due to the weak interaction reaction ( $\beta$ -decay in equation 1.1). They have a very small reaction probability. However, the confinement of a star due to gravity is excellent. On earth, research has to find ways to control fusion processes with high reaction rates and good confinement.

The reaction with the highest cross section for fusion processes at lowest temperatures is the deuterium-tritium reaction:



The amount of fusion processes per volume and time is defined by the reaction rate [2]

$$R_{ab} = n_a n_b \langle \sigma_{\text{fusion}}(u) u \rangle \quad (1.5)$$

with the densities  $n_a$  and  $n_b$  of the different species like deuterium and tritium.  $\langle\sigma u\rangle$  is the reaction parameter with  $u$  the relative velocity defined by  $\mathbf{u} = \mathbf{v}_a - \mathbf{v}_b$ . The cross section  $\sigma$  for fusion processes for some fusion reactions can be seen in figure 1.1.

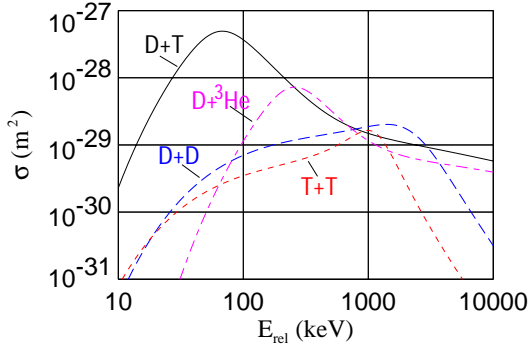


Figure 1.1: Cross section of different fusion processes

energy released by a fusion process. The power of the  $\alpha$ -particle heating  $P_\alpha$  is given by

$$P_\alpha = R_{ab}E_\alpha = \frac{n_e^2}{4}\langle\sigma u\rangle E_\alpha \quad (1.6)$$

The transfer of that energy back to the plasma has to be high enough to sustain the plasma discharge. The following inequality of the power balance has to be fulfilled:

$$P_\alpha > P_{loss} + P_{radiation} \quad (1.7)$$

The parameter  $P_{loss}$  covers the energy loss by convection and heat conductivity,  $P_{radiation}$  for the radiation loss. The radiation energy is mainly lost by Bremsstrahlung with the Bremsstrahlungs constant  $c_{Br} = 5.25 \cdot 10^{-37} \frac{Wm^2}{\sqrt{keV}}$

$$P_{radiation} \approx P_{Bremsstrahlung} = c_{Br}n_e^2Z_{eff}\sqrt{k_B T} \quad (1.8)$$

$n_e$  is the electron density,  $Z_{eff}$  the effective atomic number,  $k_B$  the Boltzmann constant and  $T$  the temperature.

The energy loss due to conduction and convection can be expressed in a simplified form by an empirical time constant. In a pure hydrogen plasma with  $n_e = n_i = n$ ,  $T_e = T_i = T$  and  $\tau_E^e = \tau_E^i = \tau_E$ , the so-called energy confinement time  $\tau_E$  is given by

$$\tau_E = \frac{W}{P_{loss}} = \frac{3nk_B T}{P_{loss}} \quad (1.9)$$

The ignition criterion of equation 1.7 can be rewritten as a function of the temperature  $T$

$$n_e\tau_E > \frac{3k_B T}{\langle\sigma u\rangle E_\alpha/4 - c_{Br}Z_{eff}\sqrt{k_B T}} \quad (1.10)$$

The total energy gained per fusion process can be summarized in  $E = 17.613$  MeV. The neutrons carrying the largest part of the energy, leave the vessel and will be used in a future reactor to extract the gained energy. The goal is to reach a plasma that is maintained without feeding further energy from the outside. In this state, the plasma is ignited. The lost energy will be replaced by  $\alpha$ -particle heating. The efficiency of the  $\alpha$ -particle heating will be proven in the next generation of experiments, in ITER (International Thermonuclear Experimental Reactor). The helium ion carries 20% of the

A parameter, the so-called triple product  $nT\tau_E$  can be defined by measuring the status of a fusion experiment with the density  $n$ , the temperature  $T$  and the energy confinement time  $\tau_E$ . With plasma pressure  $p$  defined as  $p = 2nk_B T$ , the triple product becomes  $p\tau_E$ . For constant temperatures, the ignition criterion can be seen in figure 1.2 together with experimental values for several international fusion devices. The next generation device ITER is designed to significantly exceed the breakeven point. Breakeven means that the energy used to heat the plasma equals the energy gained by fusion processes.

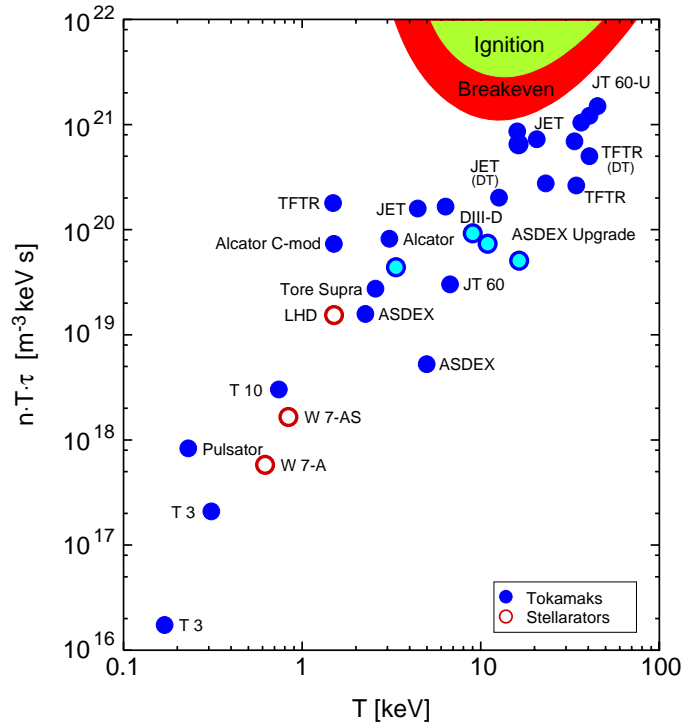


Figure 1.2: Ignition criterion including experimental values

In the first toroidal experiments with magnetic confinement, particle losses by drifts were strongly limiting the confinement. In the presence of a magnetic and an electric field, a drift of the guiding centre is overlaid on to the gyration of electrons and ions. Due to  $B \times \nabla B$  force, the charged particles separate by the so-called grad  $B$  drift. This gives rise to an electric field  $\mathbf{E}$  which leads to an  $\mathbf{E} \times \mathbf{B}$  drift. Both drifts together lead to a net drift of the particles out of the torus. However, by giving a helicity to the magnetic field lines, the drifts can be compensated. The particles drift back into the torus. Today, there are two main branches realizing these twisted field lines: the tokamak and the stellarator.

In today's stellarators, the twisted field is created by complex three dimensional shaped coils. The advantage of this configuration is that no strong main plasma current is needed to maintain the poloidal field. However, due to the complicated geometry, the toroidal symmetry is no longer valid. The toroidal magnetic field in a tokamak is achieved with main field coils. The overlaid poloidal field, necessary to twist the field lines, is created via a transformer. The plasma is used as the secondary winding of the transformer core. Due to the transformer,

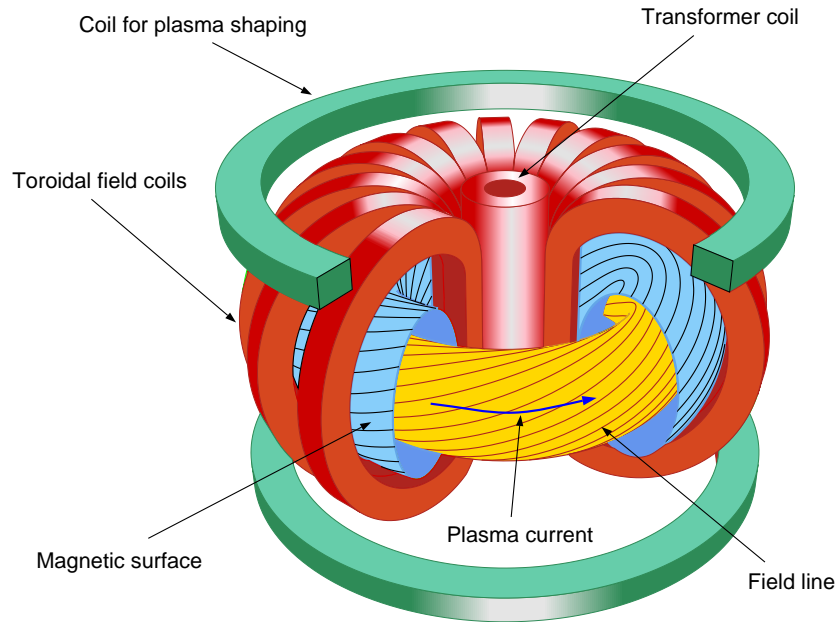


Figure 1.3: The tokamak

current is induced in the plasma that leads to the poloidal field. The advantage of the tokamak geometry is its simplicity due to toroidal symmetry, seen in figure 1.3.

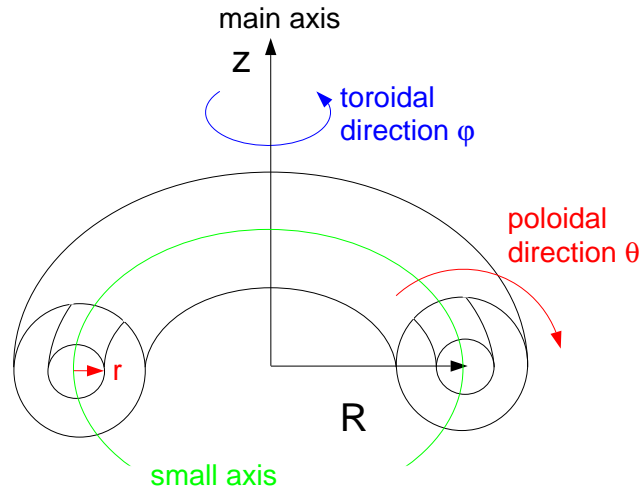


Figure 1.4: Toroidal geometry

Additional shaping coils to elongate the plasma or give it a more triangular shape are added. On the other hand, the strong current needed to maintain the poloidal field, leads to plasma instability. The basic torus geometry is illustrated in figure 1.4.

In figure 1.3 it can be seen, that the magnetic field lines with the same helicity form magnetic surfaces. These magnetic surfaces are at the same time constant pressure and poloidal current

surfaces. They have the shape of tori, nested one into another. The geometry of the field line can be described with the safety factor  $q$

$$q = \frac{m}{n} = \frac{\text{number of toroidal circulations}}{\text{number of poloidal circulations}} \quad (1.11)$$

of the field lines. A  $q = 2/1$  surface for example has closed field lines after two toroidal and one poloidal windings. Plasma instabilities, as will be introduced in chapter 2, usually coincide with these magnetic surfaces of low order of rational  $q$  values. The safety factor is used to label the instability.

The efficiency of the plasma confinement is represented by a factor called  $\beta$ .  $\beta$  is defined as the ratio of plasma pressure over the magnetic field pressure:

$$\beta = \frac{P}{B^2/2\mu_0} \quad (1.12)$$

with the main toroidal field  $B$ . While fusion power increases with the kinetic pressure ( $P_{fus} \approx p^2$ ), the magnetic pressure is mainly limited due to the high costs for the production of high magnetic fields. In today's tokamaks, the efficiency of the plasma confinement is limited by plasma instabilities which are oscillations in the plasma on the magnetic surfaces. To be able to compare the  $\beta$  value with the theoretically predicted limit [4], a normalized  $\beta_N$  is defined:

$$\beta_N = \frac{\beta[\%]}{I[MA]/(a[m] \cdot B[T])} \quad (1.13)$$

In  $\beta_N$ , the parameters like the magnetic field, the current and the small radius are eliminated.

In the tokamak ASDEX Upgrade, operated at MPI Garching, typical temperatures reach  $T = 1 \dots 20$  keV (temperatures of more than 10...200 million degrees). To achieve these high temperatures, it is necessary to heat the plasma. For low temperatures, a very effective heating mechanism is Ohmic heating. Due to the plasma resistance and the high current, the temperature rises. With increasing temperature, the plasma resistance decreases and the Ohmic heating becomes less efficient and so other heating mechanisms, like high frequency waves, or neutral particle injection are needed.

For magnetic fields of several Tesla, the electron gyration frequency lies in the microwave range. In the case of the so-called electron cyclotron resonance heating (ECRH), the electrons are accelerated if the microwave is in resonance with the gyration frequency or its harmonics. Depending on the magnetic field and the density, the ordinary (O-mode) or extraordinary mode (X-mode) is absorbed or reflected. In ASDEX Upgrade, second harmonic X-mode heating is used. The maximum heating power with the ASDEX Upgrade system is currently  $P_{ECRH} = 2$  MW. For more details, see section 2.4.1.

With electron cyclotron radiation (ECR), not only are the electrons heated but very localized electron cyclotron current drive (ECCD) is also possible. As outlined in figure 1.5, if the injection angle of the microwave beam is not perpendicular to the plasma current, depending on the angle, electron cyclotron current drive (ECCD) in co or counter direction to the plasma current becomes possible. The wave energy is transferred to electrons with a resonant parallel

velocity component that leads to a shift in the distribution function to higher parallel electron velocities, resulting in a driven current in either co or counter direction to the plasma current. The injection angle can be varied via movable mirrors inside the torus. The deposition location is usually labelled by a normalized flux co-ordinate  $\rho$ . As seen in figure 1.5,  $\rho$  is defined as one at the last closed flux surface. In the plasma centre  $\rho$  becomes zero.

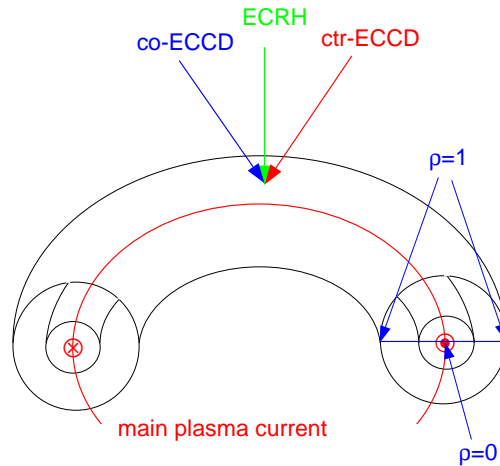


Figure 1.5: Toroidal geometry with sketch of ECRH/ECCD

A different method is the heating of the plasma via injection of neutral particles, the neutral beam injection (NBI). Only neutral particles can penetrate the magnetic field until they get ionized and deflected by the magnetic field. The neutral particle beam is injected into the plasma and results in a very broad deposition profile. The energy is transferred via collisions. The NBI is the main heating source in ASDEX Upgrade with  $P_{NBI} = 20$  MW. By injecting a beam in co or counter direction to the main plasma current, it is also possible to achieve current drive (NBCD).

With increasing plasma pressure, the plasma can become unstable. Instabilities appear on the magnetic surfaces, limiting the confinement. A pressure dependent confinement reduction in  $\beta_N$  is seen clearly in the time trace of figure 1.6 while the total heating power is kept constant. The Mirnov diagnostic, measuring plasma oscillations with a set of coils inside the vessel, shows the  $n=2$  mode amplitude clearly. In the parameter  $\beta$  or the normalized  $\beta_N$ , as defined in equation 1.13, this confinement reduction can be seen. Figure 1.6 shows an  $m=3$ ,  $n=2$  neoclassical tearing mode (NTM), seen in the poloidal cross section in figure 1.7. The mode is called neoclassical because classical transport theory alone is not able to explain this mode behaviour. In the neoclassical transport theory, due to toroidicity, pressure gradients lead to a toroidal current. This current is called bootstrap current and has to be taken into account. An NTM is generated by a flux perturbation due to a perturbation of this bootstrap current. The flux perturbation leads to breaking and reconnection of field lines, forming so-called magnetic islands as seen in figure 1.7. Inside the magnetic islands, the pressure is constant, leading to a reduction of the maximum pressure in the plasma centre. The con-

Control of NTMs is very desirable as it enables  $\beta_N$  to be increased and with it the confinement. NTMs are usually triggered by other instabilities, providing seed islands like the so-called sawtooth instability. One method to control the NTMs is to control the triggering process.

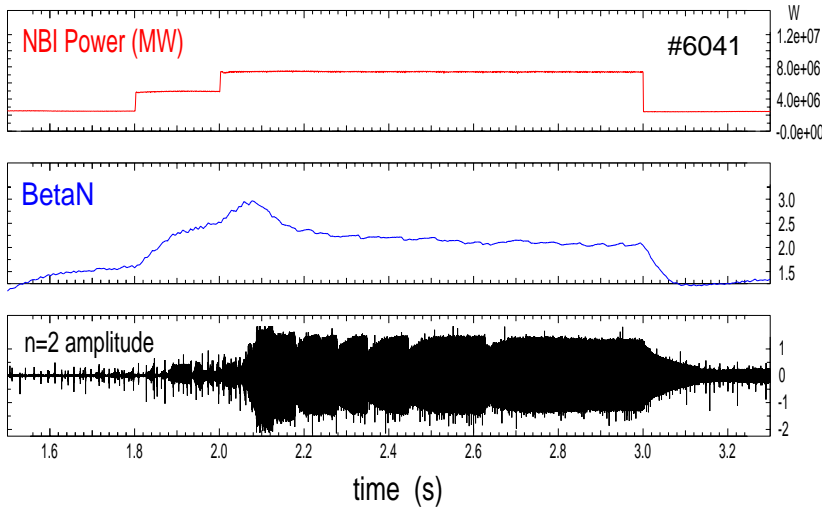


Figure 1.6: Confinement reduction in  $\beta_N$  with constant heating power due to  $m=3$ ,  $n=2$  mode in ASDEX Upgrade, seen in the Mirnov coil pick up signal

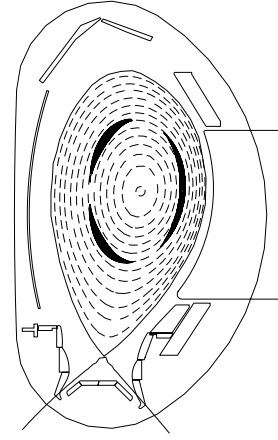


Figure 1.7: Poloidal cross section of  $m=3$ ,  $n=2$  mode

The sawtooth instability is located on the  $q=1/1=1$  surface. This magnetic surface has a special topology. The field lines on this surface wind once in the toroidal and once in the poloidal direction before they close. Due to this fact, the surface can be displaced against the plasma. This displacement is called Kink mode. The sawtooth instability is observed as a slow rise in the central electron temperature, followed by a rapid crash. The temperature in the outer plasma regions slowly decreases until it suddenly increases. The hot plasma core is ejected from the centre. In a simple model, the central current grows due to current diffusion. The safety factor  $q \sim 1/I(r)$  drops below unity, the plasma becomes kink unstable and the hot core is ejected.

The plasma background radiation of today's tokamaks is in the soft x-ray spectrum and can be measured via pinhole cameras equipped with semiconductor diodes, see chapter 3. Because of the temperature dependence of the soft x-ray radiation, it makes it an important tool in observing sawteeth and other instabilities. In figure 1.8, a major result of this thesis, measured with a central chord of the Soft X-Ray (SXR) diagnostic is shown. The sawtooth behaviour can be clearly influenced by ECCD, as shown in figure 1.8. The ECR power was ramped up until the sawteeth vanish, due to driven counter-ECCD. Because the sawtooth instability is located at the  $q = 1$  surface, a local change of the helicity and with it the derivative  $q'$  influences the sawteeth. A change in  $q'$  can be achieved with a localized current like ECCD driven at the  $q = 1$  surface.

In this work the sawtooth tailoring is investigated with application to the delay of the neo-classical tearing mode onset. In the following chapter, the magnetohydrodynamical theory is

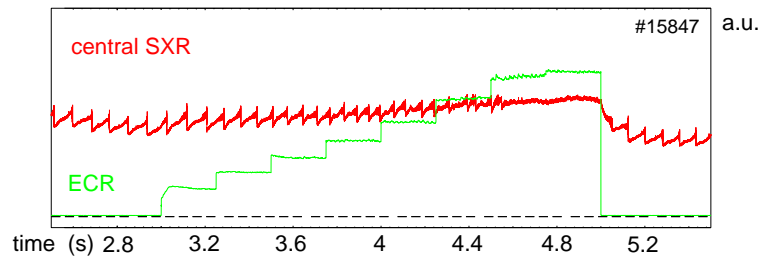


Figure 1.8: Sawtooth stabilization with a central counter-ECCD power ramp up

explained. In the third chapter, a description of the Soft X-Ray diagnostic at ASDEX Upgrade and the development of a new SXR system is given. In chapter 4, experiments showing how to tailor sawteeth are shown. These results are used in chapter 5 to influence the onset of neo-classical tearing modes. In chapter 6, modelling with the ASTRA transport code is presented, applying Porcelli's sawtooth model on ASDEX Upgrade discharges. A summary and outlook are given in the last chapter.

# Chapter 2

## Theory

In this chapter, an introduction to the single fluid treatment of a plasma, the magnetohydrodynamical (MHD) approach, is given. The equations derived in this section are used to calculate the plasma equilibrium. In the case of the ideal MHD limit, infinite conductivity is assumed. A short overview of the basic equations is given. To explain effects like field line reconnection, finite resistivity has to be taken into account. The theory of the sawtooth instability and of neoclassical tearing modes is based on resistive MHD.

Further on, a short explanation of electron cyclotron heating (ECRH) is given. By using the TORBEAM beam tracing code the ECRH deposition location in the plasma is modelled. The principle of ASDEX Upgrade's main heating source, the neutral beam injection (NBI), is described in the last section of this chapter.

### 2.1 Magnetohydrodynamics

A plasma is a multiple particle system, even more complex to describe than classical multiple particle systems. As an additional degree of freedom, the charge of the electrons and ions has to be taken into account. Often, a good approximation is the so-called magnetohydrodynamical (MHD) approach. A hydrogen plasma can be described as a mixture of two fluids, the electrons and ions. The mass density  $\rho$  can be defined as [3]

$$\rho = m_i n_i + m_e n_e \approx m_i n \quad (2.1)$$

with the ion mass and density  $m_i$  and  $n_i$ , the electron mass and density  $m_e$  and  $n_e$  with  $m_e \ll m_i$ . The assumption  $n_i = n_e = n$  is called “quasi neutrality” which is usually well satisfied. The velocity of the centre of mass  $\mathbf{v}$  and the current density  $\mathbf{j}$  are defined as

$$\mathbf{v} = \frac{1}{\rho} (m_i n_i \mathbf{u}_i + m_e n_e \mathbf{u}_e) \approx \mathbf{u}_i \quad (2.2)$$

$$\mathbf{j} = en(\mathbf{u}_i - \mathbf{u}_e) \quad (2.3)$$

with the velocities of the centre of mass of the different species  $\mathbf{u}_i$ ,  $\mathbf{u}_e$ . In this one fluid model, the continuity equation results in

$$\frac{\partial \rho}{\partial t} + \nabla \cdot (\rho \mathbf{v}) = 0 \quad (2.4)$$

By adding up the electron and ion force balance equations

$$m_i n_i \frac{d\mathbf{u}_i}{dt} = en_i (\mathbf{E} + \mathbf{u}_i \times \mathbf{B}) - \nabla \underline{\mathbf{P}}_i + \mathbf{R}_{ie} \quad (2.5)$$

$$m_e n_e \frac{d\mathbf{u}_e}{dt} = en_e (\mathbf{E} + \mathbf{u}_e \times \mathbf{B}) - \nabla \underline{\mathbf{P}}_e + \mathbf{R}_{ei} \quad (2.6)$$

where friction cancels due to  $\mathbf{R}_{ei} = -\mathbf{R}_{ie}$ , the equation of motion for a single fluid is determined to

$$\rho \frac{d\mathbf{v}}{dt} = \rho \left( \frac{\partial \mathbf{v}}{\partial t} + \mathbf{v} \cdot \nabla \mathbf{v} \right) = \mathbf{j} \times \mathbf{B} - \nabla \underline{\mathbf{P}} \quad (2.7)$$

with the pressure tensor  $\underline{\mathbf{P}} = \underline{\mathbf{P}}_e + \underline{\mathbf{P}}_i$  and equation 2.2 in equation 2.3  $\mathbf{u}_e \approx \mathbf{u} - \frac{\mathbf{j}}{ne}$ . The so-called ‘‘generalized Ohm’s law’’ can be used to determine the electric field in the plasma. It is found by writing the electron force balance equation 2.6 in single fluid variables:

$$\mathbf{E} + \mathbf{v} \times \mathbf{B} = \frac{1}{\sigma} \mathbf{j} + \frac{1}{en} (\mathbf{j} \times \mathbf{B} - \nabla p_e) - \frac{m_e}{e} \frac{d\mathbf{v}_e}{dt} \quad (2.8)$$

The momentum transfer of the ions to the electrons can be expressed via the resistance  $\eta = 1/\sigma$  as  $\mathbf{R}_{ei} = \eta ne \mathbf{j}$  [5].

As a consequence of these equations, in the ideal MHD case with infinite conductivity  $\sigma \rightarrow \infty$ , it can be shown that a field line topology moves with the electron velocity  $\mathbf{v}_e$ . The magnetic flux  $\psi$  is ‘‘frozen’’ into the electron gas. As a consequence, field line reconnection, as needed to explain for example the formation of magnetic islands later in this chapter, is not possible using ideal MHD equations. Resistivity has to be taken into account.

### 2.1.1 The MHD Equilibrium for Toroidal Geometry

For equilibrium reconstruction calculations, the force balance equation 2.7 with the additional conditions  $\frac{\partial}{\partial t} \rightarrow 0$  and  $\mathbf{v}=0$  can be used to find the isotropic pressure [3]

$$\nabla p = \mathbf{j} \times \mathbf{B} \quad (2.9)$$

By multiplying equation 2.1.1 with  $\mathbf{B}$  to  $\mathbf{B} \cdot \nabla p = \mathbf{B} \cdot \mathbf{j} \times \mathbf{B} = 0$  it is proven that the vector  $\mathbf{B}$  is situated in a  $p=\text{const.}$  and  $\psi=\text{const.}$  surface where  $\psi$  is the poloidal magnetic flux, as indicated in the introduction chapter. The vectors  $\mathbf{j}$  and  $\mathbf{B}$  are lying in this surface. The constant flux surfaces form tori nested into each other as seen in figure 1.3. Each of these tori is formed by field lines with the same helicity.

Because  $p$  is only dependent on  $\psi$ , equation 2.1.1 can be rewritten as

$$\frac{\partial p}{\partial R} = \frac{dp}{d\psi} \frac{\partial \psi}{\partial R} = j_\Phi B_z - j_z B_\Phi \quad (2.10)$$

With Ampère's Law  $\nabla \times \mathbf{B} = \mu_0 \mathbf{j}$  the variable  $j_\Phi$  and  $j_z$  can be replaced in equation 2.10

$$j_\Phi = \frac{1}{\mu_0} \left( \frac{\partial B_R}{\partial z} - \frac{\partial B_z}{\partial R} \right) \quad (2.11)$$

$$j_z = \frac{1}{\mu_0 R} \frac{\partial}{\partial R} (R B_\Phi) \quad (2.12)$$

The Maxwell equation  $\nabla \cdot \mathbf{B} = 0$  can be transformed to [3]

$$\frac{1}{R} \frac{\partial (R B_R)}{\partial R} + \frac{\partial B_z}{\partial z} = 0 \quad (2.13)$$

introducing the flux dependence of the magnetic field components

$$B_z = \frac{1}{2\pi R} \frac{\partial \psi}{\partial R} \quad (2.14)$$

$$B_R = -\frac{1}{2\pi R} \frac{\partial \psi}{\partial z} \quad (2.15)$$

The magnetic field in the toroidal direction is due to the poloidal current

$$B_\Phi = \frac{\mu_0 I_{pol}}{2\pi R} \quad (2.16)$$

The substitution of equation 2.10 by the equations 2.11, 2.12 and 2.14-2.16 results in a nonlinear partial differential equation for the flux, the Grad-Shafranov-equation:

$$R \frac{\partial}{\partial R} \left( \frac{1}{R} \frac{\partial \psi}{\partial R} \right) + \frac{\partial^2 \psi}{\partial z^2} = \Delta^* \psi = -2\mu_0 \pi R j_\Phi = -\mu_0 (2\pi R)^2 p' - \mu_0^2 I_{pol}^2 / R \quad (2.17)$$

A typical reconstruction using the Grad Shafranov equation can be seen in figure 2.1. The flux surfaces are labelled with the  $q$  values, the last closed flux surface is named separatrix. A similar figure is often drawn showing magnetic surfaces labelled with flux co-ordinates. A poloidal flux co-ordinate can be defined via the poloidal flux  $\psi$

$$\rho_{pol} = \sqrt{\frac{\psi - \psi_a}{\psi_s - \psi_a}} \quad (2.18)$$

with the index  $s$  referring to the separatrix, the last closed flux surface, and the index  $a$  to the magnetic axis.  $\rho_{pol}$  is scaled so that it becomes  $\rho_{pol} = 0$  on the magnetic axis and  $\rho_{pol} = 1$  at the separatrix. Using the toroidal flux  $\Phi$ , a second flux co-ordinate  $\rho_{tor}$  can be introduced:

$$\rho_{tor} = \sqrt{\frac{\Phi - \Phi_a}{\Phi_s - \Phi_a}} \quad (2.19)$$

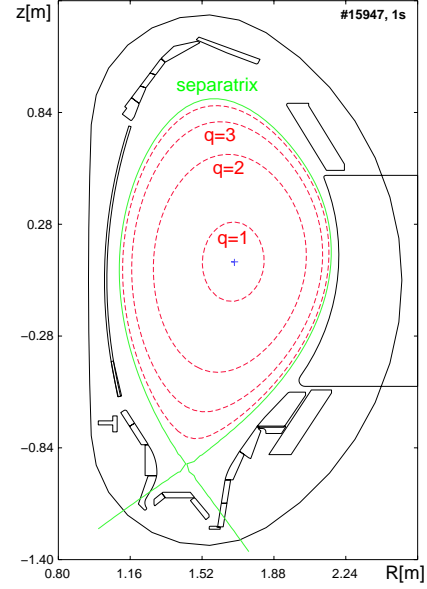


Figure 2.1: Equilibrium reconstruction; the last closed flux surface is named separatrix.

Equivalent to the poloidal flux co-ordinate,  $\rho_{tor}$  becomes zero on the magnetic axis and  $\rho_{tor} = 1$  at the separatrix.

The position of the magnetic axis referring to the last closed magnetic flux surface, seen in figure 2.1, moves with the parameter  $\beta_p$  due to a change in the current and the heating power. The poloidal beta is defined as:

$$\beta_p = \frac{\langle p \rangle}{B_{pol,a}^2/2\mu_0} \quad (2.20)$$

with the cross-sectional average of the pressure  $\langle p \rangle$  and  $B_{pol,a}$  the poloidal magnetic field at the separatrix with the minor radius  $a$ .  $\beta_p$  is a measurement for the fusion power. With increasing heating power,  $\beta_p$  increases.

With increasing heating power, the plasma pressure rises and leads to expansion of the flux surfaces. The expansion force due to the toroidal plasma current adds to this force. To counteract the expansion force, a magnetic vertical stability field is added. The magnetic axis is shifted to the low field side with increasing heating power. In figure 2.2 the so-called Shafranov shift is seen, in which the magnetic axis is shifted to the low field side with increasing heating power. This shift is a result of the balance of the expansion force with the vertical field.

In ASDEX Upgrade,  $\beta_p$  can be controlled via feedback control. Due to variation of the neutral beam heating power,  $\beta_p$  can be adjusted. By lowering the heating power,  $\beta_p$  decreases. Due to its magnetic field dependence, a second possibility is given to vary  $\beta_p$  during a discharge.

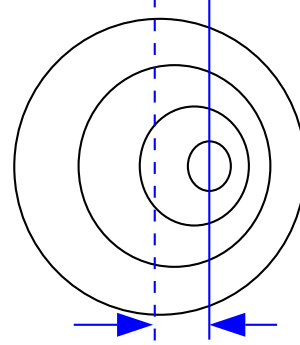


Figure 2.2: The distance between the dashed line, indicating the centre without shift, and the solid line outlines the Shafranov shift of the flux surfaces.

### 2.1.2 Ideal MHD Instabilities

In a plasma, instabilities occur that are limiting the stored energy in the plasma and its confinement. These instabilities can be caused by a current, the current driven instabilities, or by a pressure gradient, the pressure driven instability. To describe these instabilities, the potential energy of the plasma will be discussed.

In the zero resistivity ideal MHD case, an equilibrium is unstable if a perturbation lowers the potential energy of the plasma. To describe a perturbation, the displacement vector  $\xi$  is introduced as the displacement of a fluid element of its equilibrium:

$$\mathbf{v}_1 = \frac{d\xi}{dt} \quad (2.21)$$

By linearization of the MHD equations combined with Faraday's law and Ohm's law

$$\frac{\partial \mathbf{B}_1}{\partial t} = \nabla \times (\mathbf{v}_1 \times \mathbf{B}_0) \rightarrow \mathbf{B}_1 = \nabla \times (\xi \times \mathbf{B}_0) \quad (2.22)$$

the linearized force balance equation can be written as

$$\rho_0 \frac{\partial \mathbf{v}_1}{\partial t} = \mathbf{j}_0 \times \mathbf{B}_1 + \mathbf{j}_1 \times \mathbf{B}_0 - \nabla p_1 \quad (2.23)$$

Using Ampère's law  $\mu_0 \mathbf{j}_1 = \nabla \times \mathbf{B}_1$  the MHD force balance is calculated to

$$\rho_0 \frac{\partial^2 \boldsymbol{\xi}}{\partial t^2} = \frac{1}{\mu_0} (\nabla \times \mathbf{B}_0) \times \mathbf{B}_1 + \frac{1}{\mu_0} (\nabla \times \mathbf{B}_1) \times \mathbf{B}_0 + \nabla (p_0 \gamma \nabla \cdot \boldsymbol{\xi} + \boldsymbol{\xi} \nabla p_0) = \mathbf{F}(\boldsymbol{\xi}) \quad (2.24)$$

with the force  $\mathbf{F}$  created by the displacement and growth rate  $\gamma$ . To solve the differential equation  $\rho_0 \frac{\partial^2 \boldsymbol{\xi}}{\partial t^2} = \mathbf{F}(\boldsymbol{\xi})$ , a Fourier transform in time  $f(\mathbf{x}, t) = f \mathbf{x} e^{-i\omega t}$  can be applied, because all coefficients are time independent. The solution results in an Eigenvalue problem

$$-\omega^2 \rho_0 \boldsymbol{\xi} = \mathbf{F}(\boldsymbol{\xi}) \quad (2.25)$$

It can be proven that  $\mathbf{F}$  is a self-adjoint operator, resulting in real Eigenvalues  $\omega^2$ . For positive values of  $\omega^2$ , the system is stable, while it becomes unstable for negative values of  $\omega^2$ . In reality, to solve the Eigenfunction is a difficult numerical problem. Via variation, an easier solution of the problem can be found by multiplying equation 2.25 with  $\boldsymbol{\xi}$  and by integrating over the volume. The change in energy caused by the displacement can be expressed by this volume integral as

$$\frac{\omega^2}{2} \int \rho_0 \boldsymbol{\xi}^2 dV = -\frac{1}{2} \int \boldsymbol{\xi} \cdot \mathbf{F}(\boldsymbol{\xi}) dV = \delta W \quad (2.26)$$

If the potential energy  $\delta W$  is positive, the system is stable, while the system becomes unstable in the case of a negative  $\delta W$ .

In the case of current driven modes, the pressure gradient can be neglected. In the limit of a big aspect ratio and small mode numbers  $(nr/R_0)^2 \rightarrow 0$ , the potential energy becomes

$$\begin{aligned} \delta W &= \frac{2\pi^2 B_z^2}{\mu_0 R_0} \int_0^a [(r\xi')^2 + (m^2 - 1)\xi^2] \left(\frac{n}{m} - \frac{1}{q}\right)^2 r dr \\ &+ \frac{2\pi^2 B_z^2}{\mu_0 R_0} \left( \frac{2}{q_a} \left(\frac{n}{m} - \frac{1}{q_a}\right) + (1+m) \left(\frac{n}{m} - \frac{1}{q_a}\right)^2 \right) a^2 \xi_a^2 \end{aligned} \quad (2.27)$$

with the safety factor  $q$  and the poloidal and toroidal mode numbers  $m$  and  $n$  (compare with the introduction chapter 1). The index  $a$  marks the value of variables at the minor radius.

If the displacement at the minor radius  $\xi(a) \neq 0$ , the perturbation of the plasma is situated between the plasma and the vacuum. The plasma becomes stable against these so-called external kinks with  $\delta W > 0$  if

$$\frac{n}{m} - \frac{1}{q_a} > 0 \implies \frac{m}{n} < q_a \quad (2.28)$$

The internal kink instability appears for  $\xi(a) = 0$ , which means no displacement at the minor radius. As shown in figure 2.3, the perturbation is only inside the plasma. In equation 2.27,

only the first line, the integration, remains. For  $m = 1$  and no displacement at the  $q = 1$  surface,  $\frac{n}{m} - \frac{1}{q}$  in the remaining part of the integrations becomes zero.

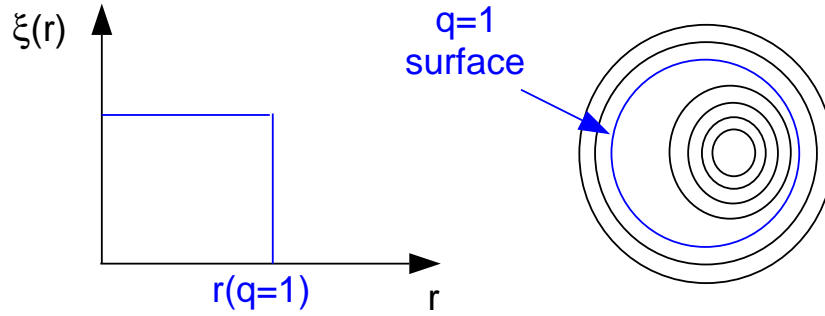


Figure 2.3: In an internal kink instability, the plasma is displaced inside the  $q = 1$  surface. The displacement is shown by its rectangular Eigenfunction.

If the displacement is chosen as a function that is constant inside the  $q = 1$  surface and zero outside, as shown in figure 2.3,  $\delta W$  is zero. This means the system is potentially unstable. However, the experiment shows that usually an internal kink appears if the central  $q$  drops below unity.

With  $m > 1$  and  $\delta W > 0$  the plasma is stable. The stability criterion by minimizing  $\delta W$  becomes  $q(0) > 1$ .

### 2.1.3 Adiabatic Invariants and Banana Orbits

If a system performs periodic oscillations, invariants of motion can be found by applying the following integration:

$$I = \oint p dq \quad (2.29)$$

$q$  is a generalized co-ordinate and  $p$  the generalized momentum [1]. If even by small perturbations of the system, the periodicity remains defined, these invariants are called adiabatic invariants.

The first adiabatic invariant, the magnetic moment  $\mu = mv_{\perp}^2 / (2B)$ , provides the basic principle of the magnetic mirror.  $v_{\perp}$  describes the particle velocity perpendicular to the  $B$  field lines. In a magnetic mirror, particles in a  $B$ -field are reflected by facing a stronger magnetic field. This reflection is explained by the invariance of  $\mu$ . The angular co-ordinate of a gyrating particle in a magnetic field  $\Theta$  is chosen as the generalized co-ordinate and the corresponding momentum is the perpendicular angular momentum.

$$I = \oint p dq = \int_0^{2\pi} \pi m \omega_c r_L^2 d\Theta = 4\pi \frac{m}{q} \mu \quad (2.30)$$

With the Larmor radius  $r_L = v_\perp / \omega_c$  and the cyclotron frequency  $\omega_c = |q|B/m$  and fixed  $m/q$ , the invariance of  $\mu$  is shown.

The second or longitudinal adiabatic invariant  $J$  is defined with the velocity parallel to a magnetic field  $v_\parallel$  and the distance  $s$  as

$$J = \oint v_\parallel ds \quad (2.31)$$

If the distance  $s$  between two magnetic mirrors is reduced, the parallel velocity of the particles has to increase because of the invariance of  $J$ .

The third adiabatic invariant is called flux invariant. Again, if in a magnetic mirror, the particles are reflected between two mirror points, due to the inhomogeneity of the field, the particles drift with the velocity  $v_D$  perpendicular to the field lines. They perform nearly closed circles due to the drift. The invariant is given by

$$\Phi \sim \oint v_D dl \quad (2.32)$$

along the path  $l$  of the drifting particles.

In a tokamak, due to toroidicity, the magnetic field is not homogenous. The high field side (HFS) is situated closer to the transformer core while the low field side (LFS) lays at the outside of the torus. Due to the helicity of the field lines, this change in the  $B$ -field results in a magnetic mirror. The particles, following the magnetic field lines, become reflected, if the ratio  $v_\parallel^2/v_\perp^2$  is sufficiently small (otherwise the particles are passing). The poloidal propagation is reminiscent of a banana; a typical particle path is seen in figure 2.4. Due to the far smaller poloidal field compared with the main field, the banana path is not closed. The particles perform an additional precessional drift in the toroidal direction, seen in figure 2.5. These banana particles are called “trapped particles” because they are lost for the usual transport mechanisms in the plasma.

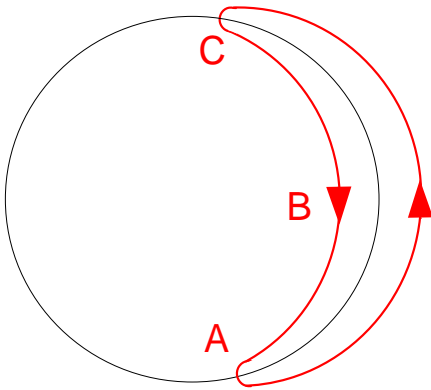


Figure 2.4: Banana orbits due to magnetic mirror

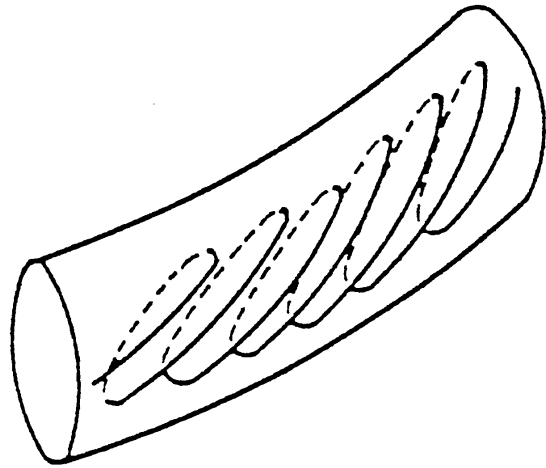


Figure 2.5: Toroidal propagation of the trapped particles. The banana orbits are not closed.

Due to the density gradient in a toroidally confined plasma, more trapped particles exist in the outer banana orbits than in the inner. In a poloidal cross section, this results in a net current in the positive poloidal direction. However, the trapped particles have their main velocity component in the toroidal direction, resulting in a nearly toroidal current. This current is amplified by collisions with passing particles leading to a so-called Bootstrap current. The Bootstrap current is proportional to the pressure gradient  $j_{BS} \sim \frac{\nabla p}{B_0}$ .

### 2.1.4 Resistive MHD Instabilities

In ideal MHD, resistivity is neglected. This approximation leads to flux conservation. However, in a tokamak, resistive instabilities are observed [6]. Allowing a local current perturbation  $\mathbf{j}_1$ , equation 2.22 becomes

$$\frac{\partial \mathbf{B}_1}{\partial t} = \nabla \times (\mathbf{v}_1 \times \mathbf{B}_0) - \frac{1}{\sigma} \mathbf{j}_1 \quad (2.33)$$

This current perturbation  $\mathbf{j}_1$  is not perpendicular to the main magnetic field, in contrast to the ideal equations. By applying the curl to Ampère's law, a diffusion equation  $\Delta \mathbf{B} = D \frac{\partial \mathbf{B}}{\partial t}$  can be derived to

$$\nabla \times (\nabla \times \mathbf{B}) = -\Delta \mathbf{B} = \nabla \times (\mu_0 \mathbf{j}) = \mu_0 \sigma \nabla \times \mathbf{E} = -\mu_0 \sigma \frac{\partial \mathbf{B}}{\partial t} \quad (2.34)$$

with  $\nabla \times \mathbf{B} = \mu_0 \mathbf{j}$  and  $\mathbf{E} = \frac{1}{\sigma} \mathbf{j}$  with the conductivity  $\sigma$ . With the assumption of diffusion over the minor plasma radius  $a$ , the characteristic resistive MHD time scale becomes

$$\tau_{Res} = \mu_0 \sigma a^2 \quad (2.35)$$

Processes dominated by resistivity have long time scales compared to ideal effects with flux conservation. In typical fusion plasmas, the ideal time scale represented by the Alfvén time has values of 1-10  $\mu\text{s}$ . The resistive time scale is far longer than the ideal Alfvén time scale.  $\tau_\eta$  is defined as  $\tau_\eta = \mu_0 \sigma a^2 = a^2 / D_{mag}$  with the conductivity  $\sigma$  and the diffusion coefficient  $D_{mag}$ . In a plasma with the magnetic field  $B = 2$  T, a density of  $n = 10^{20} \text{ m}^{-3}$ , a temperature of  $T = 1$  keV with the Spitzer conductivity  $D_{mag} \approx 0.02 \text{ m}^2/\text{s}$  and the diffusion over a length of  $a = 0.05$  m, the resistive time scale becomes 0.125 s. Taking resistivity into account, field line

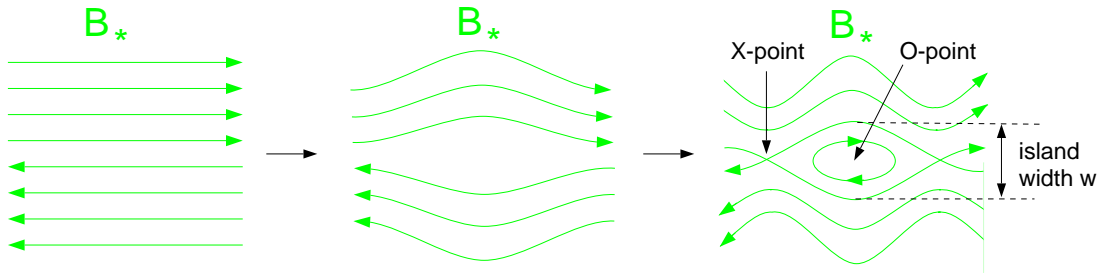


Figure 2.6: Formation of a magnetic island due to field line reconnection of a perturbed magnetic field  $B_*$  with the O-point, the centre of the island, the O-point and the island width  $w$ .

breaking and reconnection becomes possible. Magnetic islands can be formed. The resistive growth rate of instabilities is determined by the time the flux needs to be changed dissipatively, the resistive time  $\tau_{Res}$ . The difference in the time scales enables the separation of ideal and resistive instabilities. A perturbed magnetic field  $B_*$  and how its field lines form new closed flux surfaces is shown in figure 2.6. Due to the breaking or “tearing” of field lines, these resistive modes are called tearing modes. The centre of the island is called the O-point and the point where the field lines “cross” is called the X-point. The island width  $w$  of an island is defined as the maximum distance between the last closed flux surface of the island. The resistive ( $m=1$ ,  $n=1$ ) kink instability causing sawtooth crashes is described in more detail in 2.2. In section 2.3, instabilities with toroidal mode numbers  $m > 1$ , the neoclassical tearing modes (NTMs), are discussed.

### 2.1.5 The Fishbone Instability

The fishbone instability is an ideal instability, situated on the  $q = 1$  surface. It has been recently discovered that it can also have a resistive character [8]. It is characterized by a burst like structure in the Mirnov coil pick up signal and a frequency drop during a burst, seen in figure 2.7 [9], [10].

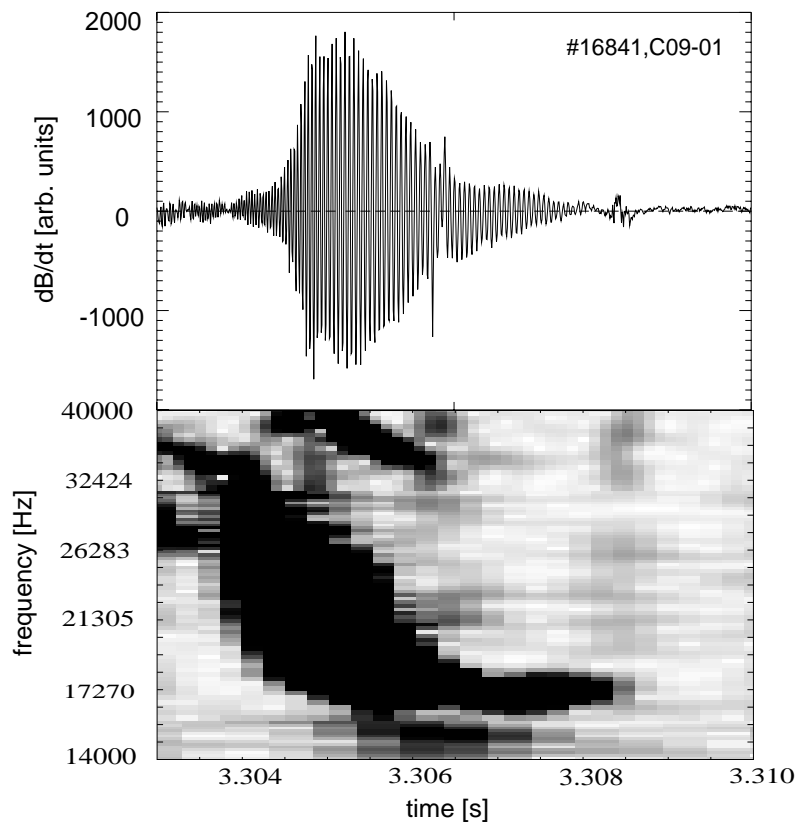


Figure 2.7: Fishbone bursts in the Mirnov signal and the typical frequency drop seen in the wavelet plot below.

In a fishbone burst, the fast trapped particles that are in resonance with the (1,1) fishbone mode, are ejected. At first, the deeply trapped fast particles are in resonance, then the slower, less energetic particles of the fast trapped particle distribution. The energy of the fast trapped particles is proportional to its bounce-averaged toroidal precessional frequency  $\omega_{Dh}$ . The resonance of the mode with less energetic particles results in the frequency drop in the wavelet signal in figure 2.7. This effect is most effective if the mode oscillates with about the thermal ion diamagnetic frequency  $\omega_{di}$  and becomes comparable with the toroidal precessional frequency  $\omega_{Dh}$  (averaged with the bounce time  $\tau_b$  [10]). The fishbone instability appears only in plasmas with a high amount of trapped fast particles like neutral beam heated plasmas. The disturbed distribution function due to the ejection of the highest energetic trapped particles is refilled due to the creation of new fast particles with the NBI.

## 2.2 Theory of the Sawtooth Instability

This internal disruptive instability was discovered by Goeler et al. in 1974 [11]. Kadomtsev [12] gave a first insight into the complete reconnection process as outlined in the previous section. This simple theory depicts the observations. Later on, it became clear that the sawtooth instability could not be fully explained with Kadomtsev's theory. Recently, Porcelli [13] and Zakharov [22] presented a further developed explanation.

### 2.2.1 Theory by Kadomtsev

In sawteeth, often an  $m = 1, n = 1$  instability is observed at the centre of the plasma followed by a rapid internal disruption. The central region cools down rapidly, the outer regions are heated up. This picture is explained by assuming complete reconnection [12]. To give an explanation, the introduction of the helical field  $B_*$  is needed:

$$B_* = B_{pol} - (rB_z/R)e_\theta \quad (2.36)$$

$B_*$  is the poloidal field subtracting the poloidal field at the  $q = 1$  surface, while  $B_{pol}$  is the poloidal component of the magnetic field,  $e_\theta$  is the poloidal unit vector and  $B_z$  the longitudinal field. The evolution of  $B_*$  is shown in figure 2.8. The corresponding time traces of the SXR signal during a sawtooth crash and a wavelet plot, showing the frequency over time dependence, can be seen in the same figure.

The safety factor  $q$  is dependent on the plasma current [3].

$$q = \frac{2\pi r^2 B_\phi}{\mu_0 R} \cdot \frac{1}{I(r)} \quad (2.37)$$

By current diffusion, the central current grows. The central  $q(0)$  drops below unity as in figure 2.8 a). The helical field vanishes at the  $q = 1$  surface. Thus, the direction of the  $B_*$  field lines reverses at the  $q = 1$  surface. If  $q(0)$  drops below unity, the plasma becomes Kink unstable. The internal Kink instability leads to a displacement of the central plasma column inside the

$q = 1$  surface. This leads to the growth of an  $m = 1, n = 1$  island as seen in figure 2.8 b). The first graph in figure 2.9 shows the flux  $\Psi_{*,initial}$  before and  $\Psi_{*,final}$  after the sawtooth crash. Obviously, for every radius  $r_1$  inside  $r_s$  a second radius  $r_2$  with  $r_2 > r_s$  can be found with  $\Psi_{*,initial}(r_1) = \Psi_{*,initial}(r_2)$ . The island grows until the flux surface with  $r = r_1$  touches the surface with  $r = r_2$  which are of equal flux. At this point, the field lines break and reconnect as seen in figure 2.8 b) and form a croissant-shaped surface. At the end, the hot plasma core inside  $q = 1$  is removed from the centre, as seen in figure 2.8. This leads to the quick drop of the red central and the rapid rise of the blue outer SXR signal in figure 2.8.

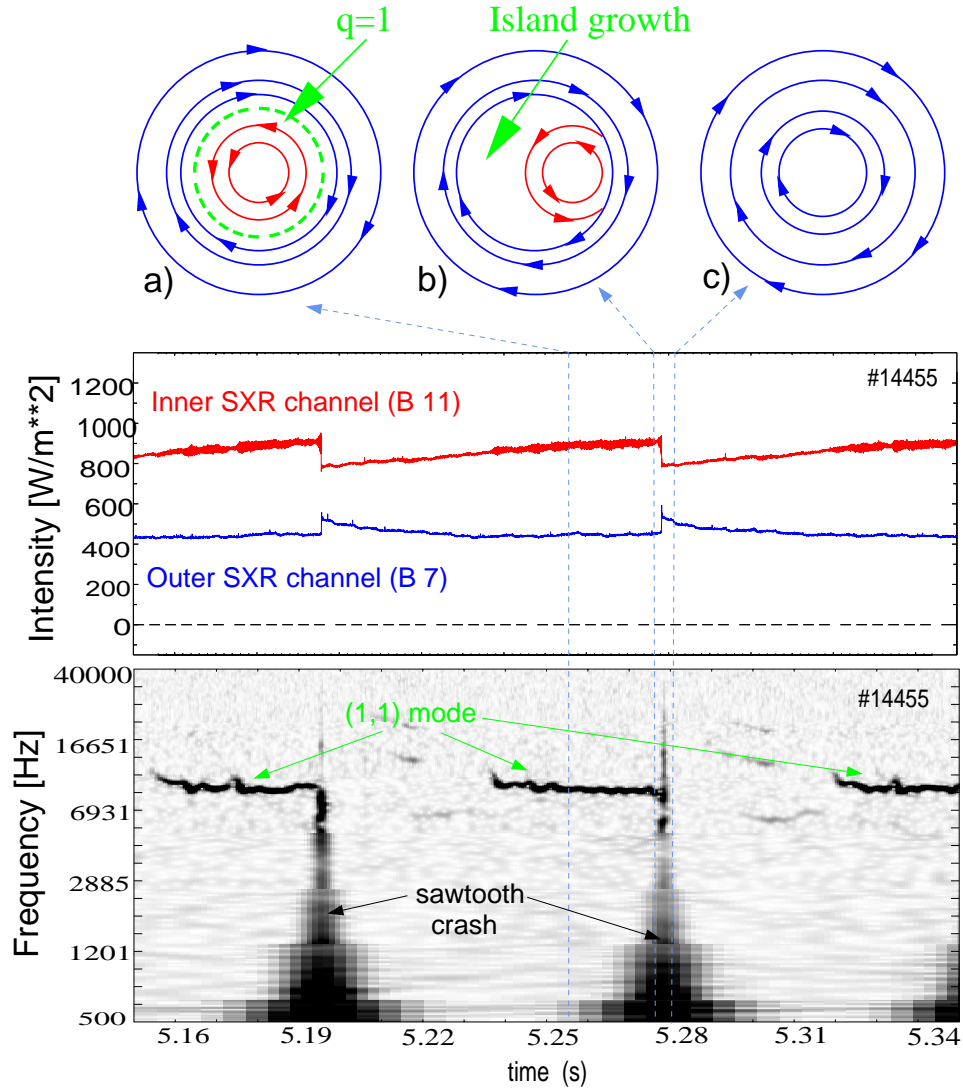


Figure 2.8: Development of  $B_*$ , SXR time trace and wavelet plot during a sawtooth crash

The initial central flux surface  $\Psi_{*,initial}(0)$ , which corresponds to the initial magnetic axis, reconnects with the flux surface at the mixing radius defined in equation 2.38

$$\Psi_{*,initial}(r_{mix}) = \Psi_{*,initial}(0). \quad (2.38)$$

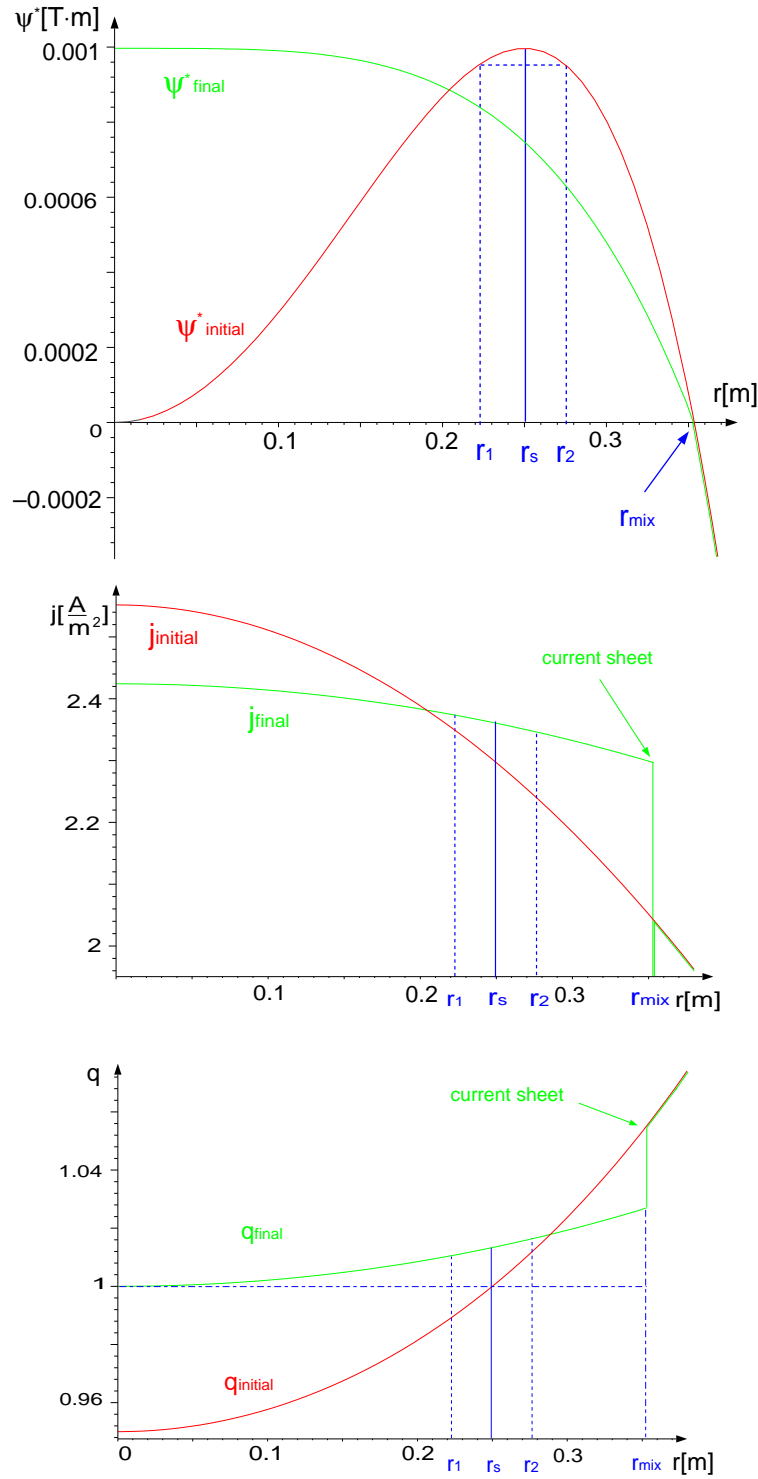


Figure 2.9: Profiles of the central flux  $\psi_*$ , the current density  $j$ , and the safety factor  $q$  before and after a sawtooth crash [7]

Inside the mixing radius the current density is nearly flat which causes the central  $q_{final}(0)$  to rise. In the third graph in figure 2.9, it can be seen that  $q_{final}(0)$  is, as in the beginning, bigger than unity.

At  $r = r_{mix}$  a discontinuity appears because of the jump in  $d\psi_{*,final}(r_{mix})/dr$ . This corresponds to a negative current sheet, a current running in the negative direction with a fast decay as in the second graph of figure 2.9. For a more detailed derivation of figure 2.9, see appendix C.

The Kadomtsev model is an approximation that is quite successful for a not too small resistivity  $\eta$  in a tokamak with an aspect ratio  $a/R \ll 1$  and high  $q_a$  values  $q_a \gg 1$ . The resistive growth rate is much larger than the ideal growth rate [7]. In large-diameter, high-temperature plasmas, the collapse times are more than a magnitude smaller than expected for the calculated  $\eta$  dependence. In addition, direct measurements of the  $q$ -profile indicate that  $q$  might remain below unity throughout the sawtooth period. These findings contradict the simple Kadomtsev model, calling for a further refinement of the sawtooth theory. In the following, the crash phase will not be investigated in more detail, but refined theory for the sawtooth onset will be presented.

### 2.2.2 Theory by Porcelli

This more refined theory of the sawtooth instability takes into account several stabilizing and destabilizing terms. Effects like the growth of an (1,1) mode due to ideal MHD are modified with effects due to resistivity, the rotation of the plasma and the influence of thermal and fast trapped particles. The Porcelli model combines these effects in a model for the sawtooth period which will be presented in this section.

In the ideal MHD theory, the ideal kink mode becomes unstable if its growth rate becomes positive. In section 2.1.2 the potential energy  $\delta W$  was introduced in the limits of ideal MHD. The growth rate  $\gamma$  of an ideal kink can be calculated using a dimensionless normalized energy functional  $\delta\hat{W}$  [13]

$$\delta\hat{W} = -\frac{4\delta W}{s_1 \xi^2 \varepsilon_1^2 R B^2} \quad (2.39)$$

with the radial displacement of the magnetic axis  $\xi$ .  $\varepsilon_1$  is defined as  $\varepsilon_1 = \bar{r}_1/R$ , the ratio of the average  $q = 1$  radius  $\bar{r}_1$  to the major radius  $R$ , and  $s_1$  the shear at the  $q = 1$  surface. The growth rate of the ideal mode can now be written as

$$\gamma = -\frac{\delta\hat{W}}{\tau_A} \quad (2.40)$$

$\tau_A = \sqrt{3}R/c_A$  is the so-called Alfvén time. In the ideal MHD, displacements of the magnetic field lines spread with the Alfvén velocity  $c_A = B/(\mu_0 n_i m_i)^{1/2}$  with the magnetic field  $B$ , the ion density  $n_i$  and the ion mass  $m_i$ .

The effects taken into account in the ideal term are specified in the normalized energy functional. The ideal energy functional will be named  $\delta W_{MHD}$ . A condition for the growth of an

ideal kink instability can now be given by this ideal energy functional as

$$-\delta\hat{W}_{MHD} = \gamma\tau_A > 0 \quad (2.41)$$

which means that a kink mode appears if the ideal growth rate becomes positive.

Effects of toroidicity, using a circular cross section of the plasma, and pressure are included in the ideal term by the so-called Bussac [14] term. The ideal Bussac functional is defined as

$$\delta\hat{W}_{Bussac} = -c_{MHD}\epsilon_1^2(\beta_{p1}^2 - \beta_{pc}^2) \quad (2.42)$$

the total pressure, including the fast particle pressure, is taken into account via the poloidal  $\beta$  at the  $q = 1$  surface, defined over the volume averaged pressure  $\langle p \rangle_1$  at the  $q = 1$  surface:

$$\beta_{p1} = \frac{2\mu_0}{B_{pl}^2}[\langle p \rangle_1 - p(r_1)] \quad (2.43)$$

The parameter  $c_{MHD}$  is defined with the internal inductance  $l_i$  inside the  $q = 1$  surface

$$c_{MHD} = \frac{9\pi}{s_1} \left( l_{i1} - \frac{1}{2} \right) \quad (2.44)$$

With the averaged plasma radius  $\bar{a}$  the parameter  $\beta_{pc}$  becomes

$$\beta_{pc} = 0.3 \left[ 1 - \left( \frac{5\bar{r}_1}{3\bar{a}} \right) \right] \quad (2.45)$$

Even though a circular cross section of the plasma is assumed, the following expressions are still valid for elongated plasmas if the averaged minor radius  $\bar{a}$  is replaced with  $\bar{a} = (ab)^{1/2}$  and the average radius of the  $q = 1$  surface with  $r_1 = \kappa_1^{1/2} r_1$  with the elongation of the  $q = 1$  surface  $\kappa_1$ .

Further corrections due to the plasma shape are necessary. The elongation of the plasma  $\kappa_1$  at the  $q = 1$  surface is taken into account by the so-called elongation term:

$$\delta\hat{W}_{elong} = -c_{el} \left[ \frac{\kappa_1 - 1}{2} \right]^2 \quad (2.46)$$

with the parameter  $c_{el}$  defined as

$$c_{el} = \frac{18\pi}{s_1} \left( l_{i1} - \frac{1}{2} \right) \quad (2.47)$$

The Bussac term and the elongation term can be summarized to the ideal MHD functional  $\delta\hat{W}_{MHD}$ :

$$\delta\hat{W}_{MHD} = \delta\hat{W}_{Bussac} + \delta\hat{W}_{elong} \quad (2.48)$$

By multiplying the sum of the Bussac and the elongation term with a triangularity factor  $C_\delta$ , the corrections due to the triangularity  $\delta$  of the plasma can be taken into account [15] in the

ideal MHD functional. However, the triangularity factor is not part of Porcelli's theory of [13] and is not used in the modelling with the ASTRA transport code in section 6.

A plasma confined in a magnetic field shows diamagnetic behaviour. This means that the magnetic field created due to the gyration of the charged particles reduces the main magnetic field. A pressure gradient is needed to provide a non-zero diamagnetic current resulting in a variation of the diamagnetic magnetic field [2]. Taking the effect of plasma rotation due to these diamagnetic effects into account, a (1,1) mode can be stable as long as the growth rate of the mode is stabilized by the plasma rotation. The ion diamagnetic frequency defined with the necessary pressure gradient can be given as

$$\omega_{*i} = cT / (eB\bar{r}_1 r_p) \quad (2.49)$$

with the temperature  $T$  and the pressure scale length  $r_p = \frac{p}{|dp/d\bar{r}|}$ . The sawtooth triggering criterion in equation 2.41 has to be modified due to the rotation effect and becomes [16]

$$-\delta\hat{W}_{MHD} > 0.5\omega_{*i}\tau_A \quad (2.50)$$

The effects of collisionless thermal trapped ions are taken into account by another stabilizing term. Thermal trapped ions can be calculated via drift kinetic effects or in via the high frequency energy principle [17]. The stabilizing influence on the ideal kink due to the perpendicular compressibility of the thermal trapped particles is derived in [18]. The term used in the Porcelli model, the so-called Kruskal-Oberman term, is derived by the high frequency energy principle. The effect of the thermal trapped ions leads to an increase of  $\beta_{pol}$  at the  $q = 1$  surface far over the MHD value [17]. The Kruskal-Oberman term  $\delta W_{KO}$  is defined as follows, assuming that the thermal trapped particles are collisionless, which means they do not undergo collisions:

$$\delta\hat{W}_{KO} = 0.6c_p\epsilon_1^{1/2}\beta_{i0}/s_1 \quad (2.51)$$

with the peak ion toroidal beta  $\beta_{i0}$  and the parameter  $c_p$ , using again  $x = r/r_1$  and the ion pressure profile  $p_i(x)$  with the maximum value  $p_{i0} = p_i(0)$

$$c_p = \frac{5}{2} \int_0^1 dx x^{3/2} \frac{p_i(x)}{p_{i0}} \quad (2.52)$$

The electrons are collisional and are not included in the Kruskal-Oberman term. In cases of flat pressure profiles, the parameter  $c_p$  becomes one. The mode frequencies have to be higher than the thermal ion diamagnetic frequency that the  $\delta\hat{W}_{KO}$  term is valid.

If the thermal trapped particle effect is taken into account, the energy functional describing the stability of the kink mode has to be modified. The modified energy functional is written as

$$\delta\hat{W}_{core} = \delta\hat{W}_{Bussac} + \delta\hat{W}_{elong} + \delta\hat{W}_{KO} = \delta\hat{W}_{MHD} + \delta\hat{W}_{KO} \quad (2.53)$$

with  $\delta\hat{W}_{core}$  describing the sum of the energy functionals. This leads to a new sawtooth triggering condition:

$$-\delta\hat{W}_{core} > 0.5\omega_{*i}\tau_A \quad (2.54)$$

A well known stabilizing process [19] is the fast particle stabilization. As seen in section 2.1.5, if the frequency of a mode is about the thermal ion diamagnetic frequency  $\omega_{di}$  and if  $\omega_{di}$  is comparable to the precessional drift frequency  $\omega_{Dh}$  of deeply trapped fast particles [10], the fishbone instability is most effective. However, for  $\omega_{Dh} \gg \omega_{di}$  a stabilizing term to the  $m = 1$  dispersion relation is found.

Fast particles with toroidal precessional frequencies far higher than the frequency of a mode conserve the third adiabatic invariant. These fast particles can be seen as current loops around a poloidal helical flux tube. Due to the conservation of the third adiabatic invariant, the flux in these current loops is conserved if they contract or expand. If the fast particle pressure is peaked in the plasma centre and the current loop contracted adiabatically due to a mode, the fast trapped particles in the current loop have to be accelerated due to the flux conservation. The internal energy of the fast particles is increased, which results in a positive work against the centrally peaked fast particle pressure. Thus the fast particles have a stabilizing effect.

The stabilizing effect of the fast particles become relevant compared to the core energy functional in the following limit:

$$-\delta\hat{W}_{core} > c_h \omega_{Dh} \tau_A \quad (2.55)$$

with  $\omega_{Dh} > \omega_{*i}$  a numerical factor  $c_h$  in the order of unity. Equation 2.55 is on criterion for sawtooth triggering and is implemented to the ASTRA code. However, in the triggering condition for the kink, the fast particle energy has to be added to the sum of the energy functionals, covering this additional effect. To the ideal MHD potential energy  $\delta W_{MHD}$ , kinetic effects of the high energy particles, like fusion  $\alpha$  particles or fast particles produced by auxiliary heating, have to be added with the positive fast particle term  $\delta W_{fast}$

$$\delta\hat{W}_{fast} = c_f \epsilon_1^{3/2} \beta_{p\alpha}^* / s_1 \quad (2.56)$$

with a coefficient  $c_f$  in the order of unity for the limit  $\omega \ll \omega_{Dh}$ . The parameter  $\beta_{p\alpha}^*$  is dependent on the fast particle pressure gradient inside the  $q = 1$  surface with  $x = r/r_1$ :

$$\beta_{p\alpha}^* = \frac{2\mu_0}{B_p^2(r_1)} \int_0^1 dx x^{3/2} \frac{dp_\alpha}{dx} \quad (2.57)$$

$B_p$  stands for the poloidal magnetic field. Fast particle stabilization is dependent on the pressure profile and becomes effective for centrally peaked pressure profiles.

With the stabilizing terms  $\delta W_{fast}$  and  $\delta W_{KO}$ , the potential energy becomes

$$\delta W = \delta W_{MHD} + \delta W_{KO} + \delta W_{fast} \quad (2.58)$$

The total normalized energy functional can be summarized by adding these four terms if a monotonically increasing  $q$ -profile is assumed with a central  $q_0$  well below unity.

The additional term in  $\delta W$  leads again to a modification of the criterion 2.54:

$$-\delta\hat{W} > 0.5\omega_{*i}\tau_A \quad (2.59)$$

Equation 2.59 is now in its final form as it is used in the Porcelli model and implemented to the ASTRA code.

Even if both criteria of equation 2.55 and 2.59 are not valid, a destabilization of a kink mode is still possible. In the limit of the potential energy  $\delta W$  being nearly zero, resistivity, finite Larmor radius effects, diamagnetic frequency effects or other microscopic effects might change the mode dynamics, localized close to the  $q=1$  surface. In this region, magnetic reconnection is possible. In the so called ion-kinetic regime, the layer width  $d_e$  close to  $q = 1$  is smaller than the ion Larmor radius  $\rho_i$ .  $d_e$  is the width of the electron current layer, in which reconnection can take place. The width of this layer is limited due to the parallel diffusion of the electrons. There, the collisional resistivity is of more importance than the electron inertia. The ion kinetic regime is valid if the following inequality is fulfilled:

$$\rho_i > \delta_\eta > d_e \quad (2.60)$$

$\delta_\eta$  defines the resistive layer width  $\delta_\eta = s_1^{-1/3} S^{-1/3} \bar{r}_1$ .

In the ion kinetic regime, if diamagnetic effects are neglected, the characteristic growth rate  $\gamma_\rho$  of an internal kink mode can be defined [20] as

$$\gamma_\rho = C_\rho(\tau) \hat{\rho}^{4/7} S^{-1/7} s_1^{6/7} \tau_A^{-1} \quad (2.61)$$

with  $\tau = T_e/T_i$ ,  $C_\rho(\tau) = [2(1 + \tau)/\pi]^{2/7}$  the magnetic Reynold's number  $S = \tau_\eta/\tau_A$  with the local resistive diffusion time over the length  $\bar{r}_1$   $\tau_\eta$  and  $\hat{\rho} = \rho_i/\bar{r}_1$ . The resistive time scale is far longer than the ideal Alfvén time scale mentioned above.

Layer physics becomes important if

$$|\delta \hat{W}| \leq |\delta \hat{W}_{crit}| = |\max\{\rho\}, (\omega_{di} \tau_A/2)| \quad (2.62)$$

is valid. Effects due to the ion diamagnetic frequency  $\omega_{*i}$  as well as the diamagnetic frequency  $\omega_{*e}$  have to be taken into account. However, we assume that  $\omega_{*e} \sim \omega_{*i}$ . In the interval

$$-\hat{\rho} < -\delta W < \hat{W}_{crit} \quad (2.63)$$

the destabilization of a  $m = 1$  mode is possible due to ion diamagnetic frequency effects, taking the effective plasma viscosity into account. This regime is only valid if  $\omega_{*i}$  is a couple of times larger than the growth rate (2-4 times), neglecting diamagnetic frequency effects, calculated with  $\omega_{*i} = 0$ .

By using the growth rate in equation 2.61, a criterion for the sawtooth onset can be given with

$$\omega_{*i} < c_* \gamma_\rho \quad (2.64)$$

with the numerical factor  $c_*$  of the order of unity. The factor  $c_*$  is dependent on plasma parameters like the plasma shape and collisionality. These parameters will vary with the fusion devices and have to be found separately for the different experiments.

The above described regimes can be summarized in three sawtooth triggering conditions:

$$-\delta\hat{W}_{core} > c_h\omega_{Dh}\tau_A \quad (2.65)$$

$$-\delta\hat{W} > 0.5\omega_{*i}\tau_A \quad (2.66)$$

$$-c_p\hat{p} < -\delta\hat{W} < 0.5\omega_{*i}\tau_A \quad \text{and} \quad \omega_{*i} < c_*\gamma\rho \quad (2.67)$$

with  $c_h$ ,  $c_p$  and  $c_*$  of order of unity. The second part of equation 2.67 can be transformed into a critical shear criterion for sawtooth triggering:

$$s_1 > s_{crit} = \alpha(S^{1/3}\hat{\rho})^{1/2}(\beta_{i1}R^2/\bar{r}_1^2)^{7/12}(\bar{r}_1/r_n)(\bar{r}_1/r_p)^{1/6} \quad (2.68)$$

with the ion toroidal beta  $\beta_{i1}$  at the  $q = 1$  surface and  $\alpha = 1.5 \cdot c_*^{-7/6} \left[ \frac{T_e}{T_i} \frac{1}{1+T_e/T_i} \right]^{7/12}$ . The critical shear criterion is directly dependent on the factor  $c_*$  and can be chosen in the order of unity, for example in [13]  $c_* = 3$ . The critical shear is inverse proportional to the density scale length at the  $q = 1$  surface  $r_n = \frac{n}{|dn/dr_1|}$ . A weaker dependence is seen on the pressure scale length  $r_p$ , defined analog to the density scale length.

Driving current close to the  $q = 1$  surface causes the  $q$ -profile to change in this region. This change influences the criteria above with the change in the shear. A reduction of the shear at the  $q = 1$  surface leads to an easier fulfilment of the critical shear criterion.

### 2.2.3 Theory by Zakharov

While Porcelli uses a combination of kinetic treatment of the ions with a fluid model for the electrons, Zakharov models the sawtooth behaviour purely by using a two fluid model [21]. In TFTR supershots with long sawtooth free phases, very peaked pressure profiles were observed. The central  $\beta_{1,pol}$ , defined in equation 2.71, was with  $\beta_{1,pol} \sim 1 \dots 1.5$  far higher than the theoretical onset of the  $m = 1$  mode at  $\beta_{1,pol} \sim 0.3$  [22]. The stabilization of sawtooth oscillations due to  $\omega_*$  effects were investigated, comparable to the derivation of Porcelli's critical shear criterion in equation 2.67.

As in the Porcelli model, Zakharov takes effects of finite drift frequencies  $\omega_*$  into account which lower the mode growth rate  $\gamma$ . For the growth rate of the ideal mode, the variable  $\gamma_I$  is chosen with

$$\gamma_I\tau_A = \frac{q'_1\lambda_H}{\sqrt{3}} \quad (2.69)$$

with the Alfvén time  $\tau_A$  defined in 2.2.2 and  $q'_1 = q'(\bar{r}_1) = dq/dr|_{\bar{r}_1}$  at the  $q = 1$  radius.  $\lambda_H$  describes the inertial singular layer

$$\lambda_H \approx -\frac{3\pi}{q'_1} \frac{\bar{r}_1^2}{R^2} (0.3^2 - \beta_{1,pol}^2) \quad (2.70)$$

with

$$\beta_{1,pol} = \frac{2\mu_0[\langle p \rangle_1 - p(\bar{r}_1)]}{B_\Theta^2(\bar{r}_1)} \quad (2.71)$$

In the evaluated TFTR discharges, the typical value of  $\lambda_H$  was positive and in the range of 1 cm. The stability criterion for the ideal mode

$$\lambda_H \leq 0 \quad (2.72)$$

is violated even in the sawtooth free area. This criterion is identical with the criterion 2.40, but the energy functional  $\delta\hat{W}_{MHD}$  only contains the Bussac term  $\delta\hat{W}_{Bussac}$  of equation 2.42. The parameter  $c_{MHD}$  becomes  $\frac{3\pi}{\sqrt{3}} \approx 5.4$ .

Taking the collisionless reconnection mode with a nonlinear growth rate into account by neglecting the resistive reconnection mode (unimportance shown in [22]), equation 2.69 becomes

$$\gamma_{nonlinear}\tau_A \approx q'_1\rho_s \quad (2.73)$$

with the ion-sound Larmor radius  $\rho_s = \frac{\sqrt{(T_e+T_i)/m_i}}{\omega_{ci}}$  and the ion cyclotron frequency  $\omega_{ci}$ .

The collisionless reconnection mode can be stabilized in the two fluid model (similar to the ideal mode) by  $\omega_*$  effects. If the so-called singular layer equation [21] has a solution with a real Eigenvalue. As in the Porcelli model, the criterion for sawtooth triggering can be written as the critical shear criterion 2.68 in the Porcelli model:

$$s_{crit} < s_1 \quad (2.74)$$

By including kinetic effects of energetic beam particles using fluid theory, a further term, named  $\lambda_K$ , has to be added to  $\lambda_H \rightarrow \lambda_H + \lambda_K$

$$\lambda_K = \frac{\bar{r}_1}{s_1^2} \left(\frac{\bar{r}_1}{R}\right)^{3/2} \frac{2\mu_0}{B_\Theta^2(\bar{r}_1)} \int_0^{\bar{r}_1} \left(\frac{r}{\bar{r}_1}\right)^{3/2} p'_{hot} dr \quad (2.75)$$

Even the modification due to the fast particle term gives a slight improvement, but does not reproduce the experimental observations.  $s_{crit,II}$  is still lower than the shear, observed in the experiment.

With a third assumption that the dominant ideal mode can be neglected,  $\lambda_K$  and  $\lambda_H$  are set to zero. A simplified but analytically close form is given by the following shear criterion for sawtooth triggering:

$$s_{crit,III} \approx 1.4\beta_1^{2/3} \left|\frac{R}{r_n}\right|^{2/3} \left|\frac{R}{r_p}\right|^{1/3} < s_1 \quad (2.76)$$

with the density  $n$ . Compared with equation 2.68, similar dependencies can be found in equation 2.76. The density scale length  $r_n$  scales slightly different due to the power of -2/3 compared with the power of -1 in the Porcelli criterion. The pressure scale length is scaled with the power of -1/3 compared with -1/6 in 2.68. In both criteria,  $\beta$  plays a role with a stronger dependence in Zakharovs criterion, but Porcelli takes the ion toroidal beta into account.

The third criterion 2.76 does successfully reproduce the appearance of sawtooth free phases in TFTR supershots. However, the criterion is inconsistent with the linear theory.

For the modelling that will be presented in the chapter 6, only the Porcelli model will be taken into account.

## 2.3 Neoclassical Tearing Mode Instability

A typical resistive pressure driven instability is the neoclassical tearing mode (NTM). Currently, NTMs are the main limitation in confinement efficiency in conventional H-mode tokamak discharges. These NTMs limit the plasma pressure  $p$ , as outlined in figure 2.10.

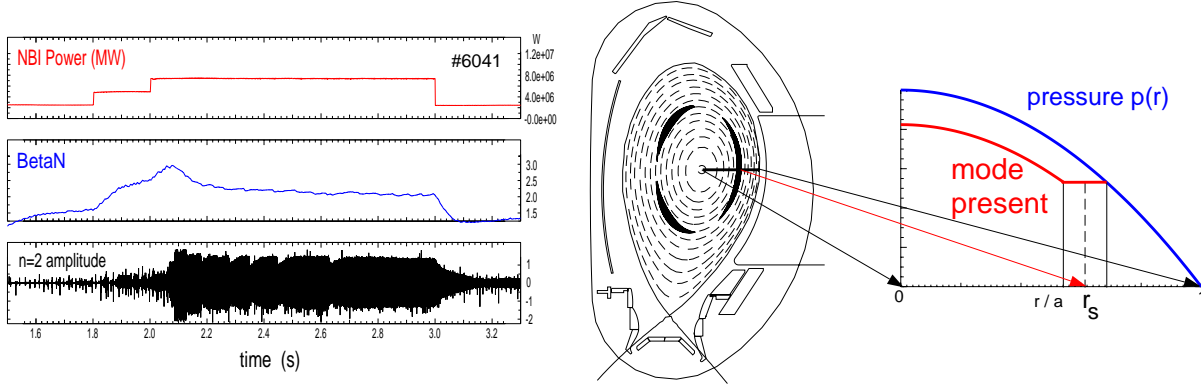


Figure 2.10: Limit in  $\beta$  and pressure degradation due to NTM

Figure 2.10 shows a  $m = 3, n = 2$  mode, forming three islands in the poloidal cross section. If an island is formed at a rational surface with high pressure gradient, the pressure gradient will flatten in the island, as seen in figure 2.10.

Due to the dependence of the bootstrap current on the pressure gradient, the bootstrap current decreases. The missing current in the island is leading to a helical defect current in the O-point of the island (see figure 2.6), increasing its size. The increasing island size leads to a further decrease of the pressure gradient. Obviously, if a small island exists, starting to decrease the pressure gradient, the plasma becomes unstable against the NTM. These so-called seed islands can be created by other instabilities like sawteeth or fishbones. Due to the formation of seed islands, these instabilities can trigger NTMs.

The lowering effect on the pressure leads to a degradation of the confinement efficiency, expressed with the parameter  $\beta$ , introduced in equation 1.12.  $\beta$  is defined as the ratio of plasma pressure over the magnetic field pressure as in equation 1.12.

$\beta$  is a measure how much pressure can be sustained for a given magnetic field. The kinetic pressure is dependent on the fusion power. The fusion power is limited by the kinetic pressure. The main limiting factor of the magnetic field is the high costs for the production of high field copper coils. However, in a future fusion device, the coils have to be superconducting to

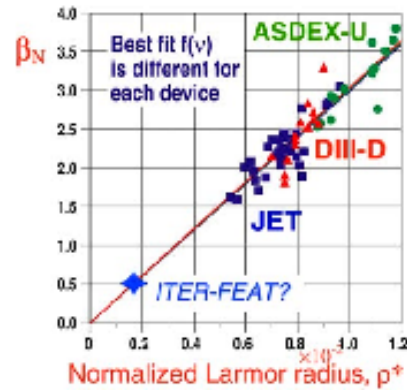


Figure 2.11: NTM onset in  $\beta_N$  over normalized Larmor radius  $\rho_*$

minimize losses and allow long pulse lengths. The maximum field in superconducting coils is limited due to the breakdown of superconductivity with high fields.

A normalized  $\beta_N$  is used to compare fusion devices of different sizes and geometries, defined as in equation 1.13. Factors like the magnetic field, the current and the minor radius are eliminated in  $\beta_N$ . Figure 2.11 shows the dependence of the onset of the (3,2) NTM on  $\beta_N$  for the tokamaks JET, Great Britain, DIII-D, USA, ASDEX Upgrade and an expected value for ITER [23].

The size of these NTMs develops with time. The temporal evolution of the island width can be described by the generalized Rutherford equation [24]:

$$\frac{\tau_{res}}{r_{res}} \dot{w} = \underbrace{r_{res} \Delta'(w)}_{(1)} + r_{res} \beta_p \left( \underbrace{a_2 \sqrt{\epsilon} \frac{r_q}{r_p} \frac{w}{w_0^2 + w^2}}_{(2)} - \underbrace{a_3 \frac{\epsilon}{R_0} \frac{r_q^2}{r_p} \frac{1}{w}}_{(3)} - \underbrace{a_4 g(v) \left( \rho_p \frac{r_q}{r_p} \right)^2 \frac{1}{w^3}}_{(4)} \right) - \underbrace{a_5 \frac{r_q r_{res}}{2\sqrt{\pi}} \frac{I_{ECCD}}{I_p(r_{res})} f(w) \frac{1}{w^2}}_{(5)} \quad (2.77)$$

with  $\tau_{res}$  the resistive time scale,  $r_{res}$  the radius of the resonant surface, the shear and pressure scale lengths  $r_q = q/\nabla q$  and  $r_p = -p/\nabla p$ , the function  $g(v)$ , that changes from a small to a large value if the collisionality  $v$  is above a certain value, and the critical island width  $w_0$  below which  $p$  no longer flattens across the island due to finite parallel heat conduction.

The term with the subscript (1) takes the equilibrium current profile characterized by the stability parameter  $\Delta'$ , into account. The bootstrap current drive, introduced in section 2.1.3, is included in term (2). The stabilizing effect of toroidicity is shown in term (3), while term (4) describes a stabilizing polarization current. In ASDEX Upgrade, complete stabilization of neoclassical tearing modes was achieved by localized electron cyclotron current drive (ECCD), described in term (5). The deposition width of the ECCD is taken into account by the function  $f(w)$ . Figure 2.12 shows the island growth  $dw/dt$  over the island size  $w$  for different  $\beta_p$  values.

The mode appears with a  $\beta_{p,onset}$ . The growth of the mode follows the red arrow in figure 2.12 up to its saturated size. If the mode has reached its maximum size,  $dw/dt$  becomes zero. If  $\beta_p$  decays, the island width shrinks, shown by the blue arrow. For a  $\beta_p < \beta_{p,crit}$ , shown in green, the mode decays further and disappears.

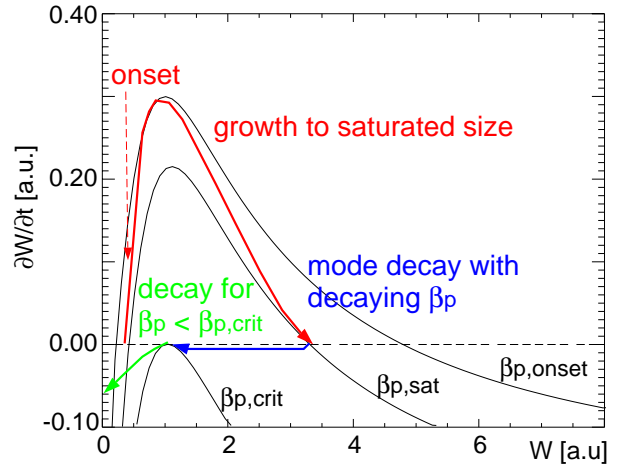


Figure 2.12: NTM trigger condition

To trigger an NTM, usually another MHD event like a sawtooth crash or a fishbone instability is present. These instabilities give rise to a seed island. In ASDEX Upgrade, seed island sizes are usually 1...1.5 cm. In figure 2.13, several fishbones are shown until an NTM is triggered by a sawtooth. The first time trace shows the SXR signal, the second and the third one indicate mode activity. If a mode with even toroidal mode number like the (3,2) mode appears, a signal is seen in the Even N time trace of the Mirnov coil diagnostic. With an odd mode number

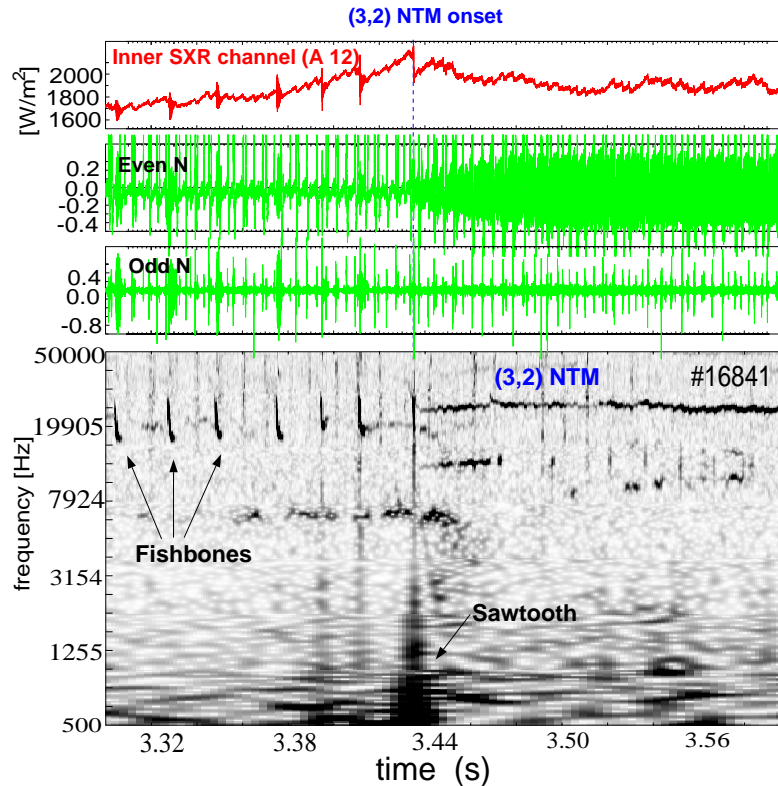


Figure 2.13: Sawtooth triggered NTM. The mode can be seen in the Mirnov coil pick up signals for even and odd  $n$  mode numbers and in the wavelet plot.

as the (1,1) mode of the fishbone activity, a signal is seen in the Odd N time trace. The last diagramme shows a wavelet plot with the frequency over time. Fishbones, sawteeth and the NTM are marked.

The suppression of the sawteeth is equivalent with the suppression of a seed island for the NTM. If no seed island is given by a sawtooth, it was shown at ASDEX Upgrade [25] and later at JET [26] that the  $\beta$  value can be increased until another instability like the fishbone instability triggers the mode. In the discharge in figure 2.13, an NTM was triggered by a fishbone. The fishbone is clearly seen in the SXR and Odd N time traces. If additional to sawteeth as well the fishbone instability can be suppressed, the  $\beta$  value at the NTM onset can be even further increased [25]. At very high  $\beta$  even the spontaneous appearance of an NTM is possible without a seed island due to a previous instability.

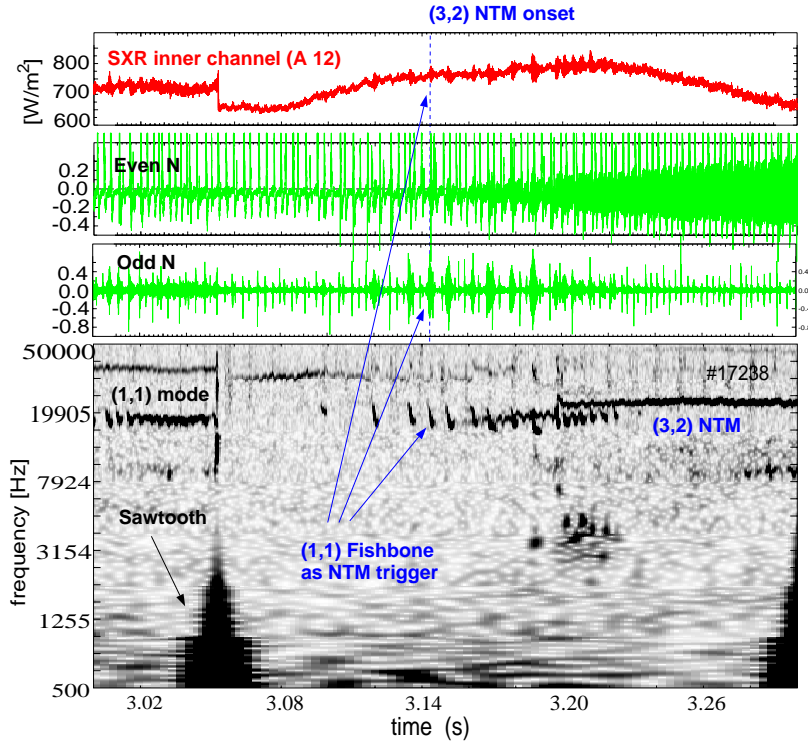


Figure 2.14: Fishbone triggered NTM. The mode can be seen in the Mirnov coil pick up signals for even and odd  $n$  mode numbers and in the wavelet plot.

## 2.4 Plasma Heating

The main toroidal plasma current that creates the poloidal field is not only necessary for the equilibrium. At low temperatures, very strong Ohmic heating is achieved dependent on the plasma resistance. The resistance  $\eta$  varies with temperature  $\eta \sim T_e^{-\frac{3}{2}}$  [2]. However, the higher the plasma temperature the less effective the Ohmic heating becomes. Further heating mechanisms have to be considered. The electron cyclotron resonance heating and current drive method will be explained as well as the injection of neutral particles, the neutral beam heating. ASDEX Upgrade also is equipped with ion cyclotron resonance heating, which will not be explained in detail.

### 2.4.1 Electron Cyclotron Resonance Heating and Current Drive

By using microwaves with frequencies of the electron or ion gyration frequency the plasma can be heated. The accessibility of the plasma is limited due to cut-offs and resonances, see appendix B. By perpendicular injection, the heating of the electrons is independent of their parallel velocity, seen by the symmetric circles in the  $v_{\perp} - v_{\parallel}$  diagramme in figure 2.15. The resonance condition can be expressed as

$$\omega - \omega_{ce} = k_{\parallel} v_p \quad (2.78)$$

with the cyclotron frequency  $\omega_{ce}$ ,  $k_{\parallel}$  the component of the wavenumber parallel to the magnetic field and  $v_p$  the phase velocity. Only electrons are heated that are circulating in toroidal direction with certain parallel velocities  $v_{\parallel}$ . The electrons fulfilling the resonance condition are heated preferentially. These collide less often with the ions than the electrons with circulation in the opposite direction than the heated electrons. A current is generated due to this difference in momentum transfer to the ions [27], [2].

The evolution of the electron distribution function  $f$  in the presence of additional effects like current drive is described by the Fokker-Planck equation [27]

$$\frac{df}{dt} = C(f, f) + C(f, f_i) - \frac{\partial}{\partial \mathbf{v}} \cdot \mathbf{S}_{\omega} \quad (2.79)$$

with  $C(f, f)$  the self-collisions of electrons,  $C(f, f_i)$  the scattering of electrons off-ion distribution  $f_i$  and the wave induced flux  $\mathbf{S}_{\omega}$ . Due to a preference of electrons with certain parallel velocities  $v_{\parallel}$ , these processes lead to an asymmetric distribution function, the indication of presence of current drive, seen in figure 2.16.

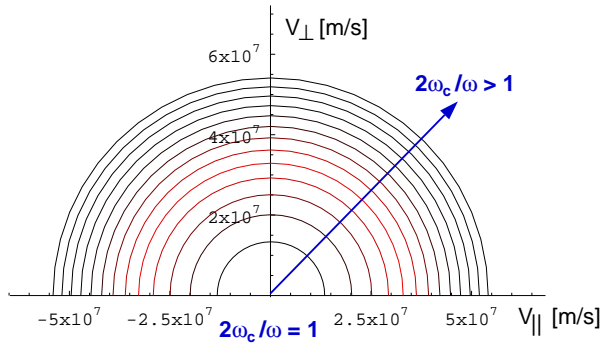


Figure 2.15: Electron heating distribution function in  $v_{\perp} - v_{\parallel}$  diagramme

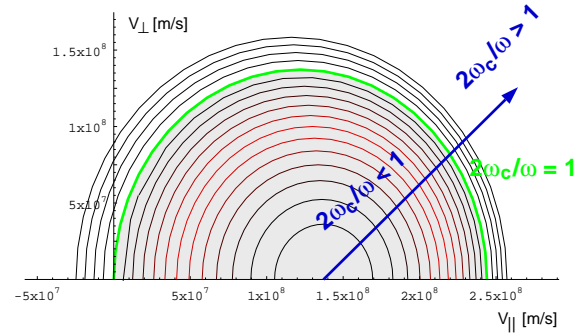


Figure 2.16: Electron current drive distribution function in  $v_{\perp} - v_{\parallel}$  diagramme

In ASDEX Upgrade, the second harmonic of the electron cyclotron frequency in X-mode with

$$2\omega_{ce} = 2 \cdot |e \cdot B| / m_e = 140 \text{ GHz} \quad (2.80)$$

is heated. The cold resonance at  $B = -2.5$  T is located on the magnetic axis as indicated in figure 2.17.

At present, four fixed frequency gyrotrons with a maximum power of 0.5 MW each are available. Pure heating or current drive at different locations can be chosen by positioning a movable mirror. In figure 2.18 the mirrors launching the wave from the low field side in the equatorial midplane of the torus in sector 14 are seen. The maximum angle in poloidal direction is  $\Theta = \pm 32^{\circ}$ , in toroidal direction  $\Phi = \pm 30^{\circ}$ . Variations of the mirror angles and of the magnetic field allow radial, poloidal and toroidal shifts of the deposition location.

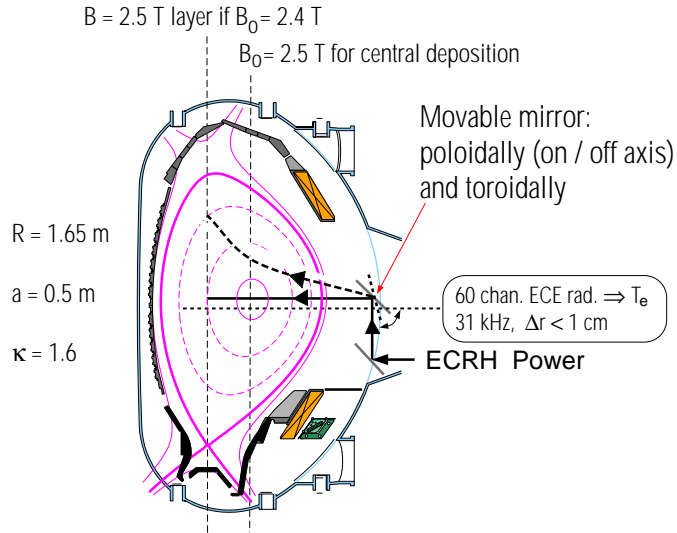


Figure 2.17: ECRH system in ASDEX Upgrade



Figure 2.18: ECRH mirrors

### 2.4.2 TORBEAM Code

To describe the propagation and absorption of electron cyclotron waves in ASDEX Upgrade, or in general in tokamak plasmas, the beam tracing code TORBEAM [28] is used. The wave beams are assumed to have a Gaussian amplitude profile. For frequencies in the electron cyclotron range, the scale length  $L$  of inhomogeneities in the medium is normally much larger than the wavelength  $\lambda$  of the beams:

$$\mu := \frac{\omega L}{c} \gg 1 \quad (2.81)$$

In this limit, the application of geometrical optics is possible. The advantage of geometrical optics lies in the simplification of the problem. Maxwell's equations are reduced to easy and fast to solve first order ordinary differential equations which represent the beam as a bundle of independent rays. However, important wave effects like interference and diffraction are not treated in this simple picture.

Different methods can be used to introduce diffraction, but most of them lead to difficult and complicated equations. The advantage of the beam tracing method [29] is that wave effects can be taken into account, solving again a set of ordinary differential equations. They describe the evolution of the beam axis, the beam width and the curvature of the wave front. The TORBEAM code can be used not only to display the propagation of the wave in the plasma but also to calculate the deposited power and driven current. The discharge #14872 is used as an example in figure 2.19. In figure 2.19 a typical power deposition and current profile can be seen.

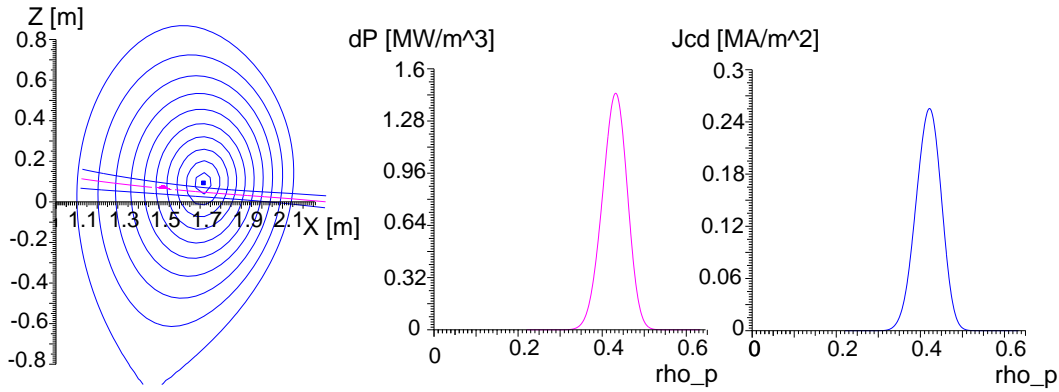


Figure 2.19: TORBEAM results for discharge #14872 at 2.5 s

Discharge #14872 was performed as a part of the investigation of the sawtooth behaviour depending on the ECR deposition (see figure 4.11). The parameters used to calculate figure 2.19 are the gyrotron wave frequency  $\nu = 140$  GHz, total power of two beams at 2.5 s 0.8 MW. The gyrotrons 3 and 4 with the position  $x_0 = 231.1$  cm, the poloidal angle  $\Theta = 5.0^\circ$  and toroidal angle  $\Phi = -15.0^\circ$  were used.<sup>1</sup> The maximum of the power deposition at  $\rho_{pol} = 0.4321$  is found as  $1.45 \text{ MW/m}^3$ , the total driven current 13.5 kA and a maximum current drive of  $0.255 \text{ MA/m}^2$  at  $\rho_{pol} = 0.422$ .

In a nutshell, in discharge #14872, the ECR was deposited off-axis with the amount of total driven ECCD of 13.5 kA in co-direction of the main plasma current.

### 2.4.3 Neutral Beam Heating

Due to the strong magnetic field in toroidally confined plasmas, charged particles cannot penetrate the plasma without being deflected. However, neutral particles are not influenced by the magnetic field until they become ionized. The particles become ionized due to collisions with the electrons and ions in the plasma. These collisions lead on the other hand to scattering and slowing-down of the particles [2]. Particles can be lost due to shine through, which means the neutral particles pass the plasma without getting ionized.

Fast particles can be slowed down by collisions up to thermal energies if they do not hit the wall due to their gyration and drift motion (orbit losses). A further source of losing the injected particles appears due to charge exchange collisions, mainly if neutral gas is filled into the plasma during a discharge. The fast ions collide with neutral atoms, that are always present in a plasma. Due to charge exchange, they become neutralized again and leave the plasma before depositing their energy.

The deposition profile of a neutral beam injection system (NBI) is broad compared with the very localized deposition profile of the ECRH. It is determined by the penetration depth into the plasma of the injected particles, mainly dependent on the plasma density and energy of the

<sup>1</sup>To run TORBEAM correctly, the angles  $\Phi$  and  $\Theta$  have to be multiplied by -1

neutral particles.

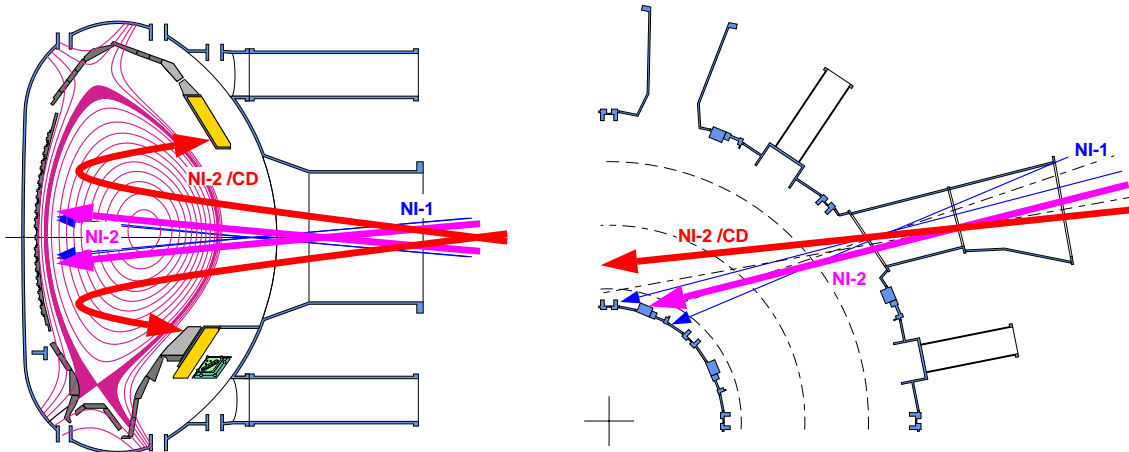


Figure 2.20: NBI geometry Injector one, which refers to source 1-4, and source 5 and 8 of box 2 injects nearly in the midplane. The beams NI 6 and 7 are the most tangential beams with more deposition outside of the plasma centre than the other beams. The injection classification is listed in the previous table. In figure 4.1, the injection is shown in a poloidal cross section.

The NBI, the main heating source in ASDEX Upgrade, is equipped with a maximum power of  $P_{NBI} = 20$  MW. It consists of two beam lines with four ion sources each. The maximum injection power of each ion source is limited to  $P_{source} = 2.5$  MW. One beam line is situated in sector 15, the second in sector 7. The beam line geometry can be seen in figure 2.20. The launching classification is listed in the following table.

Injector	Source	Classification
1, Sector 15	Q1	radial
1, Sector 15	Q2	tangential
1, Sector 15	Q3	tangential
1, Sector 15	Q4	radial
2, Sector 7	Q1 (Q5)	tangential
2, Sector 7	Q2 (Q6)	current drive
2, Sector 7	Q3 (Q7)	current drive
2, Sector 7	Q4 (Q8)	tangential



# Chapter 3

## Soft X-Ray Diagnostic

The radiation of a plasma consists of continuous background radiation, dependent on temperature and density (the so-called bremsstrahlungsspektrum) and the line radiation of partly ionized impurities. The latter will be of no importance in a fusion reactor and will not be treated any further. In the ASDEX Upgrade tokamak, typical core temperatures reach values of  $T_i = T_e = 1...20$  keV. Radiation with energies below  $E = 10$  keV lies in the soft X-ray spectrum, which is measured with pinhole cameras equipped with semiconductor detectors. The use of these semiconductor photo diodes with fast time response, leads to a line-of-sight integrated signal with high temporal resolution.

The measurement of this radiation in the soft X-ray spectrum is a very powerful tool. In this work, the Soft X-Ray (SXR) diagnostic is used to detect sawteeth. During a sawtooth collapse, the central temperature rises until it crashes. Due to the temperature dependence of the SXR signal, the change in the temperature during a sawtooth collapse is seen by the SXR chords like in figure 2.8. At the same time, the temperature outside the inversion radius decreases until it suddenly rises.

A further application of the SXR diagnostic is MHD mode analysis. A combination of the results of the Mirnov coil (MTR) diagnostic with the SXR make reliable mode analysis possible. In this chapter, a short theoretical treatment of the SXR signal is given together with the description of the ASDEX Upgrade SXR system. Finally, the development of a new system, which was carried out during this thesis work, is described.

### 3.1 Theory of the Soft X-Ray Diagnostic

In plasmas, the energy of soft X-rays are of the same order of magnitude as electron kinetic energies. That is why it is actually necessary to take quantum effects into account. This can be done by proper modification of the Gaunt factor  $G$ . However, in this work, as usual, only the classical treatment of bremsstrahlung is taken into account.

The bremsstrahlung of a single electron-ion encounter can be described as the radiated energy  $dW/d\omega$  per unit angular frequency  $\omega$  by solving Maxwell's equations [30]. For a single electron colliding with more ions with the density  $n_i$  in a high-frequency regime, a power

spectrum  $P(\omega)$  can be derived. By factorizing, the frequency dependent part can be separated:  $G(\omega, v) \frac{dP}{d\omega}$ . The frequency and velocity dependent factor  $G(\omega, v)$  is called Gaunt factor and is usually of the order on unity. The frequency independent part is given by

$$\frac{dP}{d\omega} \approx \frac{\pi}{\sqrt{3}} \frac{Z^2 e^6}{(4\pi\epsilon_0)^3} \frac{16n_i}{3m_e^2 c^3 v} \quad (3.1)$$

with the charge number  $Z$  and the electron velocity  $v$ . In a fusion plasma, the treatment of more than one electron encountering ions has to be considered. The radiated power of each single electron  $P(\omega)$  has to be integrated over the velocity distribution of the electrons  $f(\mathbf{v})$ . The power  $j(\omega)$  per unit volume per unit solid angle which is emitted by a plasma for the unit frequency is given as

$$4\pi j(\omega) = \frac{dP}{d\omega} v \int_0^\infty \frac{G(\omega, v)}{v} 4\pi f(v) v^2 dv \quad (3.2)$$

By using a Maxwellian velocity distribution with  $\bar{g}(\omega, T_e[eV])$ , the Maxwell averaged Gaunt factor [31] is defined as

$$\bar{g}(\omega, T_e) = \int_0^\infty G(\omega, E) e^{-(E-\hbar\omega)/T_e} \frac{d(E-\hbar\omega)}{T_e[eV]} \quad (3.3)$$

where  $T_e$  is the electron temperature and  $E$  the electron kinetic energy. With a Maxwellian velocity distribution and the substitution  $E = 1/2m_e v^2$ ,  $G(\omega, E)$  in equation 3.2 can be substituted with  $\bar{g}(\omega, T_e[eV])$  defined in equation 3.3. With  $G(\omega, E) \equiv 0$  for  $E < \hbar\omega$ , the power spectrum can be expressed as

$$4\pi j(\omega) = \bar{g}(\omega, T_e[eV]) n_e n_i \frac{Z^2 e^6}{(4\pi\epsilon_0)^3} \frac{16\pi}{3\sqrt{3}m_e^2 c^3} \left( \frac{2m_e}{\pi T_e[eV]} \right)^{1/2} e^{-\hbar\omega/T_e[eV]} \quad (3.4)$$

while  $n_e$  is the electron density. The dependence of the SXR signal on  $Z$ ,  $T_e$  and  $n$  is obvious. The spectral power emitted into the complete solid angle per unit frequency  $4\pi j(\omega)$  is proportional to the emissivity  $\epsilon$  [32], [30], [33]. The emissivity is defined as the radiation energy density per time and frequency interval. In the plasma (except at the edge), the bremsstrahlung forms the main part of the emissivity:

$$\epsilon_{brems, \nu} \sim \frac{Z_{eff} n_e^2}{\sqrt{T_e}} e^{-\hbar\nu/k_B T_e} \quad (3.5)$$

where the effective ion charge  $Z_{eff}$  is defined as

$$\sum_i n_e n_i Z_i^2 = n_e^2 Z_{eff}^2 \quad (3.6)$$

To calculate the actual signal from a detector, the reduction of the signal due to absorption by filtering has to be taken into account. All cameras are equipped with a beryllium filter with different thicknesses of 8  $\mu\text{m}$  and 100  $\mu\text{m}$  for the previously existing cameras, with the single diodes and 75  $\mu\text{m}$  for the new MiniSoX cameras (see section 3.3). Dependent on the thickness

of the beryllium foil, different radiation energies are filtered. The absorption probability  $W$  can be defined as (compare with [32]):

$$W(E) = e^{-\mu_{Be}(E)d_{Be} - \mu_{Al}(E)d_{Al} - \mu_{Si}(E)d_{p^+}} \cdot \left(1 - e^{-\mu_{Si}(E)d_n}\right) \quad (3.7)$$

As included in equation 3.7, the radiation is not only filtered by the beryllium foil of thickness  $d_{Be}$  but also by the aluminium electrode of thickness  $d_{Al}$  and the  $p^+$  layer on the silicone diode of thickness  $d_{p^+}$ .  $d$  is used as layer thickness and  $\mu$  the corresponding absorption coefficients for beryllium  $\mu_{Be}$ , for aluminium  $\mu_{Al}$  and for silicone  $\mu_{Si}$ . The total emissivity, including the filter corrections, is written as

$$\tilde{\epsilon}_{brems} = \int_0^\infty \epsilon_{brems,\nu} W(h\nu) d\nu \quad (3.8)$$

$$\tilde{\epsilon}_{brems} \sim Z_{eff} n_e^2 T_e^x \quad (3.9)$$

The variable  $x = d(\ln \tilde{\epsilon}_{brems})/d(\ln T_e)$  is dependent on the electron temperature and can be calculated using equation 3.8. With  $T_e = 3$  keV and  $d_{Be} = 100 \mu\text{m}$ ,  $x$  can be calculated numerically to  $x = 1.2$  [32].

Usually, the recombination radiation is negligible in the soft X-ray range of fusion plasmas. For a more detailed description, see [30].

## 3.2 Soft X-Ray Diagnostic in ASDEX Upgrade

The soft X-ray emission is measured by semiconductor diodes. The signal is amplified by a preamplifier with the variable amplification  $16^{0...3}$  and a main amplifier with amplification  $2^{0...8}$ . An analog to digital converter ADC creates a digital 12 bit signal with a sampling rate of 500 kHz. The maximum temporal resolution follows to  $2 \mu\text{s}$ . The data is stored with transputers. Due to the limited data storage possibilities of the transputer system, the data is reduced by a programmed pattern before being stored. For more details see [32], [34].

The Soft X-Ray Diagnostic (SXR) in ASDEX Upgrade is situated in the vessel in sector 5. In figure 3.1, the setup of the cameras up to March 2002 can be seen. The system in figure 3.1 consisted of five cameras with Eurisysemiconductors in two sizes, with the surface of an active layer  $D_1 = 2.6 \text{ mm} \cdot 8.6 \text{ mm}$  and  $D_2 = 2.6 \text{ mm} \cdot 20 \text{ mm}$ , especially designed for this purpose:

Camera A	30 diodes	$D_2 = 2.6 \text{ mm} \cdot 20 \text{ mm}$
Camera B	30 diodes	$D_1 = 2.6 \text{ mm} \cdot 8.6 \text{ mm}$
Camera C	60 diodes	$D_2 = 2.6 \text{ mm} \cdot 20 \text{ mm}$
Camera D	30 diodes	$D_1 = 2.6 \text{ mm} \cdot 8.6 \text{ mm}$
Camera E	12 diodes	$D_1 = 2.6 \text{ mm} \cdot 8.6 \text{ mm}$

The cross section of a camera is seen in figure 3.2. Single diodes are mounted radially around the pinhole. This setup is very flexible due to the separate diodes. Unfortunately, the diodes

suffer from ageing, most probably due to neutron damage. The signal starts drifting and loses high frequency resolution.

The B- and C-cameras were dismantled in August 2003. All cameras, including B and C-cameras, would have needed a diode replacement in order to record useful data after the opening. The replacement of these diodes would have been very expensive, a disadvantage of these single diodes. The decision was made not to exchange the diodes, but to design a completely new SXR system with cheaper planar Centronics diode chips, containing 35 diodes. A new SXR system has been set up, consisting currently of three triple chip MiniSoX cameras, described in more detail in section 3.3. An upgrade to five cameras is planned in 2004. The cost of the new design is equivalent to about three complete replacements of all Eurisys diodes. A camera equipped with the Centronics chip will have a worse resolution and intensity due to its smaller size and its plane setup, compared with the Eurisys diodes. But due to the low cost of one detector chip, one can easily exchange all diode chips in every opening to minimize the ageing problem. The maintenance of the new system is far cheaper than the previously existing one and additionally, the camera size is smaller.

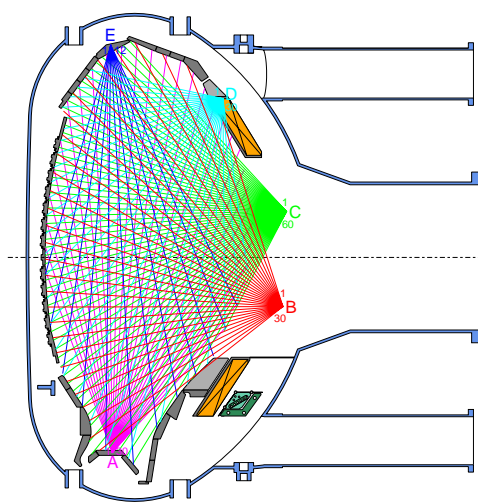


Figure 3.1: Toroidal cross section: Setup of former SXR cameras

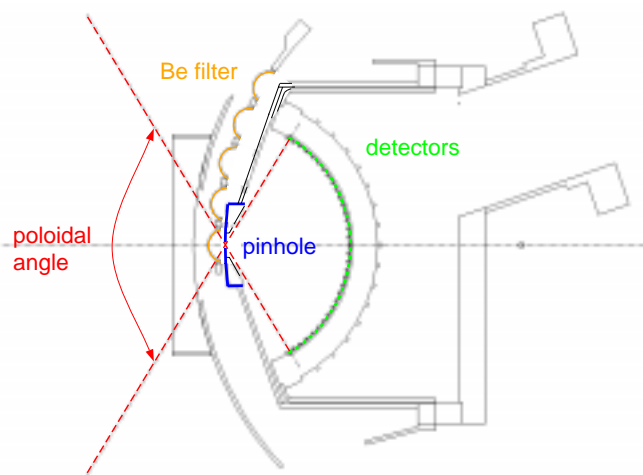


Figure 3.2: Detailed setup of previous SXR system

In March 2002, the first triple chip MiniSoX test system was included, as described in the following section 3.3.

### 3.3 Development of a New SXR System

The diodes used in the previously existing system have advantages such as flexibility, high resolution and high intensity. However, the diodes suffer strongly from probably neutron damage. In other experiments such as JET for example, the diode chip Centronix LD35-5T (window-less) is used. This planar chip with 35 mounted diodes is easy to exchange and is about half

the cost of one single Eurisys detector. Because of its far lower cost compared to the previous Eurisys diodes, one can exchange this chip easily during every opening of the vacuum vessel. The problem of the ageing of the semiconductor material due to radiation damage is reduced. A second option could be the plane Centronics chip AXUV20. The diode size is even smaller than the LD35-5T, which allows a more compact construction inside the vessel, but would lead to a further decrease in resolution and intensity. The AXUV20 is foreseen for the SXR system in the Wendelstein 7-X experiment, currently under construction in Greifswald, Germany. The diode chip Centronix LD35-5T (windowless) was decided to be used in ASDEX Upgrade due to its slightly higher resolution and intensity.

### 3.3.1 Calculation of Camera Geometry

As described in [31], the power  $P$  seen by a detector along a line of sight is given by

$$P(p, \phi) = f \int_{L(p, \phi)} \varepsilon(r, \theta) dL \quad (3.10)$$

where  $\varepsilon$  is the local emissivity,  $p$  the impact parameter,  $r$  the distance from the toroidal axis,  $\theta$  the poloidal angle and  $\phi$  the angle of the line of sight (compare figure 3.3). The so-called Etendue  $f$  is a correction factor due to the detector and pinhole geometry.  $f$  is used to obtain the power of the diodes referred to as brightness or intensity.

The camera geometry is described by the diode surface  $D = d_1 \cdot d_2$ , where  $d_1$  and  $d_2$  are the diode width and length, by the pinhole surface  $B = b_1 \cdot b_2$  with the width and length  $b_1$  and  $b_2$ , the focal length  $\Delta$  and the distance plasma-detector  $L_p$ .

If the diode surface is sufficiently small, so that the whole diode area can be assumed to be uniformly irradiated, the Etendue is defined as

$$f = \underbrace{\frac{1}{4\pi} \frac{d_1 \cdot d_2 \cdot b_1 \cdot b_2}{\Delta^2}}_{f'} \cos^4 \alpha \quad (3.11)$$

where  $\alpha$  describes the angle between perpendicular incidence through the pinhole and the incidence on the detector  $n$  through the pinhole (compare with [31]).

$f'$  is used in the following to interpret the intensity of the central diode of a chip. The intensity should be maximized by a SXR system. However, there are two mutually contradictory demands on the system. On the one hand, the intensity of the SXR system should be maximized whilst on the other the resolution should also be maximized. The broader the line of sight, the

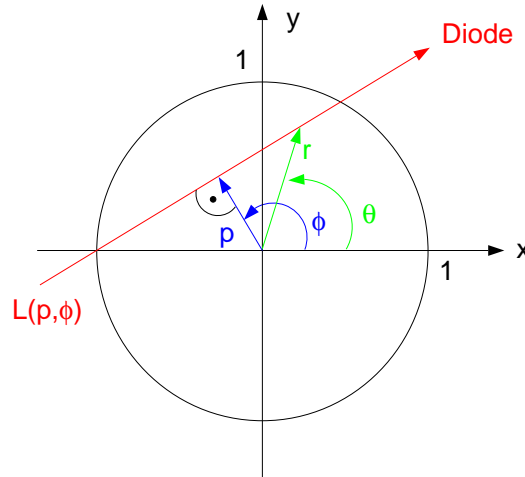


Figure 3.3:  $(p, \phi)$  diagram of the new MiniSoX cameras

larger the intensity and the bigger the resolved volume. In the case of big resolution volume, the lines of sight overlap and give less independent information.

In figure 3.4 a sketch is drawn of the parameters describing the position of the diode, the pinhole and the plasma centre. By using the trapezoid formula, one can calculate the poloidal

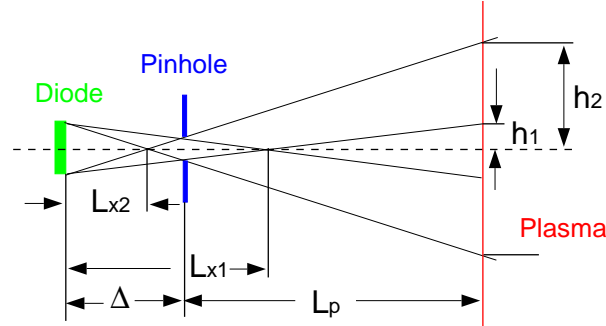


Figure 3.4: Sketch of the minimum resolution  $2 \cdot h_1$  and the maximum resolution  $2 \cdot h_2$

resolution  $h_{1,2}$  and toroidal resolution  $g_{1,2}$  of the central diode of the Centronics diode chip LD-35T, e.g. for  $h_2$

$$\frac{2h_2}{d_1} = \frac{L_p + \Delta - L_{x2}}{L_{x2}}, \quad \frac{d_1}{2L_{x2}} = \frac{b_1}{2(\Delta - L_{x2})} \quad (3.12)$$

The maximum and minimum poloidal resolution is defined as  $2 \cdot h_1$  and  $2 \cdot h_2$  and can be transformed to

$$h_1 = \frac{1}{2} \cdot d_1 - \frac{1}{2} \cdot (d_1 - b_1) \cdot \frac{\Delta + L_p}{\Delta} \quad (3.13)$$

$$h_2 = -\frac{1}{2} \cdot d_1 + \frac{1}{2} \cdot (d_1 + b_1) \cdot \frac{\Delta + L_p}{\Delta} \quad (3.14)$$

with the minimum resolution  $2 \cdot h_1$ , the maximum resolution  $g_{100\%} = 2 \cdot h_2$ , the focal length  $\Delta$  and the distance  $L_p = 620$  mm of the pinhole to the plasma centre. By using the toroidal or poloidal length of the diode  $d_1$  or  $d_2$  and the pinhole  $p_1$   $p_2$ , the poloidal and toroidal resolution can be found. The toroidal resolution can be calculated in the same way, in the formulas 3.13 and 3.14  $h_1, h_2$  have to substituted with  $g_1, g_2$  and  $d_1, b_1$  with  $d_2, b_2$ .

The maximum toroidal mode number  $m$  and poloidal mode number  $n$ , that can be resolved, is found if half the wavelength of the mode  $\lambda_{min}$  is equal to the maximum resolution  $g_{100\%} = \frac{1}{2} \cdot \lambda_{min}$ .

$$m_{max} = \frac{2\pi r_1}{\lambda_{min}} \quad (3.15)$$

with  $r_1 = r_{q=1}$ . At or close to the  $q = 1$  surface usually strong modes appear.  $r_1$  is estimated to  $r_1 = 150$  mm

$$n_{max} = \frac{2\pi R_0}{\lambda_{min}} \quad (3.16)$$

with  $R_0 = 1700$  mm the major radius. An overview over the resolution in mm is shown in the following table. For the MiniSoX camera, the etendue for the central diode is shown.

**B-camera  $d_1 = 2.6$  mm,  $d_2 = 8.6$  mm and C-camera  $d_1 = 2.6$  mm,  $d_2 = 20.0$  mm**

Camera	pin.width in [mm]	pin.length in [mm]	foc.length in [mm]	pol.res. in [mm]	tor.res. in [mm]	Etendue $f'$	$m$	$n$
B	2.5	18	69.7	47.8	254.6	$16 \cdot 10^{-3}$	10	20
C	2.5	35	141	25	276.8	$18 \cdot 10^{-3}$	19	20

**MiniSoX: Centronics chip with 35 diodes à  $d_1 = 0.96$  mm,  $d_2 = 4.5$  mm**

Camera	pin.width in [mm]	pin.length in [mm]	foc.length in [mm]	pol.res. in [mm]	tor.res. in [mm]	Etendue $f'$	$m$	$n$
first	0.3	5	18	43.7	332.2	$1.6 \cdot 10^{-3}$	11	16
second	0.5	5	18	50.8	332.2	$2.7 \cdot 10^{-3}$	9	16
	0.2	9	14	51	607	$3.2 \cdot 10^{-3}$	9.2	11
final	0.3	9	14	56.1	607	$4.7 \cdot 10^{-3}$	8.5	11
	0.4	9	14	60.6	607	$6.3 \cdot 10^{-3}$	7.8	11

MiniSoX cameras as described “first” in the table above were in use in Wendelstein-7AS. As a first test, a copy of these cameras was installed in ASDEX Upgrade. In comparison with the B- and C-camera, the resolution is comparable, but the intensity, represented by the “Etendue”, is worse by a factor of ten. To increase the intensity, the pinhole width was opened in “second”. Unfortunately, only the poloidal pinhole width was adjustable and opened as far as possible. To improve the intensity, it would have been better to increase the toroidal pinhole width. In this case, the poloidal resolution remains while the toroidal one decreases.

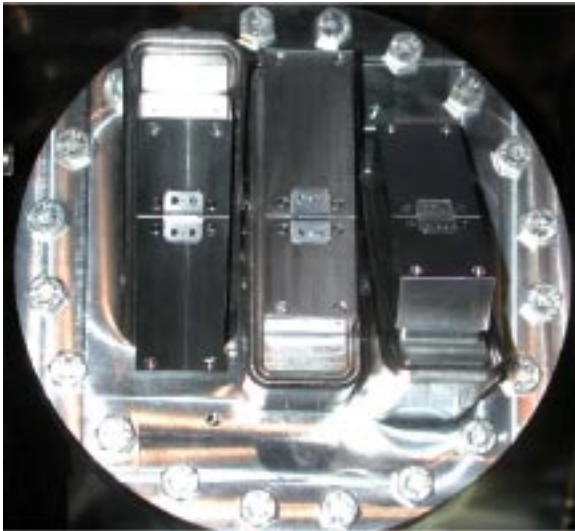


Figure 3.5: Triple chip MiniSoX camera

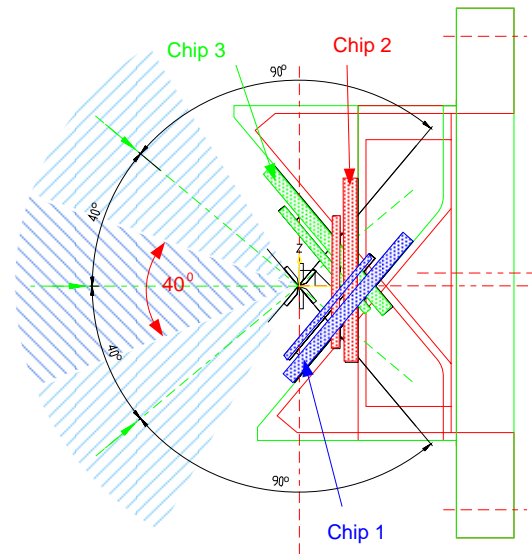


Figure 3.6: Sketch of new MiniSoX camera

However, the toroidal resolution is far higher than the poloidal one. It is a good compromise to obtain a higher intensity by losing toroidal resolution. A further method to improve the intensity is to decrease the focal length but at the expense of resolution. The focal length of the camera is already far smaller compared to the cameras B and C, as seen in the table above. A finite camera size is required, to finally build and assemble the camera. The “final” camera design is listed in the table above. The focal length is decreased for higher intensity while the pinhole length is increased to gain even more intensity without losing the poloidal resolution. In the table in the line above and below “final”, the changes in the resolution are listed due to two variations in the pinhole width.

In equation 3.11, the factor  $\cos^4\alpha$  is equal to the one for the central diode. Because of the planar diode chip, the effective diode surface and effective pinhole width decrease, the greater the distance from the diode to the pinhole. This change in the effective parameters is represented by the factor  $\cos^4\alpha$ . In addition to the decrease in intensity because of the chip geometry, the outer diodes usually see less radiation, because the outer part of the plasma is colder than the centre.

To increase the intensity, only 15 of 35 diodes are in use on each diode chip. Instead, one camera consists of three chips, placed toroidally next to each other as seen in figure 3.5. In a poloidal cross section, as seen in figure 3.6, the three cameras share the pinhole. They are rotated by  $40^\circ$  around this pinhole. To further optimize the intensity, a thinner filter is chosen compared to the previously existing cameras. The  $100\ \mu\text{m}$  filter is replaced with one of a  $75\ \mu\text{m}$  thickness. Due to equation 3.7 in section 3.1, the throughput and with it the intensity increases.

After the data acquisition, the three ‘sub-cameras’ are resorted and united via software to one

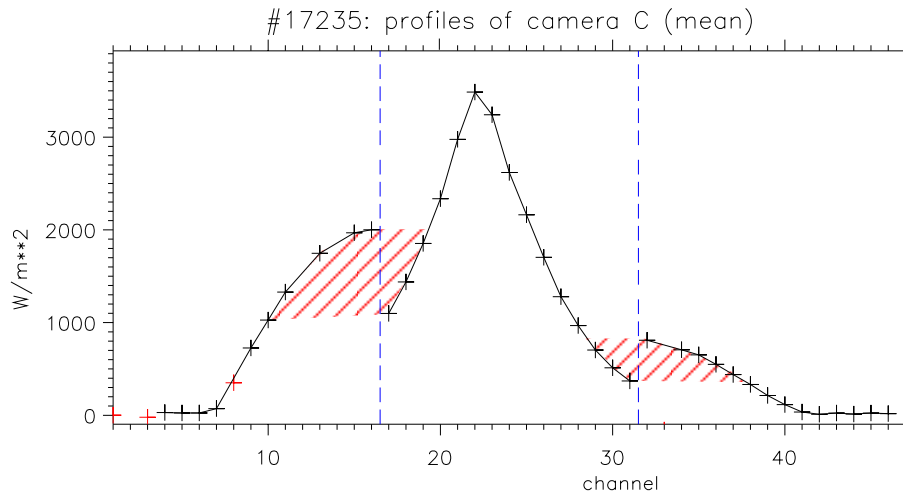


Figure 3.7: Profiles of the three different diode chips of the triple chip MiniSoX test system. On the right and left side of the dashed lines, marked by the shaded area, channels are seen in the same emissivity range. These are overlapping channels.

camera. Three diodes of each chip are chosen to overlay in order to find the exact relative position of the chips. These overlapping channels are marked by a shaded area in figure 3.7. The test system of the triple chip MiniSoX camera was successfully installed in April 2002. In

figure 3.7, the intensity of the three chips of the test system are seen separately. In figure 3.8 a wavelet plot with the mode frequencies over time is shown.

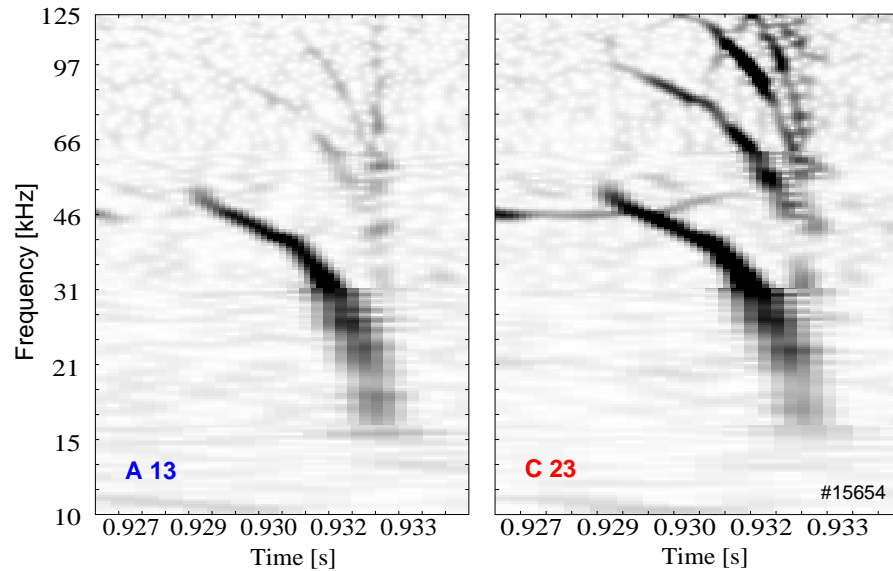


Figure 3.8: Comparison of a wavelet plot of the same discharge for a central diode of the A and MiniSoX camera; now labelled as C camera

The discharge was run at the end of April 2002. It is clearly seen, that the A camera shows high frequency modes with far less intensity than the new MiniSoX camera. This is probably due to neutron damage of the diode of the A camera. The camera was set up with new diodes in March 2001. Because of the successful test system, a complete new system consisting of five triple chip cameras is currently under construction. They will be placed in sector 11 at the same toroidal co-ordinate, poloidally displaced.

Three cameras are planned to be put into operation in autumn 2003. The position of the new cameras is seen in figure 3.9 with a flux surface close to the separatrix. Each chip refers to a different colour. In figure 3.10, a  $(p, \phi)$  diagramme is shown.

$p$  is the impact parameter and  $\theta$  the poloidal angle for a viewing chord, outlined in figure 3.3. A  $(p, \phi)$  diagramme shows the cover of the plasma with lines of sight. The more area is covered and the more regularly spread the points are, the higher the possible resolution for a tomographic reconstruction. Each cross in figure 3.10 refers to a chord in figure 3.9 marked with the same colour. The curve between 500 mm and 800 mm indicates the border of the flux surface seen in figure 3.9. No points are currently available right now around the angle  $\theta = 180^\circ$ . More cameras are planned to be integrated in the vessel in summer 2004. They are planned to be placed to fill the empty region in the  $(p, \phi)$  diagramme.

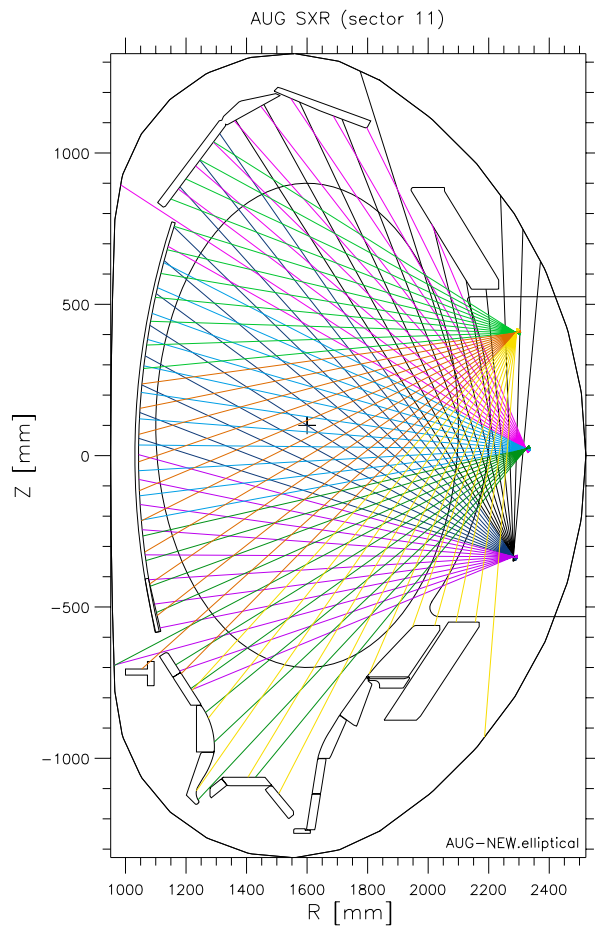


Figure 3.9: New MiniSoX cameras in sector 11

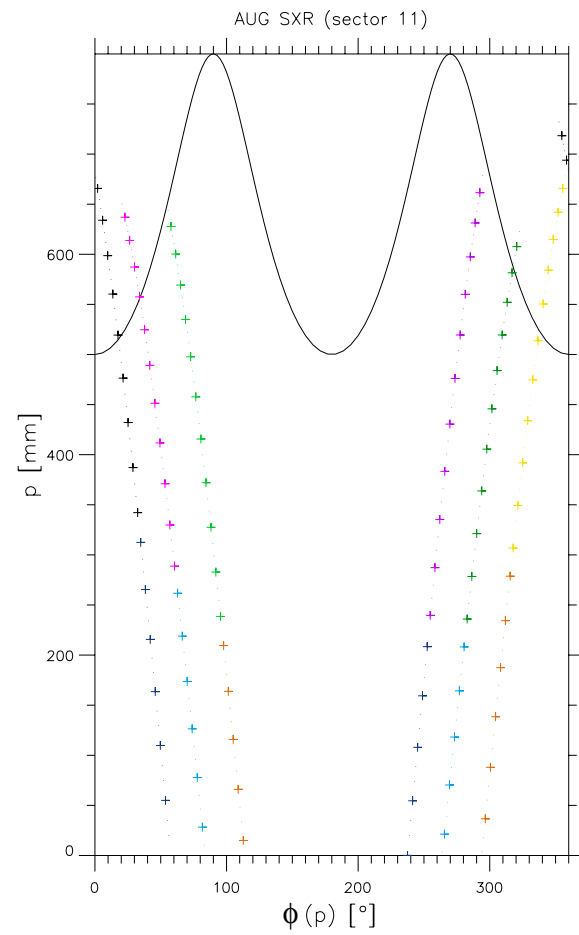


Figure 3.10:  $(p, \phi)$  diagramme of the new MiniSoX cameras

# Chapter 4

## Sawtooth Stabilization Experiments

It is well established that fast particles have a stabilizing effect on sawteeth [19]. Based on these results, the  $\alpha$ -particles created in D-T fusion processes are expected to lead to sawtooth stabilization. These long sawtooth periods might act as a trigger for neoclassical tearing modes (NTMs). The plasma  $\beta$ , a value measuring the efficiency of the confinement of the plasma pressure by the magnetic field, is limited by these NTMs. On the other hand, sawteeth can be used to remove helium ash or impurities from the plasma centre. The goal of this work is to investigate how to control the sawtooth instability. In the following, lengthening of the sawtooth period is called sawtooth stabilization while a decrease in the sawtooth period is named sawtooth destabilization. The occurrence of an MHD mode is called mode destabilization. If the mode amplitude can be decreased, the mode is stabilized.

Recently, it was demonstrated at JET [26] in a neutral beam heated plasma in the high confinement regime (H-mode) that sawteeth can be influenced by ion cyclotron current drive (ICCD). However, the control of the Ion Cyclotron Resonance Frequency (ICRF) deposition is more difficult than with electron cyclotron heating (ECRH) or current drive (ECCD), which provides the possibility of very localized deposition. Modelling can be done at ASDEX Upgrade using the beam tracing code TORBEAM [28], see section 2.4.2. In TCV, the influence of ECCD was investigated [35] in the low confinement regime (L-mode). However, in terms of ITER, sawtooth tailoring with ECCD in the high confinement regime (H-mode) in presence of fast particles is of high interest.

In the following section, experiments are shown with NBI used as the main heating source with  $P_{NBI} = 5$  MW, in Deuterium plasmas. With a plasma current of  $I_p = 0.8$  MA and densities about  $n_e = 6 \cdot 10^{19} \text{ m}^{-3}$ , the discharges are well over the H-mode threshold. The normalized beta reaches values of about  $\beta_N \approx 1.7$ .  $\beta_N$  is chosen relatively low because for  $\beta_N$  values over  $\beta_N \approx 2.5$ , the triggering of NTMs becomes probable. However, the triggering of NTMs would disturb the sawtooth behaviour.

## 4.1 Influence of Sawteeth with NBI

ASDEX Upgrade is equipped with a neutral beam injection (NBI) system with a maximum heating power of  $P_{NBI} = 20$  MW, see section 2.4.3. The NBI system consists of two beam boxes with four sources each, seen in figure 4.1. The sources vary in tangential and radial injection. Due to this difference, the sawtooth behaviour changes dependent on the chosen NBI sources. In the discharge in figure 4.2, all eight beam sources are used separately for about 1 s each, with a plasma current of 0.8 MA, 2.5 MW NBI power, densities of about  $6.3 \cdot 10^{19} \text{ m}^{-3}$  and a -2.4 T magnetic field. These plasma parameters are very similar to those used in the following experiments. Even with one beam source with  $P_{NBI} = 2.5$  MW, the H-mode regime is reached.

Injector one, which refers to source 1-4, and source 5 and 8 of box 2 injects nearly in the midplane. The beams NBI 6 and 7 are the most tangential beams with more deposition outside of the plasma centre than the other beams. The injection classification is listed in the following table. In figure 4.1, the injection is shown in a poloidal cross section.

NBI	ST period	orientation	midplane
source 1	42ms	radial	lower
source 2	45ms	tangential	lower
source 3	60ms	tangential	upper
source 4	46ms	radial	upper
source 5	35ms	tangential	lower
source 6	200ms	current drive	lower
source 7	300ms	current drive	upper
source 8	45ms	tangential	upper

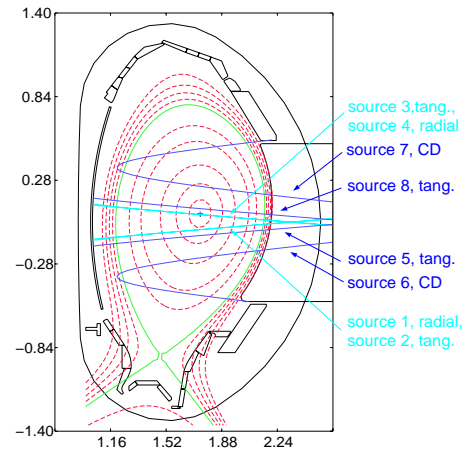


Figure 4.1: Equilibrium with beam position in #16617 at 5s

In figure 4.2, the beams NBI 6 and 7 show clearly the strongest stabilizing effect on the sawteeth. This effect cannot be explained by the well known sawtooth stabilization of trapped fast particles [19]. The more tangential the injection angle the less fast trapped particles are created. If the trapped fast particle stabilization was the dominant process, source 6 and 7 would have the shortest sawtooth period. However, the opposite effect is observed. Neither can the difference in the heating profiles of the on- and off-axis beams explain this specific increase in the sawtooth period. Because of the up shifted plasma centre, the heating profiles of source 1 (central, radial) and 7 become comparable, but the behaviour of the sawtooth period strongly differs.

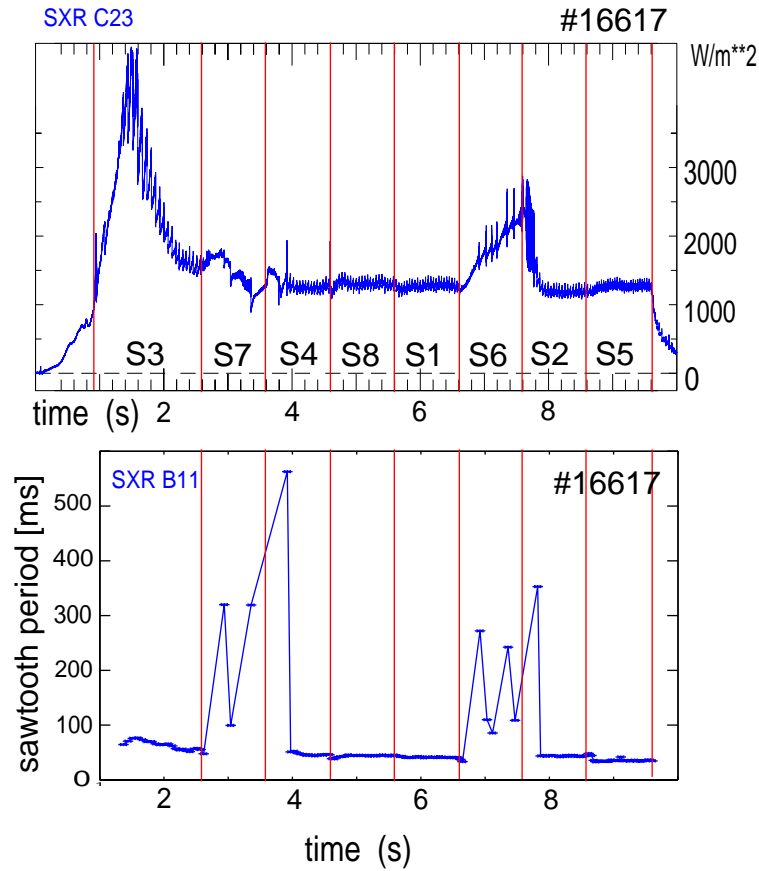


Figure 4.2: Influence of different NBI sources on sawtooth behaviour. Clear change in sawtooth behaviour for most tangential beam sources 6 and 7 with off-axis deposition.

The fast particle pressure gradient can also not explain the observed effect. As seen in figure 4.3, the gradients of the perpendicular and parallel fast particle pressure at the sawtooth inversion radius change with the NBI sources. Expressed in the toroidal flux co-ordinate  $\rho_{tor}$ , the sawtooth inversion radius is situated roughly at  $\rho_{tor} \approx 0.15$ . The sources 3, 7, 4 and 8 show a clear negative gradient which should have a stabilizing effect on the sawteeth compared with source 1 that shows a slight positive gradient. The sources 2, 6 and 7 show a nearly flat fast particle pressure profile at  $\rho_{tor} \approx 0.15$ . The current drive sources 6 and 7 show no particular difference in the fast particle pressure that could lead to an explanation of the change in the sawtooth period at least of source 6.

The sawteeth of source 6 have a well developed triangular shape while for source 7, the sawtooth behaviour does not reach steady state in the time interval. No clear sawtooth shape and period can be seen. The rise in the SXR signal for source 6 can be explained by an increase in density. However, due to neutral beam current drive [36] with the far off-axis source 6, the current profile flattens in the centre which has a stabilizing effect on the sawteeth. This resistive effect explains the long time scale of about 300 ms until the sawteeth find a regular shape and period with a different neutral beam source like source 2 after the switch-off of source 6.

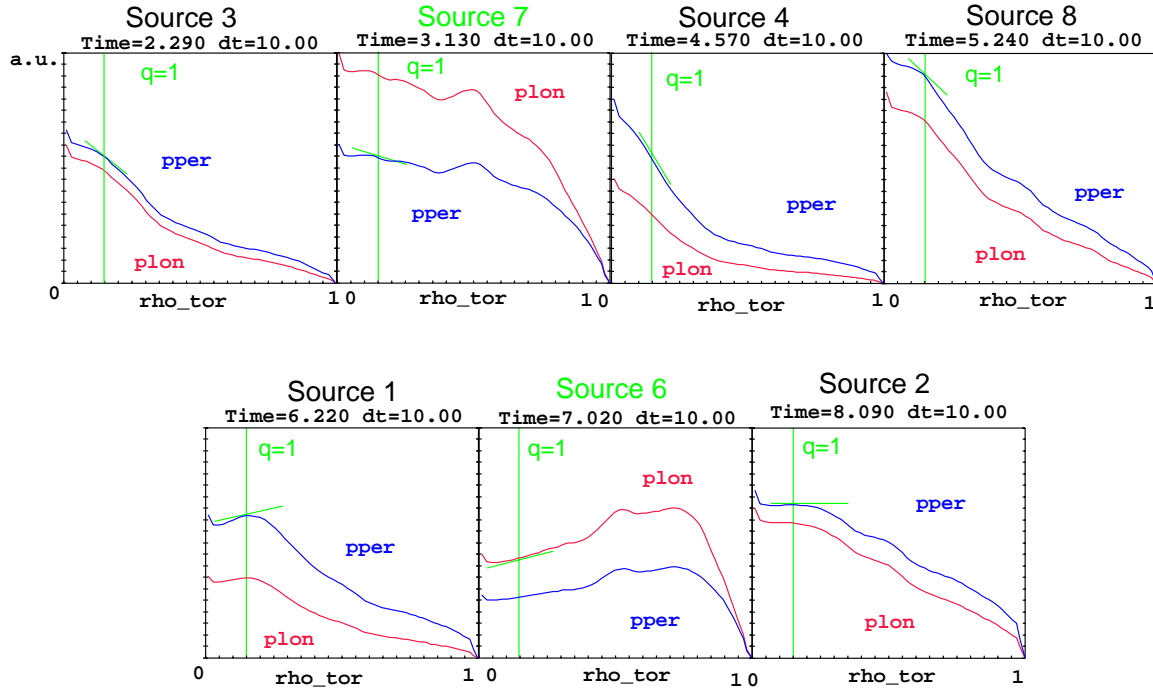


Figure 4.3: Perpendicular (ppper) and longitudinal (plon) fast particle pressure for different beam sources. No clear difference for source 6 and 7 compared to the other sources.

## 4.2 Influence of Co-ECCD on Sawteeth

In the following experiments, systematic sweeps from the high field side (HFS) to the low field side (LFS) for ECRH, co-ECCD are performed with about  $P_{ECR} = 0.8$  MW of ECRH power, provided by two gyrotrons. The cold Electron Cyclotron Resonance (ECR) condition  $\omega_{ce} = |e| \cdot B/m_e$  shows a linear dependence of the ECR deposition location with the magnetic field. For the second harmonic X-mode, the cold resonance lies at  $B = 2.5$  T in the plasma centre. Due to the magnetic field dependence of the electron cyclotron resonance, the deposition location of the ECR can be shifted by magnetic field ramps during a discharge. The sweep is carried out in several discharges. By field variations from about  $-2.05$  T to  $-2.65$  T, the ECRH deposition is varied from  $\rho_{pol} \approx -0.6$  on the high field side (HFS) out to  $\rho_{pol} \approx 0.3$  on the low field side (LFS). Negative values in  $\rho_{pol}$  are introduced to differ between HFS and LFS. The deposition location is calculated with the TORBEAM beam tracing code [28] as described in the section 2.4.2.

The following discharges are performed with ECR injection in the direction of the main plasma current, co-ECCD. The angles of the ECR mirrors are set to  $-15^\circ$  in toroidal direction to drive current and to approximately  $+5^\circ$  in poloidal direction to deposit close to the midplane. Not in all pulses the same NBI sources are used (see [40]) leading to jumps between two pulses. To filter the NBI geometry effect described above, the sawtooth period is normalized with the

sawtooth period of discharges without ECR and the same NBI sources:  $\tau = \frac{\tau_{NBI+ECR}}{\tau_{NBI\_without\_ECR}}$ . In the experiments presented here, the sawtooth period without ECR lies usually in the range of 100 ms, depending on the chosen NBI sources. The scans without normalization can be seen in the appendix D.1 showing the actual sawtooth period in [ms]. In the following sawtooth period graphs, negative values for  $\rho_{pol}$  are chosen to distinguish between high field side (HFS) and low field side (LFS) with  $\rho_{pol} > 0$ . In figure 4.4, a maximum in the sawtooth period with  $\tau \approx 320$  ms can be observed at  $\rho_{pol} \approx -0.42$  while for deposition inside the inversion radius, marked with a green line, a decrease in the sawtooth period is observed with  $\tau \approx 50$  ms.

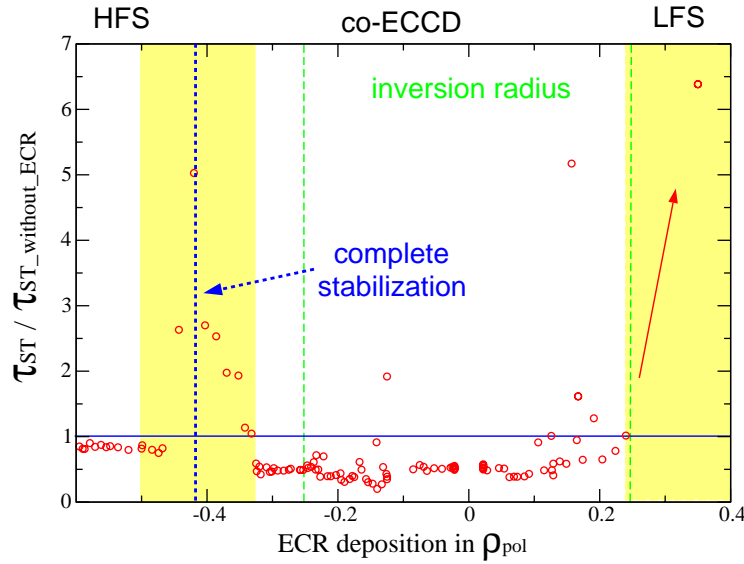


Figure 4.4: ECR deposition in  $\rho_{pol}$  over sawtooth period and sawtooth amplitude with co-ECCD. A maximum in the sawtooth period is observed at  $\rho_{pol} \approx 0.42$  while inside the sawtooth inversion radius, marked in green, the sawtooth period can be decreased.

To investigate the behaviour of the minimum sawtooth period with the ECR power, a gyrotron power ramp up is performed. It is found that the minimum in the sawtooth period with on-axis co-ECR deposition can be even further decreased. However, the shape of the sawteeth is changed. Figure 4.5 shows that the dependence of the sawtooth period on the ECR power. In #16731, the ECR power is varied from 0.8 MW to 1.6 MW in six steps. During the sawtooth destabilization, the sawtooth period is far smaller than the confinement time of about  $t_{conf} \approx 70$  ms. Usually, a change in the sawtooth shape is observed with sawtooth periods in the range of the confinement time [38],[39].

To find out if complete stabilization can be achieved with less ECR power for off-axis deposition at  $\rho_{pol} \approx -0.42$ , a gyrotron power scan is performed. The ECR is deposited in the maximum of the sawtooth period, as found in the toroidal magnetic field scans shown in figure 4.4. The power scan is performed in two discharges, in the first one ramped from 0 MW to 0.42 MW in figure 4.7. The sawtooth period is clearly increasing with power. Pulse #16729 in figure 4.8 continues the scan from 0.42 to 0.8 MW. The power scans are using the NBI sources

3 and 7, one on and one off-axis source. No complete stabilization is observed in the power scan discharges, indicating that at least the power of two gyrotrons  $P_{ECR} \approx 0.8$  MW is needed. To be able to compare all power scans, the scans are all neutral beam heated using the sources 3 and 7. However, complete stabilization is shown in figure 4.9 using the sources 3 and 6. The combination of the sources 3 and 6 might have a more stabilizing effect on the sawteeth than the combination of the sources 3 and 7, even that in both cases a central beam source is combined with a tangential off-axis source. This will be investigated further in future.

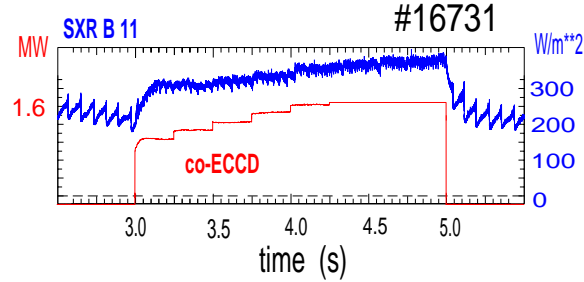


Figure 4.5: Gyrotron power ramp up with central deposition. The sawtooth period can be further decreased with increasing ECR power.

In figure 4.9, in pulse #14987, using source 3 and 6, stabilization for 2 s could be shown, the maximum available ECR pulse length in ASDEX Upgrade. Here, one little sawtooth appears, however, this discharge was repeated several times without showing any sawteeth at all. To show the complete stabilization, a constant field discharge is presented in figure 4.9 with deposition at  $\rho_{pol} \approx -0.42$ . The amount of injected ECR power is only a small fraction of the total heating power, namely 15%. The total driven current of  $I_{ECCD} = 24$  kA, calculated with a TORBEAM simulation, is sufficient to completely stabilize the sawteeth. During this stabilization, the (1,1) mode is still present in form of (1,1) fishbone activity. The fishbones are clearly seen as rapid frequency drops in the lower wavelet plot in figure 4.9. However, the mode amplitude is decreasing with the ECR pulse from 3.9% to 1.4% and recovers after the end of the ECR pulse.

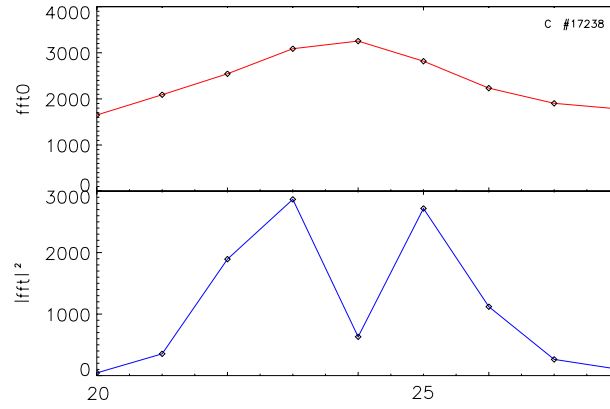


Figure 4.6: The zero component of the FFT, the emissivity, is followed by the first component, the relative amplitude, shown over the channel number of the diodes of the C camera. The mode seen is an  $m = 1$  mode.

The SXR amplitude can be normalized by the intensity  $2|fft/fft0|$  as the ratio of the first and the zero component of a Fast Fourier Transformation (FFT) (compare with the appendix E). However, this amplitude is not absolute, because it does not take the slope of the zero component of the FFT into account, which means the peakedness of the signal. For the C camera, the absolute amplitude of the (1,1) mode is given by the first FFT component divided by the slope of the zero FFT component (in  $\rho_{pol}$ ) at the  $q = 1$  position (absolute amplitude = relative amplitude/ $[\Delta FFT0/\Delta\rho_{pol}]|_{q=1}$ ).

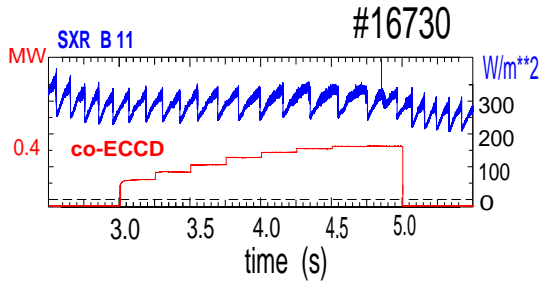


Figure 4.7: Gyrotron power ramp up from zero to 0.4 MW with off-axis deposition. An increase of the sawtooth period with ECR power is seen.

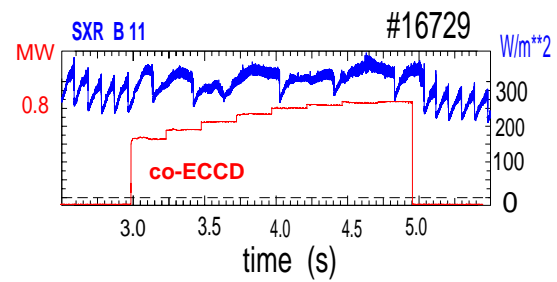


Figure 4.8: Gyrotron power ramp up from 0.4 MW to 0.8 MW with off-axis deposition. A further increase of the sawtooth period with ECR power is seen.

The local driven current is expected to change the shear locally. For co-ECCD deposition slightly outside the  $q = 1$  surface, the current gradient and with it  $q'$  is expected to decrease. This has a stabilizing, which means lengthening, effect on the sawtooth period. Inside the  $q = 1$  surface, the current gradient and with it  $q'$  is expected to increase which leads to a destabilizing, shortening, effect on the sawtooth period. The modelling of the stabilization discharge of figure 4.9 with the ASTRA transport code is found in chapter 6.

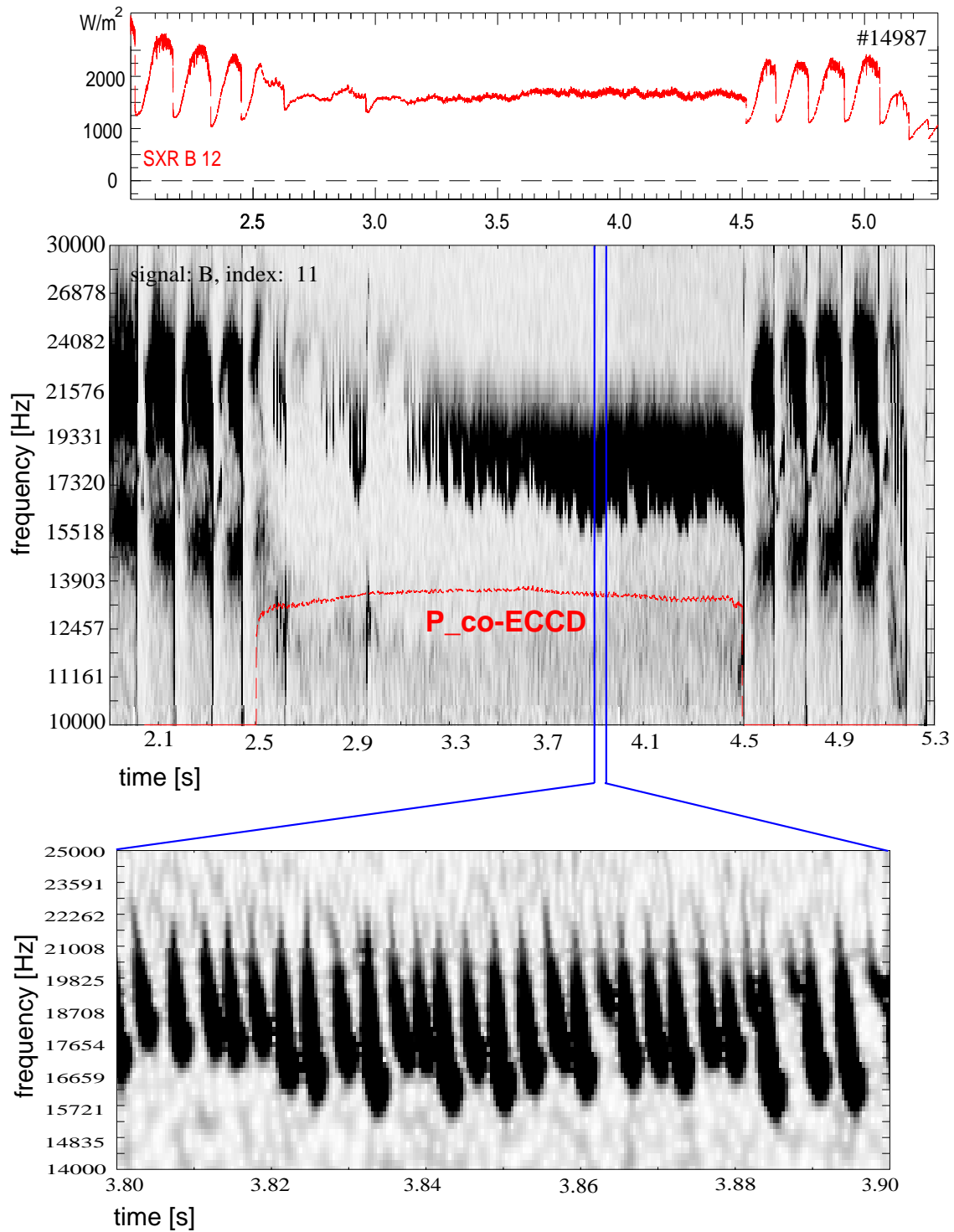


Figure 4.9: SXR time trace and wavelet plot, showing the frequency over time, of the constant  $B$  discharge with complete sawtooth stabilization and fishbone activity in sawtooth stabilization phase.

### 4.3 Influence of Counter-ECCD on Sawteeth

For counter-ECCD, the position of the ECR launching mirrors are changed to a toroidal launching angle of  $+15^\circ$ . The beam is now driving current in the opposite direction of the main plasma current. In figure 4.10, the maximum at  $\rho_{pol} \approx -0.42$  observed in the co-ECCD case is compensated. For central counter-ECCD deposition, a broad maximum is seen with a maximum sawtooth period of about 800 ms, further off-axis, the sawtooth period is comparable to the one without ECR. A change in the sawtooth behaviour between co- and counter-ECCD is clearly observed, while the deposited heating power is comparable for co- and counter-ECCD. This shows indirectly the presence of ECCD.

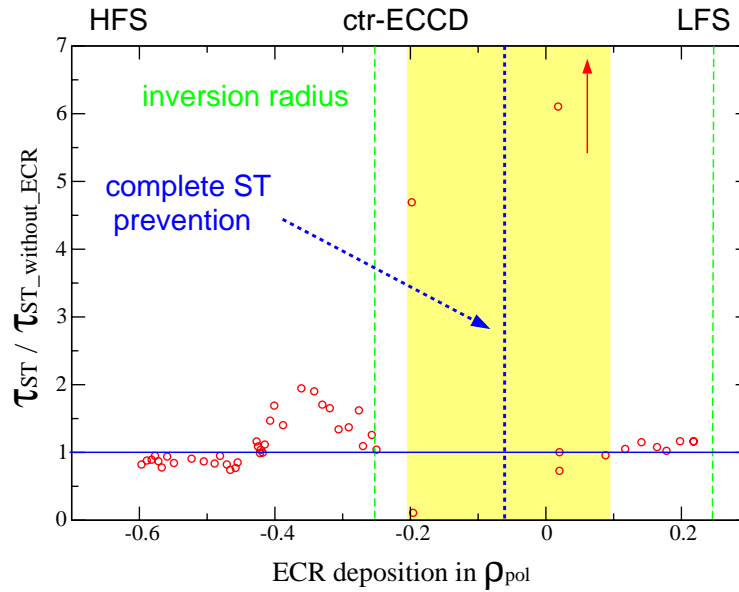


Figure 4.10: ECR deposition in  $\rho_{pol}$  over sawtooth period and sawtooth amplitude with counter-ECCD

Arguing as in the co-ECCD case, for deposition slightly outside the  $q = 1$  surface, the current gradient and with it  $q'$  is expected to increase. This has a destabilizing effect on the sawtooth period while for deposition inside the  $q = 1$  surface, the current gradient and with it  $q'$  is expected to decrease which leads to a stabilizing effect on the sawteeth. However, this simple stabilizing effect due to the change in the shear at  $q = 1$  cannot be applied here as it will be shown by discussing a gyrotron power ramp up.

To investigate the behaviour of the sawtooth period, amplitude and how much power is needed for stabilization, ECR power ramps are performed. Figure 4.11 shows discharge #15847 (NBI 3,7) with a ramp from zero to 0.8 MW ECR with deposition in the centre (at  $\rho_{pol} \approx -0.07$ ). The power threshold for complete stabilization is reached with nearly full power of both gyrotrons. With 0.7 MW heating power (same counter-ECCD scenario than before), the sawteeth could be completely stabilized. Figure 4.12 shows that the sawtooth period remains about constant, while the sawtooth amplitude constantly decreases. One would expect stabilization with

increasing sawtooth period. In discharges with constant field, complete sawtooth prevention is achieved. The even slightly decreasing sawtooth period and decreasing amplitude in figure 4.12 with increasing power is surprising. The effect here seems due to the slight decrease in the sawtooth period closer to destabilization than to stabilization, while the  $\rho_{pol}$  scan clearly shows a stabilizing region with a sawtooth period increase, proven by several constant field discharges with complete sawtooth prevention. It is a clear example, that the description of sawtooth behaviour by “stabilization” or “destabilization” is insufficient and has to be used carefully. During the stabilization phase, a (1,1) mode is present without fishbone activity.

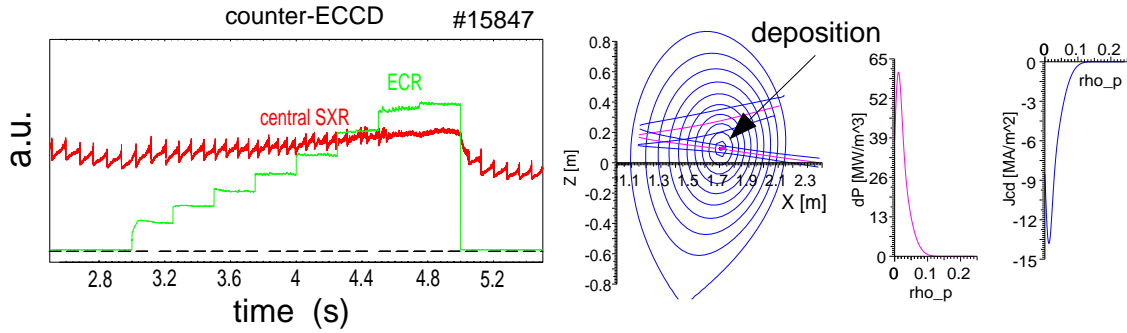


Figure 4.11: Sawtooth period changes due to a counter-ECCD power ramp up at  $\rho_{pol} \approx +0.01$ , NBI beams 3,7. The ECR deposition, the power deposition and current profile are shown.

In figure 4.11 the result of a TORBEAM simulation for the ECR deposition is seen. The deposition is on-axis, the power deposition and current profile are seen on the right hand side in figure 4.11. The deposition profile becomes narrower for central deposition than for off-axis deposition, as seen in figure 2.19.

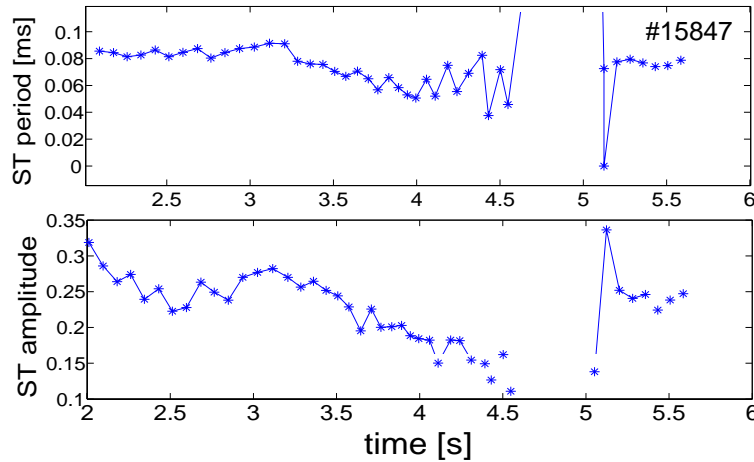


Figure 4.12: The sawtooth period slightly decreases and the amplitude decreases during counter-ECCD power ramp.

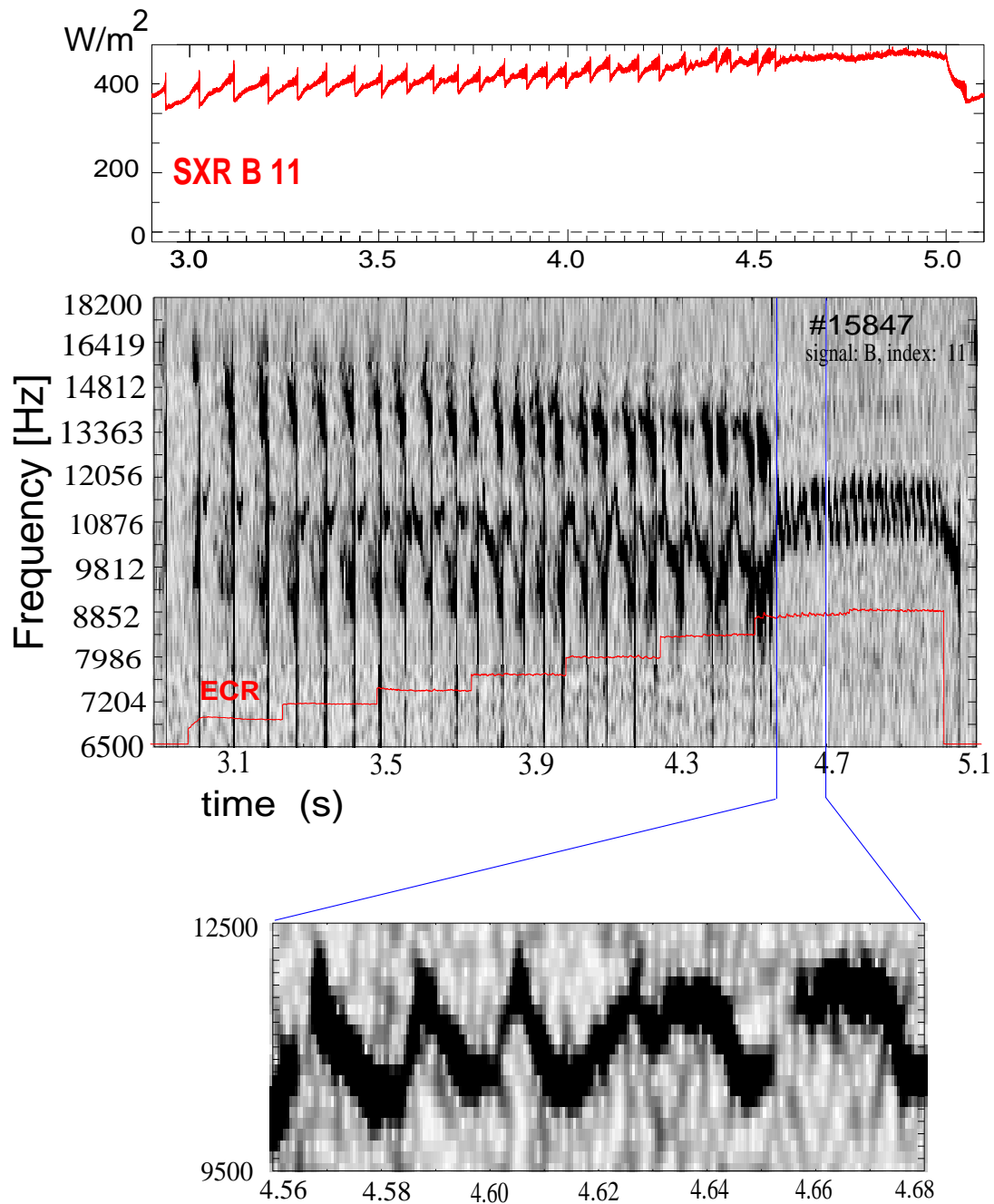


Figure 4.13: Sawtooth suppression with counter-ECCD power ramp up, using NBI sources 3 and 7. In the wavelet plot, it can be seen that the (1,1) mode becomes destabilized with increasing ECR power.

In the wavelet plot in figure 4.13, showing the time evolution of mode frequencies, it can be seen that a (1,1) mode with a frequency of about 10 kHz becomes destabilized, which develops from the sawtooth precursor, with increasing ECR power. However, the mode amplitude decreases with increasing ECR power.

The appearance of the stabilization phase in the counter-ECCD case changes with deposition location. The remaining (1,1) mode does not have fishbone activity but sometimes shows abrupt changes like jumps in the frequency like in figure 4.13 or shows no change in frequency at all. In average, the period of the jumps is about 40 ms, which is about half of the previous sawtooth period.

At the threshold where the sawteeth disappear, the mode is still present and strong enough to keep the SXR signal constant which means the transport is high enough that impurities do not accumulate in the plasma centre.

In chapter 6, the discharge #15847 the profiles will be investigated in more detail. Modelling of discharges with central counter-ECCD with the Porcelli model is not possible, because the Porcelli model is not valid for reversed shear profiles.

However, from this difference in MHD signature, one can conjecture that the stabilization mechanisms for off-axis co-ECCD and central counter-ECCD differ.

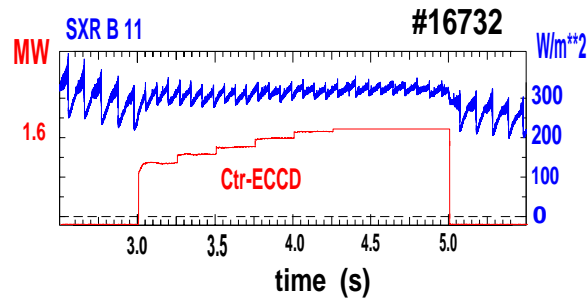


Figure 4.14: Gyrotron power ramp up with off-axis counter-ECCD deposition with NBI sources 3, 7. No big change in the sawtooth period seen, only amplitude decreases.

Analog to the co-ECCD case, a gyrotron power scan is performed with off-axis deposition. For deposition in the small minimum outside the sawtooth inversion radius, no big change in the sawtooth period is expected. However, maybe the counter current driven in the deposition scans is just sufficient to compensate the maximum in the sawtooth period seen in the co-ECCD case. The sawtooth period is even smaller in the case without current drive in the following figure 4.15. In this figure, the influence of heating only on the sawtooth period is investigated. In the experiments with co- and counter-ECCD, the deposited heating power is comparable. The main difference lies not in the deposited heating power but the local driven current. In figure 4.14, the sawtooth period could be further decreased as for central co-ECCD deposition. The magnetic field is kept constant with  $B = -2.23$  T in order to deposit the ECR in the minimum off-axis where the maximum is observed in the co-ECCD case. The ECR power is ramped up from approximately 1.0 MW to about 1.7 MW. The sawtooth period could be lowered from 110 ms without ECR to about 70 ms with ECR.

## 4.4 Influence of ECRH on Sawteeth

The discharges with ECRH are performed with one launching angle of  $+15^\circ$  and one with  $-15^\circ$ . This means one ECR beam is driving counter-ECCD, the second one co-ECCD. The net current is expected to add up to zero, while the deposition profile is comparable to the following co- and counter-ECCD experiments. A TORBEAM simulation showed for discharge #14883 with deposition at  $\rho_{pol} = 0.4$  at 3.0 s a net current of 0.2 kA. The total driven current by each gyrotron is 6.6 kA and 6.8 kA.

In figure 4.15, a maximum in sawtooth amplitude is seen at  $\rho_{pol} \approx -0.45$ . With a maximum sawtooth period of about 240 ms, the maximum is lower than with co-ECCD. For deposition further outside the plasma centre, the sawtooth amplitude is the same than without ECRH. Inside the sawtooth inversion radius, the period remains mostly below the level without ECR, similar to the co-ECCD case. It has to be kept in mind that a small net current in co direction is still driven, because the currents in co and counter direction add up to  $I_{ECR} = 0.2$  kA.

The ECRH case shows clearly that the change in the sawtooth period does not appear due to localized heating. The small but very localized driven current is responsible for the change in the sawtooth period.

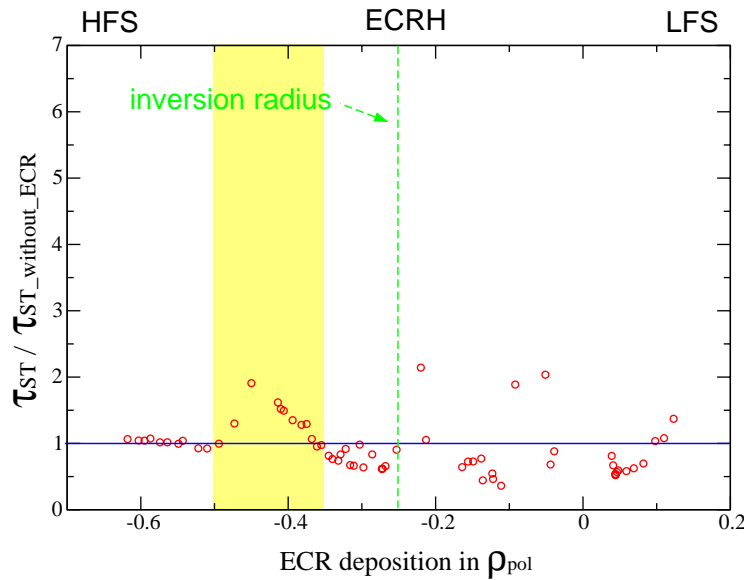


Figure 4.15: ECRH deposition in  $\rho_{pol}$  over sawtooth period and sawtooth amplitude

Close to  $\rho_{pol} \approx \pm 0.1$ , a second, very narrow peak in sawtooth period is observed. To make sure that this peak is not a side effect of the overlay of co- and counter-ECCD, a narrow region is scanned with pure heating. The raw SXR data is shown in figure 4.16. Heating directly inside the island might be responsible for this reproducible effect. With electron cyclotron emission data, mode analysis can be performed with higher spacial resolution than with the SXR diagnostic. The position of the (1,1) mode and with it the island is situated slightly further outside at about  $\rho_{pol} \approx 0.20$ . However, due to the finite width of the ECR power deposition

profile, it is possible that part of the power is deposited directly into the island.

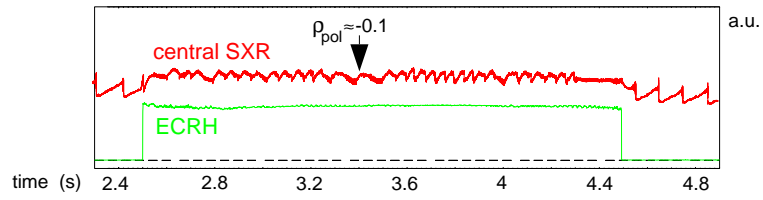


Figure 4.16: SXR time trace of  $B$  field scan with pure ECRH around  $\rho_{pol} \approx -0.1$

# Chapter 5

## NTM Control by sawtooth stabilization

In this chapter it will be investigated whether the control of sawteeth is able to prevent the triggering of NTMs and eventually lead to an increase in  $\beta$  as has been indicated in JET [26]. This investigation is based on the results of chapter 4, utilizing the knowledge gained from experiments with medium NBI power on how to influence sawteeth depending on the deposition and current drive direction.

In order to be able to trigger NTMs, the injected neutral beam power is increased, resulting in an increase of  $\beta$ . The influence of the different NBI sources on the sawtooth period has to be taken into account by comparing experimental results obtained with several beam sources. A mixing effect on the sawteeth due to the neutral beam heating and the ECR is expected.

In the following experiments, the NBI is used as the main heating source in Deuterium plasmas. The plasma current is chosen as  $I_p = 0.8$  MA and densities of about  $n_e = 6 \cdot 10^{19} \text{ m}^{-3}$ . As in the previous chapter, sawtooth stabilization is referred to as an increase of the sawtooth period, while during a complete stabilization phase no sawteeth appear at all. On the other hand, sawtooth destabilization means a shortening of the sawtooth period.

In the following, experiments are described using co-ECCD and counter-ECCD with central and off-axis deposition on the high field side.

### 5.1 Central ECR deposition

In discharges with medium NBI power [40], the sawtooth behaviour can be controlled as described in detail in chapter 4. If the ECR is deposited near the plasma centre, complete stabilization is achieved with counter-ECCD and strong destabilization with co-ECCD. However, the goal of the sawtooth investigation is the suppression of NTMs by controlling the sawtooth activity. In the discharges #16841,2,3 in figure 5.1, the NBI power is increased up to 12.5 MW in order to trigger NTMs.

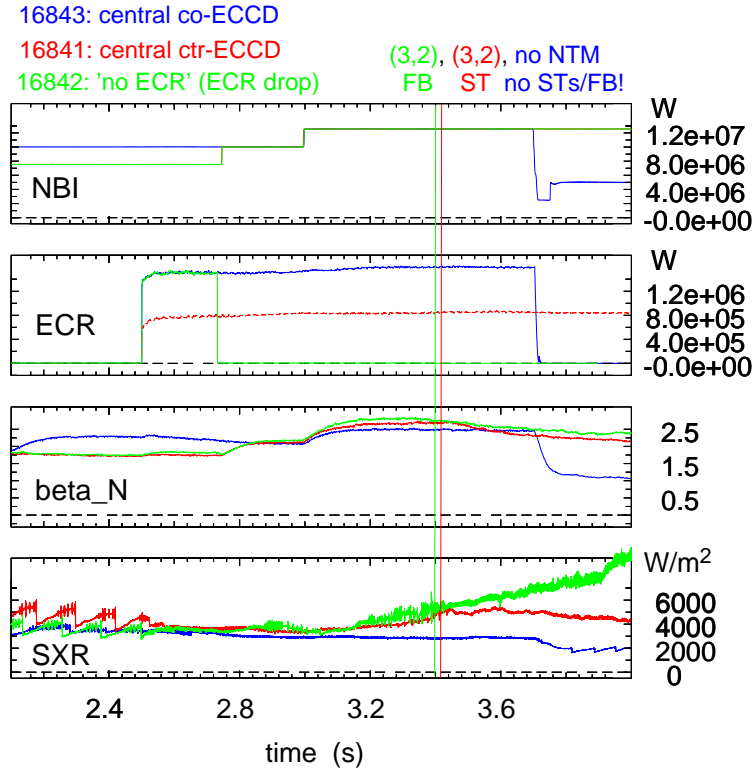


Figure 5.1: Co-, counter- and no ECCD as reference for central deposition ( $\rho_{pol} \approx 0.11$ ) with 12.5 NBI power. For counter-ECCD and without any ECR, NTMs are triggered. In the co-ECCD case, no NTM is triggered due to too low  $\beta$ .

In the reference discharge #16842, except for a short ECR phase, **no ECR** is present. In this discharge, the sawteeth seem to vanish and fishbone activity is present due to the increase of the neutral beam power, or the combination of beam sources with deposition on- and off-axis. The influence of the NI injection geometry is described in section 4.1. NBI source 5 is added shortly after the ECR pulse, in addition with the already used beam sources 3, 7 (off-axis beam source) and 8. This combination seems to be responsible for the sawteeth not returning. Strong fishbone activity with mode amplitudes of 3.5% is present and finally triggers an NTM with high  $\beta_N = 2.8$ , indicated with a solid line in figure 5.1. The mode amplitude is an indication for the size of the seed island. The higher the absolute amplitude (see E) the larger the seed island.

In the discharge with **co-ECCD** deposition (#16843), the sawteeth disappear for central deposition of co-ECCD. The already long sawteeth with low amplitude completely vanish immediately with the ECR onset and do not reappear. In comparison with the lower power pulse experiments in chapter 4, sawtooth destabilization, which means higher frequent sawteeth, is observed with central co-ECCD deposition. However, neither sawtooth nor fishbone activity can be seen in discharge #16843. Only a weak (1,1) mode with a mode amplitude of 1.1% is still present which is strong enough to keep the SXR signal at the same level, which means that the impurity content is low in the centre. No NTM is triggered in this discharge, even though the total heating power is high with  $P_{NBI} = 12.5$  MW.  $\beta$  remains relatively low throughout the

discharge, with  $\beta_{N,max} \approx 2.5$ . This value, rather than the absence of the sawteeth might be responsible for no NTM being triggered. Later in this section, experiments are presented with poloidal beta feedback control to achieve a constant high beta by variation of the NBI power. In the sawtooth control experiments, the sawteeth show a strong increase in their period with central **counter-ECCD**. The discharge #16841 is performed with two gyrotrons and central counter-ECCD deposition, meaning the same power as the sawtooth control experiments in chapter 4 and half the power of the two already described discharges #16843 and #16842. Only fishbone activity is present with a (1,1) mode amplitude of 2.3%, slightly increased compared with the co-ECCD case, until two small events, combining fishbones with sawteeth. A (3,2) NTM is triggered by the first stronger sawtooth at relatively high  $\beta_N = 2.7$ . The vanishing of the sawteeth might be expected, however, it is more likely that the influence of the neutral beam injection is responsible for the suppression of the sawteeth as in the two previously described discharges.

Summarizing the described set of discharges, the sawtooth behaviour seen in the sawtooth control experiments with central ECR deposition cannot be observed with high NBI power. The effect of the NBI injection geometry obviously strongly overlays the ECR effect. In the discharge #16843 in figure 5.1,  $\beta$  seemed to be too low to trigger an NTM. One option to increase the  $\beta$  is to increase the total heating power. In figure 5.2 three discharges are shown with central co- and counter deposition and one without ECR as a reference discharge.

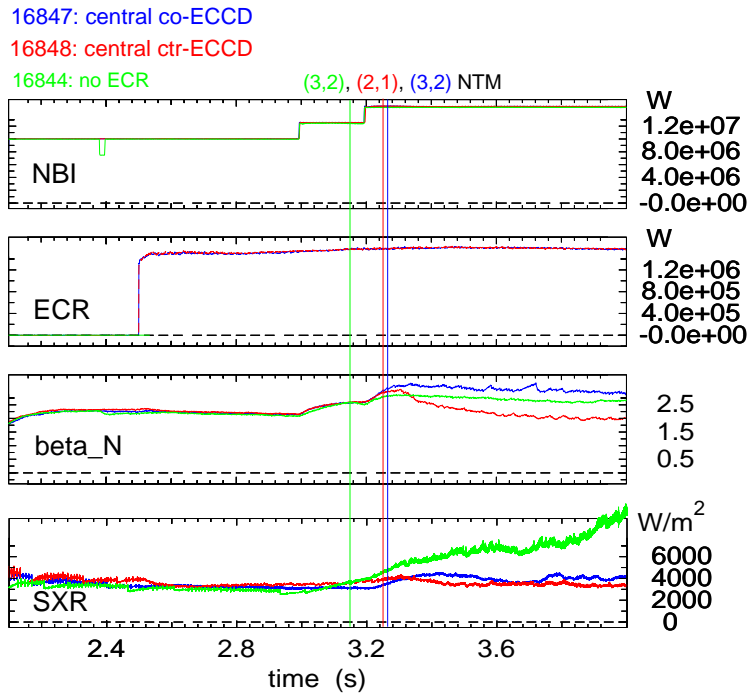


Figure 5.2: Co-, counter- and no ECCD for central deposition ( $\rho_{pol} \approx 0.11$ ) with 15 NBI power. Immediate NTM triggering observed after the last step in NBI power from 12.5 MW to 15 MW.

The  $\beta_N$  in discharge #16847 with **co-ECCD** deposition is increased as intended. The sawteeth

still vanish with the onset of the ECR, driving a current of  $I_{ECR} \approx 67$  kA, calculated with TORBEAM. However, the destabilization seen in the sawtooth control experiments in chapter 4 cannot be observed. A (3,2) NTM is triggered by a fishbone about 100 ms after the last step in the NBI power from 12.5 MW to 15 MW. A far stronger confinement decrease than observed in all previously discussed high power discharges is seen at the NTM onset with **counter-ECCD**, triggered by the first sawtooth after the ECR onset. The high beta loss from  $\beta \approx 3.0$  to  $\beta \approx 2.0$  due to the NTM can be explained by the triggering of a (2,1) NTM. It is well known that a (2,1) NTM leads to a higher  $\beta$  loss than a (3,2) NTM [37].

In the reference pulse **without ECR**, the sawtooth period is very long. The longest sawtooth free phase lasts about 320 ms. A (3,2) NTM is triggered even before the maximum in heating power is reached by the second sawtooth after the long sawtooth free phase.

As a summary, the maximum ECR power currently available in ASDEX Upgrade might not be sufficient to take enough influence on NTMs with a neutral beam power of  $P_{NBI} = 15$  MW together with the not fully known influence of the combination of different NBI sources on the sawteeth. Continuation experiments are performed with a neutral beam heating power of  $P_{NBI} = 12.5$  MW.

## 5.2 Off-axis ECR deposition

In the sawtooth control experiments in chapter 4, sawtooth stabilization is observed for co-ECCD deposition at  $\rho_{pol} \approx 0.4$  while for counter-ECCD a small destabilizing effect or no big effect at all is eventually seen. One has to keep in mind, that the Shafranov shift, explained in section 2.1.1, will influence the ECR deposition more strongly than in the sawtooth control experiments due to the higher neutral beam power. As with the first described on-axis experiments, the neutral beam heating is ramped up to a maximum of  $P_{NBI} = 12.5$  MW, seen in figure 5.3.

With the initial level of  $P_{NBI} = 10$  MW in the reference discharge **without ECR**, suppression of the sawteeth and a constant fishbone activity with a mode amplitude of 2.6% is observed. By increasing the NBI power up to  $P_{NBI} = 12.5$  MW, the fishbones become less frequent and show an increased mode amplitude up to about 5.8%, finally triggering a (3,2) NTM with  $\beta_N \approx 3.0$  and a lower absolute amplitude (which means a smaller seed island) of about 3.3%. By adding local **co-ECCD** in the initial  $P_{NBI} = 10$  MW phase, the sawteeth remain absent while the mode amplitude of the fishbones strongly decreases from 3.9% to 0.68% after the ECR onset. Obviously, the ECR has a stabilizing effect on the fishbone mode. During this time, the deposition of the ECR is shifted outwards from  $\rho_{pol} \approx 0.2$  before the ECR to  $\rho_{pol} \approx 0.3$ . By ramping the NBI up to  $P_{NBI} = 12.5$  MW, again, a long sawtooth free phase of 360 ms is observed until the sawteeth reappear. A (3,2) NTM is triggered by a sawtooth while the ECR deposition is shifted further out to  $\rho_{pol} \approx 0.44$  due to the Shafranov shift. In the sawtooth stabilization experiments, the deposition scan with co-ECCD in figure 4.4 in the previous chapter 4 shows that the off-axis maximum in the sawtooth period is found not to be relatively narrow. A possible explanation is that in discharge #16862, the deposition location might be moved out of the sawtooth stabilization regime, leading to a reappearance

of the sawteeth. After the reappearance of the sawteeth, the sawtooth period first becomes longer and finally becomes shorter again (compare with figure 5.4) until the mode is triggered by a sawtooth with a relatively short period of about 30 ms with a  $\beta_N \approx 3.1$ . Due to [26], long sawtooth periods lead to a triggering of an NTM at lower  $\beta$  than high frequent sawteeth. A longer sawtooth period might allow the shear to become larger at the sawtooth crash. It is usually expected that the NTM is triggered by a big seed island, delivered by the first sawtooth then having a very big period. However, in this discharge, the NTM onset is delayed for several sawtooth crashes, until not even the sawtooth with the longest period triggers an NTM. This seems to be a contradiction to the result in [26].

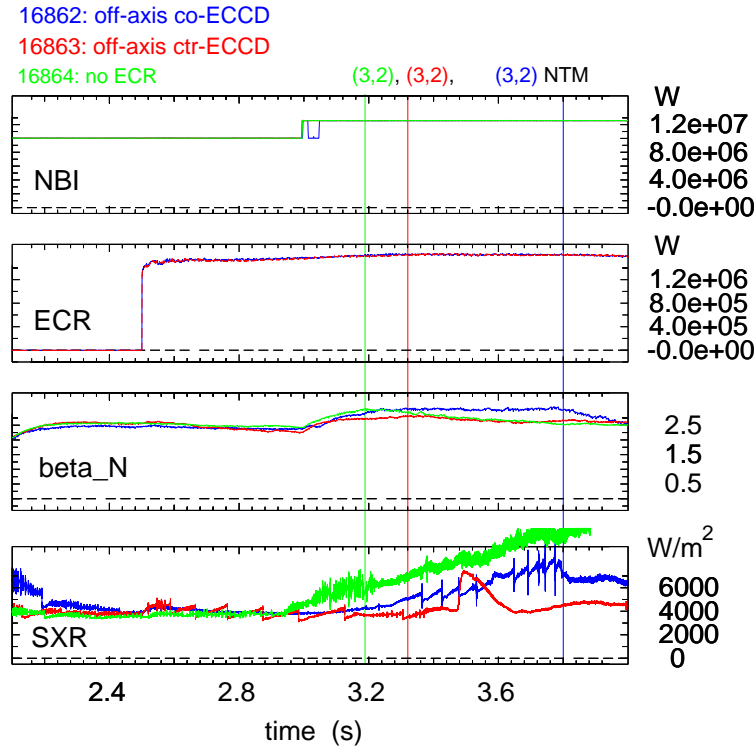


Figure 5.3: Co-, counter- and no ECCD for off-axis deposition ( $\rho_{pol} \approx 0.4$ ) with 12.5 NBI power. Long sawtooth free period seen for co current drive.

With additional off-axis **counter-ECCD** deposition, the sawteeth reappear with the ECR onset. After increasing the power from the initial  $P_{NBI} = 10$  MW to the final  $P_{NBI} = 12.5$  MW, beta remains with a maximum of  $\beta_N = 2.8$  below the values of the no ECR and the co-ECCD cases. A (4,3) NTM is triggered early, far before the triggering of the (3,2) NTM, which might be responsible for the reduced  $\beta$ . However, a (4,3) NTM usually does not lead to such a big decrease of the plasma  $\beta$  as the (3,2) NTM [37].

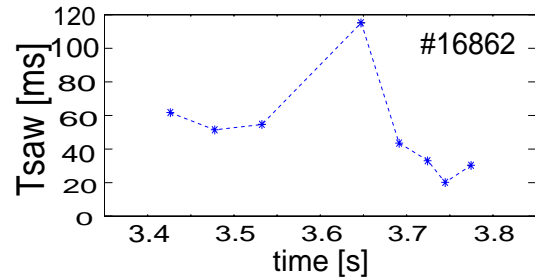


Figure 5.4: Sawtooth period in [ms] for the reappearing sawteeth in #16862.

### 5.3 Beta feedback control

The most promising of all discharges presented so far in this chapter, is the one with off-axis co-ECCD deposition #16862, seen in figure 5.3, having a long sawtooth free phase. However, as explained in the previous section, due to the Shafranov shift, the deposition of the ECR might be shifted out of the stabilization region.

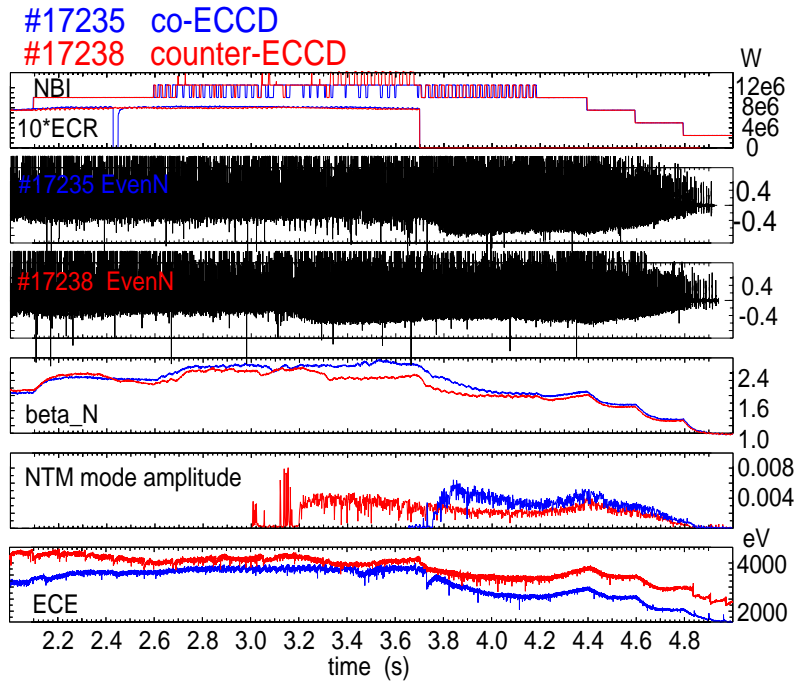


Figure 5.5: Co- and counter-ECCD with four gyrotrons. Prevention of the (3,2) NTM achieved for a complete co-ECCD pulse.

The discharge #17235 in figure 5.5 is designed to stay in this sawtooth free regime. A slight toroidal field ramp from  $B_T = -2.26 \dots -2.32$  T is performed to compensate the Shafranov shift, responsible for changing the ECR deposition location. The measured magnetic field ramp can be seen in figure 5.6. In order to receive a high enough and constant  $\beta$ , poloidal  $\beta$  feedback control is applied in #17235 and identical in the reference discharge #17238.

In ASDEX Upgrade, control of the poloidal beta  $\beta_{pol}$  is possible via adaptation of the neutral beam heating. By real time control of the neutral beam power, with  $\beta_{pol}$  as can be seen in figure 5.6,  $\beta_N$  can be adjusted as well.

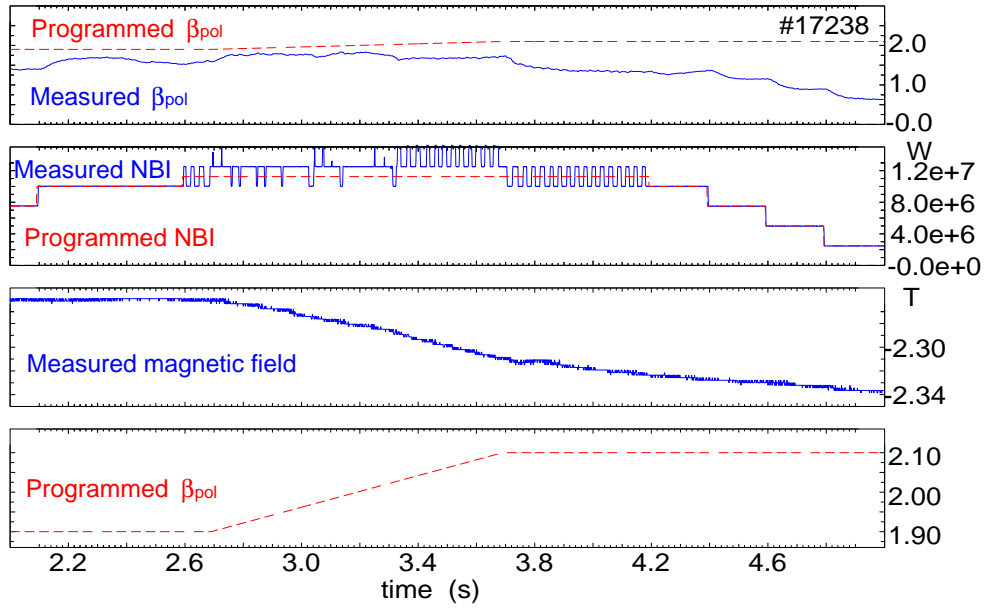


Figure 5.6: Ramp in  $\beta_{pol}$  compared with the measured value, NBI programmed and measured value with  $\beta_{pol}$  feedback control and magnetic field ramp

However, in order to achieve a constant  $\beta_N$ , defined in equation 1.13, the magnetic field dependence has to be taken into account. To compensate the change in  $\beta_N$  due to the field ramp, a small ramp in  $\beta_{pol}$  is added to compensate the field ramp and to keep  $\beta_N$  constant with  $\beta_N \approx 2.8$ . The ramp in  $\beta_{pol}$  programmed for the discharge #17235 can be seen in figure 5.6 in comparison with the actual value and enlarged for more detail.

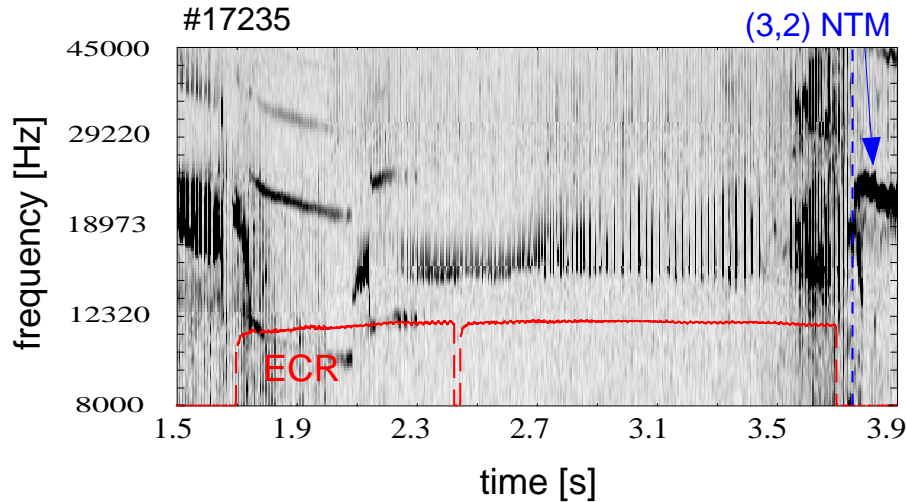


Figure 5.7: Wavelet plot of #17235 without NTM during ECR pulse. The (3,2) NTM is triggered by a sawtooth after the ECR pulse.

In discharge #17235 in figure 5.5,  $\beta_N$  is successfully kept constant with the desired value of  $\beta_N \approx 2.8$ . No big sawtooth crashes appear throughout the complete ECR phase except some small events in the second half of the ECR pulse. These events are mixtures of fishbones and sawteeth. A very small sawtooth amplitude and a small but detectable inversion of the sawtooth at the inversion radius can be seen in the ECE data. However, these 'sawteeth' are such a small perturbation in the plasma, that the seed island must be very small. Relevant fishbone activity is present throughout the ECR pulse, as can be seen in the wavelet plot in figure 5.7. The (1,1) mode amplitude of the fishbones is with approximately 2.3% the same before the ECR onset as during the ECR pulse. But the position of the mode moves outwards from  $\rho_{pol} \approx 0.28$  to 0.35 with the switch-on of the ECR. Smaller mode amplitude would deliver smaller seed islands. The smaller the seed island, the less likely an NTM triggering. However, due to the same mode amplitude, the size of the seed island cannot be the deciding effect. The movement of the (1,1) mode to further outside the plasma centre indicates a flattening of the  $q$ -profile, which has a stabilizing effect on sawteeth. Even an impurity event at about 3.5 s does not lead to an NTM triggering. Finally, just after the ECR power is switched off, a (3,2) NTM appears, triggered by a sawtooth. The onset of the NTM can be seen in figure 5.5 the Mirnov signal "EvenN", showing the presence of modes with even mode numbers. The time traces of the (3,2) mode amplitude can be seen as well in figure 5.5, showing the far earlier onset on the (3,2) NTM onset in the counter-ECCD case.

Discharge #17238 in figure 5.5 serves as a reference discharge. To keep all profiles comparable to the co-ECCD case, the ECR is not switched-off, but counter-ECCD is applied. An early (4,3) NTM is triggered, however, not having much influence on  $\beta$ . Sawteeth are present throughout the complete ECR pulse until a (3,2) NTM is triggered early by a fishbone. The counter-ECCD deposition shows a small influence on the (1,1) mode amplitude. The mode amplitude slightly decreases from 2.7% before the ECR onset to about 1.3% after the ECR onset. The fishbone triggering the (3,2) NTM has a similar mode amplitude to the previous ones, therefore indicating that the seed island size cannot be the deciding criterion. The position of the (1,1) mode of the fishbones is not as distant from the plasma centre with  $\rho_{pol} \approx 0.25$  as for the fishbones observed with co-ECCD deposition. However, the (1,1) mode of the fishbone, triggering the (3,2) NTM, is shifted slightly further outside to  $\rho_{pol} \approx 0.3$ . The complete discharge must be in an unstable NTM regime, so that any fishbone can trigger the NTM.

The same discharge is repeated with half of the ECR power  $P_{ECR} = 0.8$  MW, see figure 5.8. Even in the co-ECCD case a (3,2) NTM is triggered by a fishbone during the ECR pulse. In #17142 the mode is not situated as far outside as in #17235 which indicates that the change in the current profile is weaker. However, a change in the current profile will influence more the sawtooth behaviour than the NTM onset. A possible explanation could be that other parameters like the pressure scale length at the  $q = 3/2$ , or the position of the (3,2) mode, are changed due to the off-axis ECR deposition. The power of two gyrotrons is not sufficient to prevent the NTM.

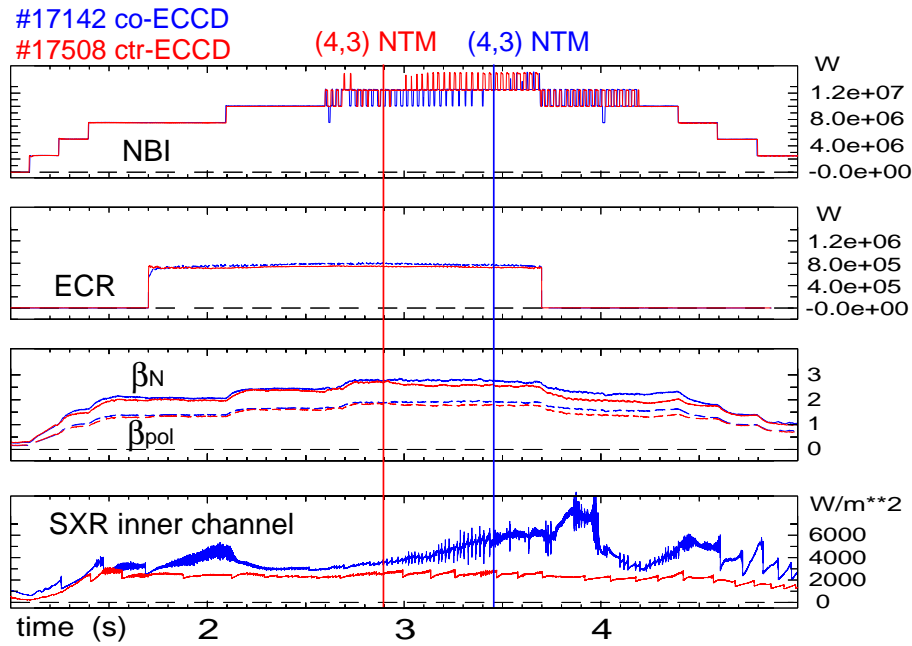


Figure 5.8: Off-axis ECR deposition for co-and counter-ECCD with two gyrotrons. The NTM could not be prevented with four gyrotrons as shown.

In summary, NTM prevention was demonstrated with  $P_{ECR} = 1.6$  MW off-axis co-ECCD, using  $\beta_{pol}$  feed back control and a magnetic field ramp to adapt the ECR deposition. Further experiments on the NTM prevention with off-axis co-ECCD deposition will show the degree of reproducibility and value of this scenario.



# Chapter 6

## Interpretation with ASTRA

### 6.1 ASTRA Transport Code

The ASTRA Automatic System for TRansport Analysis code [29] is a transport code used for wide applications. It can be used in different ways e.g. predictive or interpretative. In this chapter, a discharge with complete sawtooth stabilization due to off-axis co-ECCD deposition is investigated. In this work, the Porcelli model with its sawtooth triggering conditions was implemented to the ASTRA code. Experimental data is processed and unknown parameters supplemented by ASTRA. Due to this combination, an interpretative analysis is performed, explaining the disappearance and reappearance of sawteeth.

#### 6.1.1 Definition of Variables

In ASTRA, toroidal symmetry is assumed, using two co-ordinate systems to describe it. In the cylindrical co-ordinate system  $\{r, \varphi, z\}$ , the polar axis describes the major torus axis, while in the second co-ordinate system  $\{a, \Theta, \zeta\}$  is defined via the magnetic geometry.  $a$  stands for an arbitrary label of a flux surface,  $\Theta$  the poloidal angle and the toroidal angle  $\zeta = -\varphi$  and  $R_0$  the geometric axis of the vacuum vessel. The basic transport equations in the ASTRA transport code for the electron density  $n_e$ , the electron temperature  $T_e$ , the ion temperature  $T_i$  and the poloidal flux  $\Psi$  are defined using the flux co-ordinate

$$\rho = \sqrt{\frac{\Phi}{\pi B_0 a^2}} \quad (6.1)$$

with the toroidal magnetic flux  $\Phi$ .  $\rho$  represents the minor radius with the dimension of length. The volume  $V$  of a flux surface with  $a = \text{const.}$  is defined via a volume integral over the interior  $V$  of this flux surface with its derivative  $V' = \frac{\partial V}{\partial \rho}$ . The magnetic field  $\mathbf{B}$  and the current density  $\mathbf{j}$  are defined using the Maxwell equations:

$$\mathbf{B} = I\nabla\zeta + \frac{1}{2\pi} [\nabla\Psi \times \zeta] \quad (6.2)$$

$$\mathbf{j} = -\frac{\nabla\zeta}{2\pi\mu_0} r^2 \nabla \cdot \frac{\nabla\Psi}{r^2} + \frac{1}{\mu_0} [\nabla I \times \nabla\zeta] \quad (6.3)$$

Taking toroidal symmetry into account, the scalar functions  $\psi(a)$  and  $I(a)$  are found by multiplying the previous two equations with  $\nabla\theta$  together with an integration over the volume  $V$ . A dimensionless quantity  $J$  can be introduced that is very close to unity inside and exactly unity outside the plasma if the poloidal plasma current is far below the current flowing in the toroidal field coils, which is a good assumption for  $\beta \ll 1$ :

$$J = \frac{I}{R_0 B_0} \quad (6.4)$$

The poloidal and toroidal components of the magnetic field become

$$B_{pol} = \frac{|\nabla\rho|}{2\pi r} \frac{\partial\psi}{\partial\rho} \quad \text{and} \quad B_{tor} = \frac{I}{r} \quad (6.5)$$

In the following transport equations, an average cylinder-like poloidal field  $B_p$  is used with

$$B_p = \frac{1}{2\pi R_0} \frac{\partial\psi}{\partial\rho} \quad (6.6)$$

The transport equations on which the ASTRA code is based on can be written as

$$\frac{1}{V'} \left( \frac{\partial}{\partial t} - \frac{\dot{B}_0}{2B_0} \frac{\partial}{\partial\rho} \right) (V' n_e) + \frac{1}{V'} \frac{\partial}{\partial\rho} \Gamma_e = S_e \quad (6.7)$$

$$\frac{3}{2} (V')^{-5/3} \left( \frac{\partial}{\partial t} - \frac{\dot{B}_0}{2B_0} \frac{\partial}{\partial\rho} \right) \left[ (V')^{5/3} n_e T_e \right] + \frac{1}{V'} \frac{\partial}{\partial\rho} \left( q_e + \frac{5}{2} T_e \Gamma_e \right) = P_e \quad (6.8)$$

$$\frac{3}{2} (V')^{-5/3} \left( \frac{\partial}{\partial t} - \frac{\dot{B}_0}{2B_0} \frac{\partial}{\partial\rho} \right) \left[ (V')^{5/3} n_i T_i \right] + \frac{1}{V'} \frac{\partial}{\partial\rho} \left( q_i + \frac{5}{2} T_i \Gamma_i \right) = P_i \quad (6.9)$$

$$\sigma_{\parallel} \left( \frac{\partial\Psi}{\partial t} - \frac{\rho\dot{B}_0}{2B_0} \frac{\partial\Psi}{\partial\rho} \right) = \frac{J^2 R_0}{\mu_0 \rho} \frac{\partial}{\partial\rho} \left( \frac{G_2}{J} \frac{\partial\Psi}{\partial\rho} \right) - \frac{V'}{2\pi\rho} (j_{BS} + j_{CD}) \quad (6.10)$$

with the ion density  $n_i = n_e/Z_i$  and its flux  $\Gamma_i = \Gamma_e/Z_i$ , neglecting the influence of impurities and the electron and ion heat fluxes  $q_e$  and  $q_i$ .  $\sigma_{\parallel}$  is the electrical conductivity,  $j_{BS}$  describes the bootstrap current

$$j_{BS} = \frac{1}{B_0} \langle \mathbf{j}_{BS} \cdot \mathbf{B} \rangle \quad (6.11)$$

and  $j_{CD}$  the driven current

$$j_{CD} = \frac{1}{B_0} \langle \mathbf{j}_{CD} \cdot \mathbf{B} \rangle \quad (6.12)$$

The total current in the longitudinal Ohm's law adds up to

$$j_{\parallel} = \sigma_{\parallel} E_{\parallel} + j_{BS} + j_{CD} \quad (6.13)$$

In ASTRA, the transport equations are represented by the following matrix:

$$\begin{pmatrix} \frac{\Gamma_e}{n_e} \\ \frac{q_e}{n_e T_e} \\ \frac{q_i}{n_i T_i} \\ V' G_1 \frac{\mu_0 j_{BS}}{B_p} \end{pmatrix} = -V' G_1 \begin{pmatrix} D_n & D_e & D_i & D_E \\ \chi_n^e & \chi_e & \chi_i^e & \chi_E^e \\ \chi_n^i & \chi_e^i & \chi_i & \chi_E^i \\ C_n & C_e & C_i & 0 \end{pmatrix} \cdot \begin{pmatrix} \frac{1}{n_e} \frac{\partial n_e}{\partial \rho} \\ \frac{1}{T_e} \frac{\partial T_e}{\partial \rho} \\ \frac{1}{T_i} \frac{\partial T_i}{\partial \rho} \\ \frac{E_{\parallel}}{B_p} \end{pmatrix} \quad (6.14)$$

The coefficients  $C_n, C_e, C_i, D_E, \chi_E^e$  and  $\chi_E^i$  are dimensionless while the other coefficients have the dimension  $[m^2/s]$ .

With  $N$  describing the density of the neutral atoms,  $s_{rec}$  the recombination rate and the rates of impact ionization by electrons  $s_{ion}^{(e)}$  and ions  $s_{ion}^{(i)}$ , the source of electrons  $S_e$  is defined as

$$S_e = s_{ion}^{(e)} N n_e + s_{ion}^{(i)} N n_i - s_{rec} n_i n_e \quad (6.15)$$

and the electron energy source  $P_e$  and the ion energy source  $P_i$

$$P_e = P_{OH} - P_{\Gamma} - P_{ei} - P_e^{RAD} - P_e^N + P_e^H + P^{FUS} \quad (6.16)$$

$$P_i = P_{\Gamma} + P_{ei} + P_i^N + P_i^H \quad (6.17)$$

$P_e$  consists of the Ohmic heating power  $P_{OH}$  due to the toroidal main plasma current density  $j_{tor}$  and the flux surface quantity  $U_{pl} = \frac{\partial \psi}{\partial r} |_{\rho}$

$$P_{OH} = \frac{1}{2\pi R_0} U_{pl} j_{tor} \quad (6.18)$$

$P_e^{RAD}$  are the power losses due to radiation, the exchange of heat between electron and ion components  $P_{\Gamma} = \langle (\nabla \rho)^2 \rangle \frac{\Gamma_e}{n_e} \frac{\partial (n_i T_i)}{\partial \rho}$  and  $P_{ei} = \frac{3m_e n_e}{m_i \tau_e} (T_e - T_i)$  with the electron-ion collision time  $\tau_{ei}$ , while  $P_e^H$  and  $P_i^H$  are the auxiliary electron and ion heating powers. The losses occurring due to atomic processes are

$$P_e^N = \left( s_{ion}^{(e)} N E_{ion} + s_{rad} N E_1 + \frac{3}{2} s_{rec} n_i T_e \right) n_e \quad (6.19)$$

$$P_i^N = \frac{3}{2} (s_{ion} N T_N + s_{cx} N (T_N - T_i) - s_{rec} n_e T_i) n_i \quad (6.20)$$

with the temperature of the neutral atoms  $T_N$  and  $s_{cx}, s_{rad}$  the charge exchange and radiation rates with the energies  $E_{ion} = 13.6$  eV and  $E_1 = 10.2$  eV.  $P^{FUS}$  is the energy created due to fusion processes.

In the equations 6.7 and 6.14, the surface functions  $G_1 = \langle (\nabla \rho)^2 \rangle$ ,  $G_2 = \frac{V'}{4\pi^2} \langle \left(\frac{\nabla \rho}{r}\right)^2 \rangle$  and  $G_3 = \langle \frac{R_0^2}{r^2} \rangle = \frac{4\pi^2 \rho R_0}{J V'}$  are used. For more details see [29].

In ASTRA, usually the rotational transform  $\mu$  instead of the safety factor  $q$  is used

$$\mu = \frac{1}{q} = \frac{\partial \psi}{\partial \Phi} = \frac{1}{2\pi B_0 \rho} \frac{\partial \psi}{\partial \rho} = \frac{B_p R_0}{B_0 \rho} \quad (6.21)$$

The plasma equilibrium is calculated as described in chapter 2.1.1 via the Grad-Shafranov equation 2.17.

## 6.2 Modelling of Sawtooth Stabilization with the Porcelli Model

In ASTRA, subroutines can be implemented, allowing the investigation of different areas. The three sawtooth criteria introduced in the equations 2.65 - 2.68 were added to ASTRA via a subroutine. In the following simulation, the discharge #14987 is modelled. In this discharge, a co-ECCD pulse from 2.5 s - 4.5 s completely stabilizes the sawteeth. After the switch off of the ECR, the sawteeth reappear. A central SXR timetrace and a wavelet plot of this discharge can be seen in figure 4.9.

In the modelling, data for the electron temperature  $T_e$ , the ion temperature  $T_i$  and the electron density  $n_e$  are taken from experimental observation. The electron temperature used in the simulations is measured by the electron cyclotron emission (ECE) diagnostic, the ion temperature by charge exchange measurement (CXRS) and the electron density by central Thomson scattering measurements. As maximum, one hundred data points are taken for the time from 2 s - 5 s, less if the resolution of the diagnostic is less for this discharge. All profiles are revised manually and unrealistic data points sorted out. A very strong smoothing factor applied for example to the density profile muddles out the steep gradient at the plasma edge leading to a change in the whole  $q$ -profile. If no smoothing is done, the local density gradient at  $q = 1$  would become less accurate. However, it has to be stressed that using experimental data for this sawtooth model can only give indications as a result. It has to be kept in mind, that errors for example in the derivative of the calculated  $q$ -profile without MSE, of the calculated pressure profile and of the measured density profile are made. A detailed modelling of every appearing sawtooth is not expected. The measured data together with the equilibrium reconstruction leading to a  $q$ -profile are not accurate enough. However, it is expected to find at least a general development of the parameters describing sawtooth stability with the ECR.

The result of the first of Porcelli's sawtooth triggering criteria, defined by the inequality  $-\delta\hat{W}_{core} > c_h\omega_{Dh}\tau_A$  is seen in figure 6.1. If a sawtooth is triggered by the destabilization of the ideal internal kink mode, the left side of the equation has to exceed the right side. If the red curve in figure 6.1 tops the blue curve, sawtooth triggering is expected.

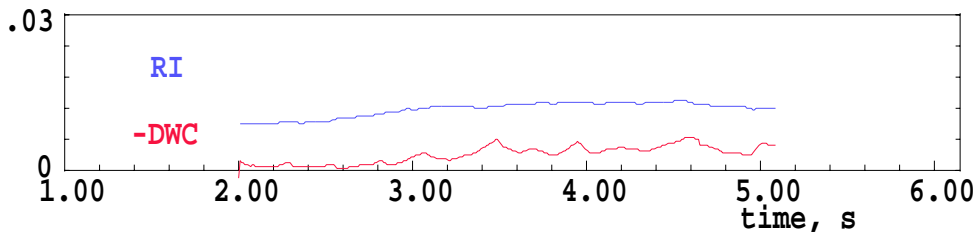


Figure 6.1: The first criterion for the onset of the ideal kink mode leading to sawtooth triggering, defined by the inequality  $-\delta\hat{W}_{core} > c_h\omega_{Dh}\tau_A$  with  $-\delta\hat{W}_{core}$  and  $c_h\omega_{Dh}\tau_A$ , is not valid.

The right side of the inequality of criteria one is dependent on a factor  $c_h$  in the order of unity. Here, this free parameter is chosen as  $c_h = 0.4$ , as used by Porcelli in [13]. Throughout the

whole discharge, the blue curve lays well over the red curve, indicating that the ideal kink mode is not responsible for the observed sawtooth stabilization.

In figure 6.2 it can be seen, that criterion two  $-\delta\hat{W} > 0.5\omega_{*i}\tau_A$  is also not fulfilled. The red curve in figure 6.2 shows the total energy functional  $-\delta\hat{W}$  and the green curve the right side of the inequality  $0.5\omega_{*i}\tau_A$ . The green curve is throughout the whole discharge above the red curve, which indicates that the second criterion is not valid. However, the higher values of the green curve than the red one fulfill the first part of the third criterion. The inequality  $-c_p\hat{\rho} < -\delta\hat{W} < 0.5\omega_{*i}\tau_A$  has to be valid so that the critical shear criterion  $s_1 > s_{crit}$  for the sawtooth onset becomes relevant.

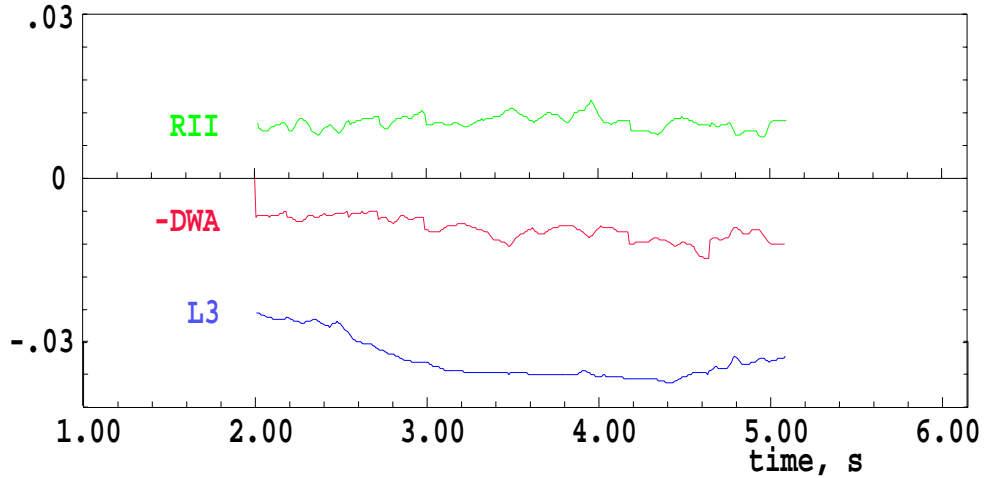


Figure 6.2: Second criterion  $-\delta\hat{W} > 0.5\omega_{*i}\tau_A$  is not fulfilled. Inequality  $-c_p\hat{\rho} < -\delta\hat{W} < 0.5\omega_{*i}\tau_A$  which has to be fulfilled if critical shear criterion is relevant with  $R11 = 0.5\omega_{*i}\tau_A$ ,  $-DWA = -\delta\hat{W}$  and  $L3 = -c_p\hat{\rho}$  is valid.

The very left side of the inequality  $L3 = -c_p\hat{\rho}$  is proportional to the free parameter  $c_p$  in the order of unity. In figure 6.2 this parameter is chosen to  $c_p = 1$  as in [13].

Due to the validity of the last inequality 2.68, the behaviour of the critical shear at the  $q = 1$  surface  $s_{crit} = \alpha(S^{1/3}\hat{\rho})^{1/2}(\beta_{i1}R^2/\bar{r}_1^2)^{7/12}(\bar{r}_1/r_n)(\bar{r}_1/r_p)^{1/6}$  compared with the real shear at the  $q = 1$  surface  $s_1$  has to be investigated. In figure 6.4, a comparison of the shear  $shea$  at  $q = 1$  and the critical shear  $SCRI$  at  $q = 1$  is seen. Due to the dependance of  $\alpha$  on the parameter  $(c_*)^{-7/6}$ , the critical shear can be adjusted. The parameter  $\alpha$  and the electron and ion temperatures  $T_e = TEY$  and  $T_i = TIY$ , on which  $\alpha$  is only dependent, can be seen in figure 6.3.  $\alpha$  does not vary much in time, it mainly shifts the critical shear on the y-axis in figure 6.3 due to the dependence on  $c_*$ .

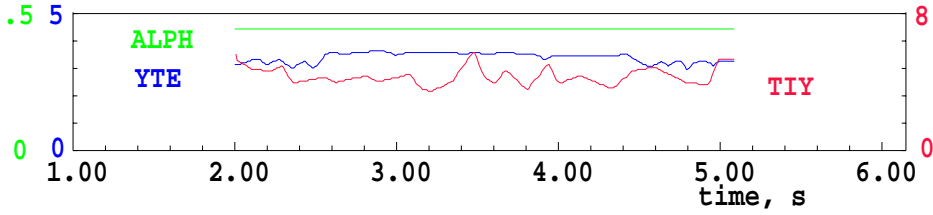


Figure 6.3: The development of the electron temperature  $t_e = TEY$ , of the ion temperature  $T_i = TIY$  and  $\alpha = ALPH$ .  $\alpha$  is only dependent on the temperatures  $T_e$  and  $T_i$ .

The parameter  $c_*$  is dependent on the plasma shape. It has to be of order unity and is chosen to  $c_* = 1$  to represent the experimental observations, while in [13] it is chosen as  $c_* = 3$ . That the chosen parameter is different to that in [13] can be explained by the differences in the plasma shape. In the section 2.2.2, it is shown that  $c_*$  is supposed to be between two and four. On the one hand, unity is very close to the interval 2-4, on the other hand does a change in the choice of  $c_*$  only affect the position of the curve on the y-axis in figure 6.4. By changing  $c_*$ , the curve is shifted on the y-axis. The parameter in [13] are chosen for simulations for the planned next step fusion device ITER, changes due to the different size and geometry is expected. It has to be shown in future if all chosen constants are the same for all ASDEX Upgrade discharges.

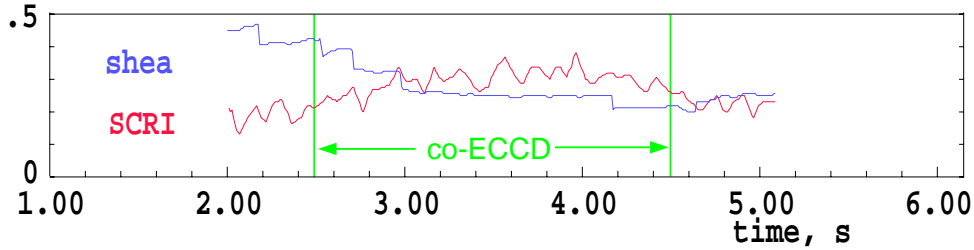


Figure 6.4: The critical shear criterion  $s_1 > s_{crit}$  for the sawtooth onset is not valid during most part of the ECR pulse. The shear at  $q = 1$  *shea* is decreasing with the ECR pulse and after its switch-off slowly recovering. The critical shear *SCRI* is with the ECR onset slowly increasing over the value of the shear at  $q = 1$  and decreasing after the end of the ECR pulse below the level of the shear at  $q = 1$ .

The shear at  $q = 1$  drawn in blue, calculated by ASTRA using the ASDEX Upgrade standard equilibrium reconstruction (FPP), is stronger decreasing with the onset of the ECR than before. During the pulse, the shear is nearly constant until it starts to recover after the switch-off of the ECR. A temporal delay in the shear with respect to the ECR onset is seen until it reaches its constant value and until it recovers. This is expected because a change in the shear is a resistive process taking place with the long resistive time scale. The red curve, the critical shear, starts to slightly increase with the beginning of the ECR pulse and remains about constant until it starts to decrease with the end of the ECR pulse. The Gaussian deposition profile of the ECR can be seen on the right side of figure 6.5.

In ASTRA, the  $q$ -profile tends to be higher than in experimental observations. The result is for

this simulation, that the average  $q = 1$  radius is too low. To be consistent, all values are taken at the  $q = 1$  position calculated by ASTRA. However in the case of the poloidal beta, this has a huge influence. As seen in figure 6.5,  $\beta_{pol}$  increases strongly towards the plasma centre.

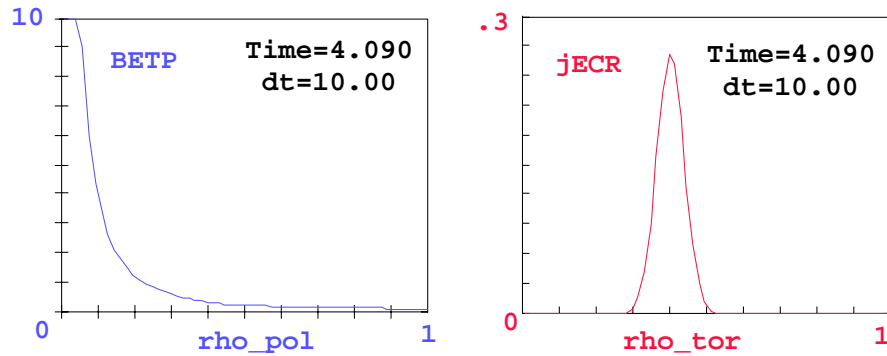


Figure 6.5: *Left side:* Profile of  $\beta_{pol} = BETP$  at  $t = 4.09$  over the flux co-ordinate  $\rho_{tor}$ . A huge change in  $\beta_{pol}$  is seen for small variations in the position of the  $q = 1$  surface. *Right side:* Gaussian deposition profile  $jECR$  over the flux co-ordinate  $\rho_{tor}$  with off-axis deposition.

In figure 6.5, the profile of the  $\beta_{pol}$  is seen. For very small variations in the position of the  $q = 1$  surface, large changes in  $\beta_{pol}$  are observed. In the simulation, only  $\beta_{pol}$  is used as if  $q = 1$  would be situated at a fixed position. The critical shear criterion is not influenced by this fixation, only the energy potentials. This change is discussed later in this chapter. In figure 6.9, the change of the local  $\beta_{pol1}$  with an average  $q = 1$  radius of 0.2 m.

In figure 6.6, the pressure and density scale lengths are shown. The pressure scale length  $r_p = SCAP$  in the blue curve, shows no tendency to lead the development in the critical shear due to  $s_{crit} \sim r_p^{-1/6}$ . The same dependence as the final critical shear is seen in the density scale length  $r_n = SCAN$ . The critical shear depends on the density scale length with  $s_{crit} \sim r_n^{-1}$ .

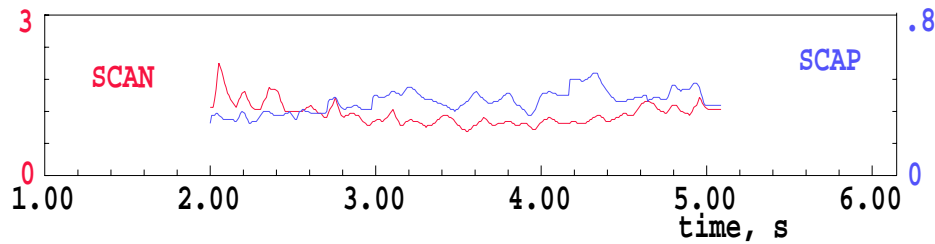


Figure 6.6: The pressure scale length  $SCAP$  shows the same development as the critical shear. The density scale length  $SCAN$  is about constant and does not influence the critical shear in a way leading to the main development of the critical shear.

Figure 6.7 shows the development of the average  $q = 1$  radius. The critical shear is dependent on the average  $q = 1$  radius through the Reynolds number and the normalization of the pressure and density scale lengths. The total dependence results into  $((r_1^2)^{1/3} \cdot r_1^{-1})^{1/2} \cdot (r_1^{-2})^{7/12} \cdot r_1 \cdot$

$r_1^{1/6} = r_1^{-1/6}$ . This explains well the inverse behaviour of the critical shear compared to the critical shear.

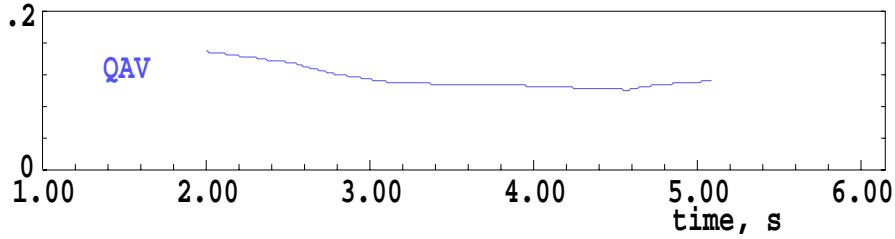


Figure 6.7: Development of the average radius of the  $q = 1$  surface  $QAV$ , showing the same tendency as the critical shear.

The magnetic Reynolds number  $SMR$  is drawn in figure 6.8 in red. It shows the same development as the critical shear due to its quadratic dependence on the average  $q = 1$  radius. The ion Larmor radius  $RLI$ , the blue curve, does not change much except some variations. The ion Larmor radius cannot be the driving force in the development of the critical shear.

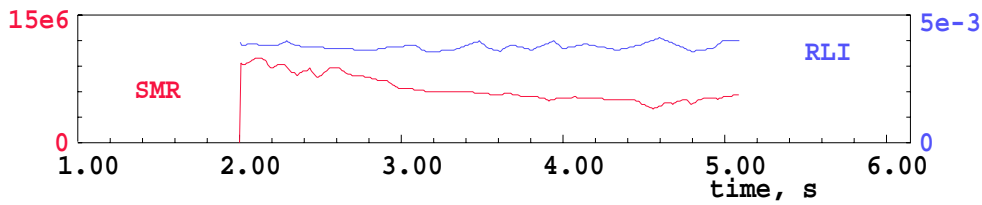


Figure 6.8: The magnetic Reynolds number  $SMR$  shows the same development as the critical shear due to its quadratic dependence on the average  $q = 1$  radius. The ion Larmor radius  $RLI$  does not change much except some variations.

Finally, the last dependence not yet discussed, is the dependence of the critical shear on the ion toroidal  $\beta_{i1}$  at the  $q = 1$  surface. It is shown in figure 6.9 as the red curve with  $BI1 = \beta_{i1}$ . No clear change in beta is seen, except some variations. Consequently,  $\beta_{i1}$  is not the critical parameter influencing the critical shear in the observed development.

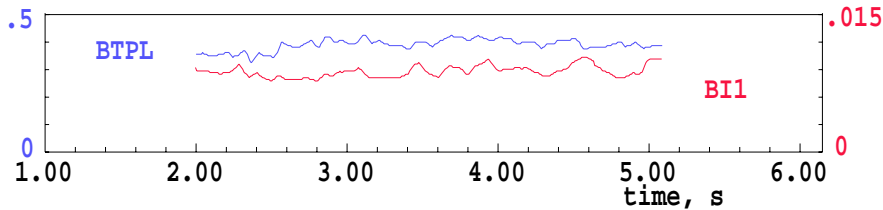


Figure 6.9: Time trace of poloidal  $\beta_{pol} = BTPL$  with fixed average  $q = 1$  radius of 0.2 m and ion toroidal  $\beta_{i1}$  at the  $q = 1$  surface

The main driving forces in the development of the critical shear are the density scale length and the average  $q = 1$  radius. The actual development of the  $q$ -profile can be seen in figure 6.10. The profiles of the safety factor  $q$ , of the inverse of the safety factor, the rotational transform,  $1/q = \mu$  and the shear before the ECR is deposited with driving co-ECCD, during the deposition (from 2.5 s - 4.5 s) and after the ECR deposition.

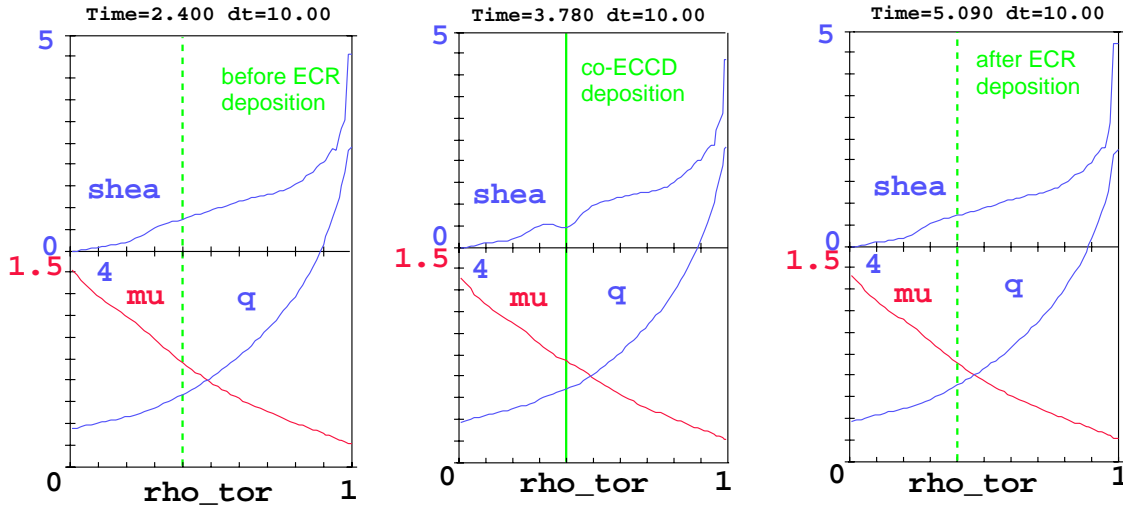


Figure 6.10: Profiles of the safety factor  $q$ , the inverse of the safety factor  $1/q = \mu$  and the shear before, while and after the off-axis co-ECCD deposition.

Clearly, the change in the shear can be seen. However, the change in  $q$  and  $\mu$  is very small, so that it is difficult to recognize the difference in figure 6.10.

In the following figures, the different energy functionals are shown. The Bussac term  $DWBU$  drawn in the red curve in figure 6.11 added to the elongation term  $DWEL$  in blue results in the MHD term  $DWMH$ , seen in figure 6.12. Both terms are negative leading to a negative potential MHD energy as expected.

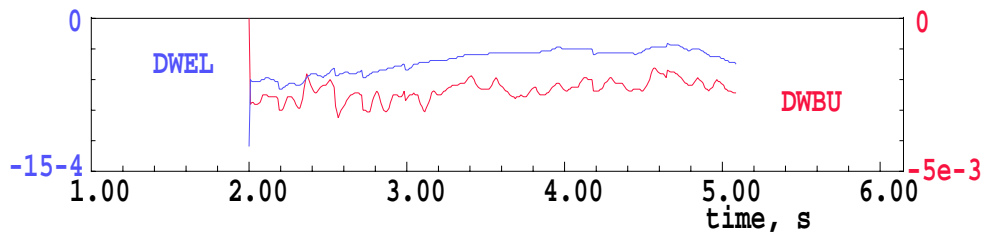


Figure 6.11: As expected, the Bussac energy potential  $DWBU$  and the elongation term  $DWEL$  are negative, which results in a destabilizing effect.

Additional to the negative red curve for the MHD energy potential, in figure 6.12 the Kruskal-Obermann term  $DWKO$  is shown in blue. As expected for standard tokamak profiles, this term is positive which means stabilizing.

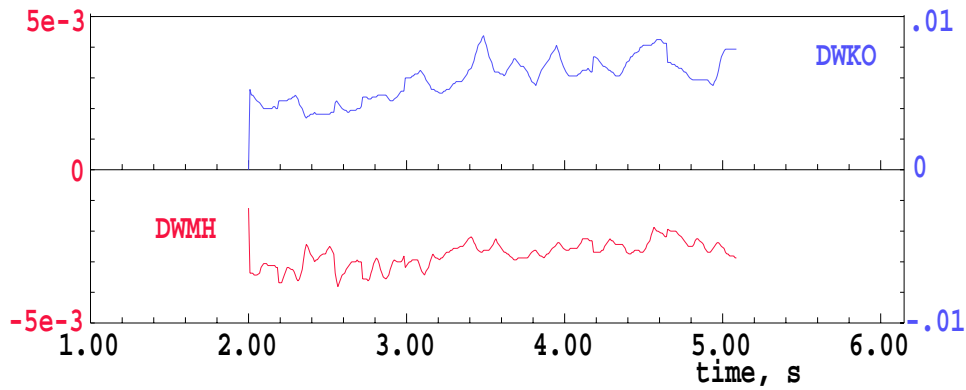


Figure 6.12: The MHD term, a combination of the Bussac and elongation terms,  $DWHM$  is negative as expected. The Kruskal-Obermann term  $DWKO$  shows the stabilizing effect of the collisionless trapped thermal particles with its positive sign.

In figure 6.13, the fast particle term is seen, drawn in blue. As well as the Kruskal-Obermann term, the fast particle term  $DWFA$  is positive as expected due to the stabilizing effect of fast particles. The core energy potential  $DWCO$ , as presented in 6.1, here as a red curve, is the addition of the MHD term with the Kruskal-Obermann term. The destabilizing MHD effect exceeds the stabilizing effect of the collisionless trapped thermal particles, resulting in a negative term for the core energy potential.

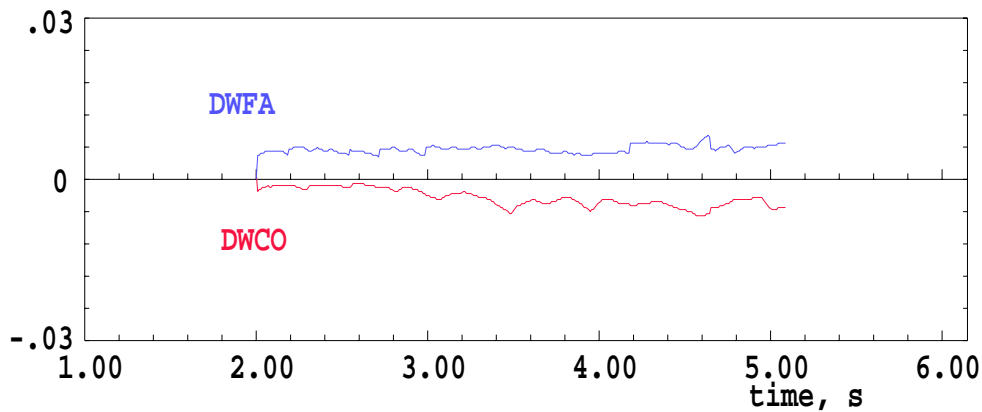


Figure 6.13: The core energy functional  $DWCO$  is negative, which means the negative destabilizing MHD energy exceeds the stabilizing Kruskal-Obermann part. The fast particle term  $DWFA$  representing the fast particle stabilization, is positive as expected.

Previously, it was mentioned that the  $q$  value at which the local  $\beta_{pol,1}$  is used, is fixed by choosing the average  $q = 1$  radius constant. If the average  $q = 1$  radius is used for the local  $\beta_{pol,1}$ , the inequality  $-c_p \hat{\rho} < -\delta \hat{W} < 0.5 \omega_{*i} \tau_A$  is no longer valid, as can be seen in figure 6.14.

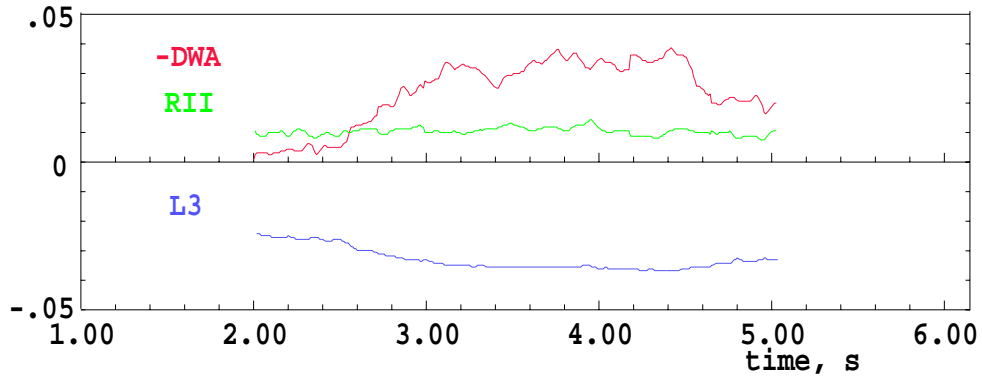


Figure 6.14: Change in the total energy functional  $-\delta\hat{W}$  in comparison with the left side  $L3$  and the right side  $RII$  of the inequality belonging to the critical shear criterion.

Due to the strong dependence on  $\beta_{pol}$  of the Bussac term of the energy functional, this term decreases drastically with  $\beta_{pol}$ .  $\delta\hat{W}_{Bus}$  would dominate the total energy functional. Due to the neutral beam heating, it is not necessarily expected that the critical shear criterion is valid. The fast particle term might play an important role. However, at JET it was found by Angioni [35], that  $-\delta\hat{W}$  becomes so negative, that the left part of the inequality  $-c_p\hat{\rho} < -\delta\hat{W} < 0.5\omega_{*i}\tau_A$  is no longer valid. This is the opposite effect than observed without fixing  $\beta_{pol}$ .

In the simulation in figure 6.15 the bootstrap current is added to the current profile. This self-created current due to the pressure gradient and the precession of the fast trapped particles is situated mainly off-axis. However, the whole current profile changes due to this additional current. This change in the current profile results in a decrease of the shear at the  $q = 1$  surface without recovering after the switch-off of the ECR.

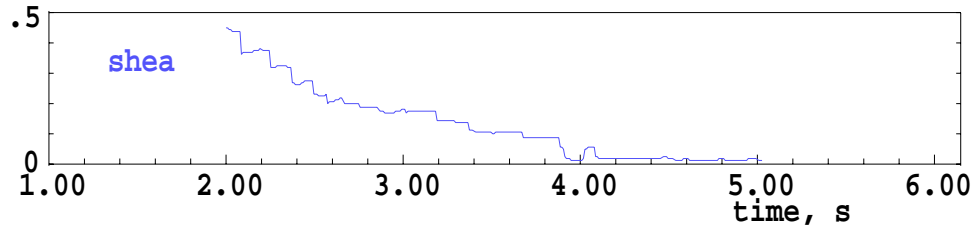


Figure 6.15: Development of the shear at the  $q = 1$  surface by taking the influence of the bootstrap current into account. The central  $q$  is in contradiction to the experiment decreasing without recovery after the end of the ECR pulse.

In the experiment, the sawtooth precursor is observed at the same  $q$  value as before the ECR pulse. This is a strong indication that the  $q$ -profile has recovered to similar values as before the ECR pulse. Because of this result that is not representative for the experimental observations, the bootstrap current was not taken into account in the simulation, presented above. However, due to correct signs of the different terms of the energy potential and the reasonable development of the critical shear, it can be assumed that the simulation is reasonable.

A rough estimate was given of the different terms in the Porcelli criteria. The critical shear criterion seems to be the valid criterion for the sawtooth onset. Two effects have been identified: The change in the critical shear (due the development of the average radius of the  $q = 1$  surface the density scale length) and the shear itself. The leading order physics is expected to be identified but the simulation is far from being quantitative.

In future simulations, a  $q$ -profile closer to the experimental profile has to be specified at  $q_0$  and  $q = 1$  by using SXR and ECE data. If the  $q$ -profile is fixed, the bootstrap current can be reintroduced without leading the shear close to zero, which means the central  $q$  to one or even above one. Usually, more reliable  $q$  profiles can be found due to the combination of Motional Stark Effect (MSE) measurements with the equilibrium reconstruction. However, the diagnostic is currently not available.

### 6.3 Modelling of Central Counter-ECCD Deposition

By modelling the discharge #15847 (gyrotron power ramp, compare figure 4.13), it will be seen, that due to the central counter-ECCD deposition, the central shear is reversed. However, the Porcelli model is derived for monotonic increasing  $q$ -profiles. It cannot be applied for counter-ECCD discharges with central deposition. Even though the Porcelli model cannot be applied, modelling of  $q$  profile and the shear with ASTRA is still possible.

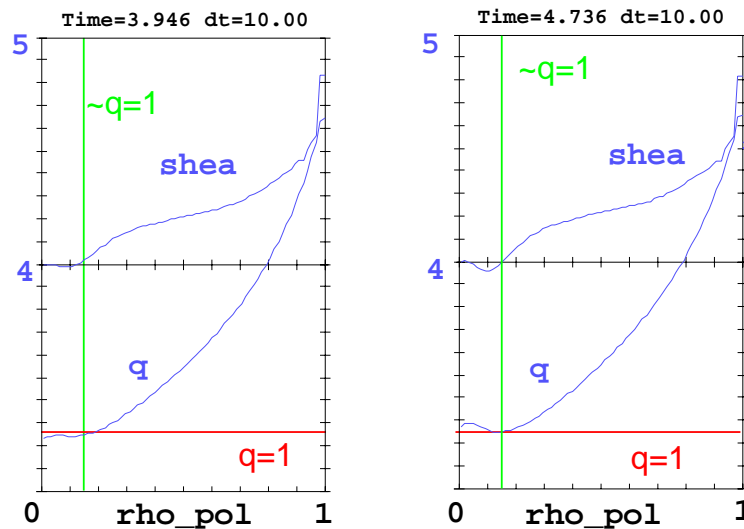


Figure 6.16:  $q$  profile and shear with central counter-ECCD deposition of #15847 for 3.946 s (still sawteeth present) and 4.736 s (sawtooth suppression).

In figure 6.16, the profiles of the shear and of  $q$  are shown for the time point  $t = 4.74$  s. At this time, the sawteeth are suppressed in #15847. Marked with a green line is the assumed  $q = 1$  surface. The position of the  $q = 1$  calculated by ASTRA (marked with a horizontal line) is consistent with the assumed position, the derivative of the  $q$ , the shear, becomes zero.

For counter-ECCD deposition inside, but close to  $q = 1$ , a decrease of the shear would be expected which is supposed to have a stabilizing effect on the sawteeth. However, in #15847 as described in section 4.3, the sawtooth period even slightly shortens before the sawteeth disappear. If the decrease of the shear would be the stabilizing effect, the sawtooth period would become longer.

By comparing the earlier time point when there is still sawtooth activity (left figure of 6.16 with later time point when the sawteeth are suppressed (right figure), it is seen that the central  $q$  is very flat but below unity then rises and reverses. When the sawteeth disappear, the minimum of  $q$  seems to be unity. In the case of reversed shear and a minimum  $q$  below unity, two  $q = 1$  surfaces exist. In this case, sawtooth crashes can happen due to the field line breaking on both  $q = 1$  surfaces [42], [43]. However, in figure 6.16 it seems that in #15847 only one  $q = 1$  surface exists in the minimum of the  $q$  profile. It is possible that the minimum  $q$  is even slightly higher than unity. With a  $q$  profile only just above unity, a (1,1) mode can still exist, but without showing sawtooth activity. The destabilized (1,1) mode, as mentioned in section 4.3 might be strong enough that no impurity accumulation takes place and sawteeth are not “necessary”. However, it has to be kept in mind that the equilibrium reconstruction, calculating the  $q$ -profile, is not exact especially in the plasma centre.

It can be concluded, that the combination of the destabilization of the (1,1) mode together with a minimum  $q$  of unity with reversed shear and  $q$ -profile might lead to the observed sawtooth suppression.



# Chapter 7

## Conclusions and Outlook

In this work, active control of a magnetohydrodynamic instability, the so-called sawtooth instability, occurring in magnetically confined fusion plasmas is investigated. Mainly the variation in the sawtooth period due to changing the Electron Cyclotron Resonance Heating and Current Drive (ECCD) in co and counter direction to the main plasma current is studied. Part of this thesis work was operating and designing a new system for the Soft X-Ray (SXR) diagnostic, an important tool in observing sawtooth instability.

The SXR system uses semiconductor diodes to measure the plasma radiation. This radiation consists of continuous background radiation, dependent on the bremsstrahlungsspektrum and the line radiation of partly ionized impurities. In the former system, the diodes are arranged radially around a pinhole. The advantage of these diodes is their flexibility of single diodes compared to a diode chip. Only single diodes can be ordered radially around the pinhole, resulting in the same focal length for all diodes. These diodes have a large surface, resulting in high intensity of the signal with good resolution. A disadvantage is that they have a very high replacement cost.

The new cameras are equipped with flat diode chips, containing 35 diodes. The advantage of these diode chips is the far cheaper cost. One diode chip has half the cost of one single diode. The cameras are designed to allow an easy removal of the chip. Due to very likely neutron damage, the diodes need replacement approximately every other year to guarantee good signals. The disadvantage of the diodes on the chip is its smaller size. Due to the smaller size, the intensity and resolution reduces. However, the camera itself can be constructed in a smaller size. This is an important advantage due to lack of space in the vacuum vessel.

A test system was successfully installed in April 2002. A clearly improved resolution is observed for mode activity in the high frequency range compared to former diodes, approximately 1.5 years old. Two more cameras were constructed in summer 2003 and included in the torus in August 2003. These three cameras are situated close to the midplane and more cameras will be installed to allow high quality tomographic reconstruction.

The SXR was the main diagnostic used to investigate the sawtooth instability. In a simple model of this instability, the fast ejection of the hot plasma core leads to a change in the central temperature of the form of a sawtooth. One goal of this thesis was to learn how to control

the sawtooth period, the time between two sawtooth crashes. The control of the sawtooth period was investigated using the very localized electron cyclotron resonance heating (ECRH) and current drive (ECCD). The amount of ECR heating power is with roughly 10-20% small compared to the main heating power of the neutral beam injection (NBI). However, the neutral beam injection also influences the sawteeth. The influence of the injection geometry of the different neutral beam sources was investigated. As a result, the most tangential beam sources with the most off-axis deposition have a strong stabilizing effect on the sawteeth, which means a strong increase in the sawtooth period. It was shown that the neutral beam driven current is probably responsible for this stabilization. It could be excluded that the fast particles created by the NBI are responsible for this effect. Further investigation is planned including modelling of the fast trapped and fast passing particles. Experiments are planned showing the influence of a combination of two beam sources on the sawtooth period, one depositing close to the plasma centre and the second either off- or on-axis, .

It was shown that the sawtooth period can be influenced by ECCD in co or counter direction to the plasma current dependent on the ECR deposition location. Due to the magnetic field dependence of the cyclotron resonance frequency, the deposition location can be varied with the magnetic field. The influence of the ECR deposition location on the sawtooth period was scanned systematically from far on the high field side (HFS) up to the low field side (LFS) by magnetic field ramps. For co-ECCD deposited inside the sawtooth inversion radius destabilization of the sawteeth is observed. The sawtooth period is about half of the sawtooth period without ECR. This destabilization can be explained by the simple picture of a current driven close to the spacial position of the instability. The sawtooth period could be further decreased with increasing ECR power and increasing current drive. A maximum in the sawtooth period is observed for deposition far from the plasma centre . The sawtooth period is about six times higher in this maximum in the field scan than in a reference discharge without ECR. By depositing the ECR where the maximum in the sawtooth period was observed in the magnetic field scans, complete sawtooth stabilization, meaning no sawteeth at all, was observed throughout a whole ECR pulse with its maximum duration of 2 s.

This observation was modelled by implementing the Porcelli model for the sawtooth period into the ASTRA transport code. In this model, three criteria for the sawtooth period are presented. One criterion takes the influence of the fast trapped particles into account, the second one the influence of the thermal trapped particles. Both criteria do not seem to be valid for the modelled discharge. The last criterion predicts a sawtooth if the shear of the magnetic field lines at the position of the instability exceeds a calculated critical shear. Using experimental data in the modelling, this critical shear seems to be influenced mainly by the density scale length and of the radius of the instability deposition. With this analysis, the leading order physics is expected to be identified, however, the modelling is far from being quantitative.

The influence of the current driven against the direction of the plasma current was investigated. In magnetic field scans with counter-ECCD deposition, the reverse to central co-ECCD deposition is observed. A broad maximum in the sawtooth period is found for deposition in the plasma centre. The sawteeth can be completely suppressed throughout a whole ECR pulse with its maximum duration.

As a reference to the current drive experiments, the influence of heating only is investigated. A

similar but much weaker effect than with co-ECCD is seen, clearly showing that the changes in the sawtooth period with co- and counter-ECCD are due to the driven current.

Sawteeth can lead to the triggering of neoclassical tearing modes (NTM). This instability is limiting the stored energy of the plasma. The stabilization of these NTMs was and is under investigation in current research. It was investigated whether the control of one trigger process could prevent the onset of an NTM. The new gained knowledge how to tailor sawteeth was applied on plasmas with far higher heating power. However, it was observed, that the sawtooth behaviour changes with high NBI power. Next to the increased heating power, the five different NBI sources with different injection geometries already influence the sawteeth themselves. This effect has to be taken into account additionally to the effect due to ECCD. However, as a main result of this thesis, the prevention of the NTM was achieved for a complete ECR pulse with off-axis co-ECCD deposition. The deposition has to be chosen very exactly and shifts in the deposition location have to be compensated.

In the future, further investigation of the influence of the neutral beam injection geometry is planned as well as the influence of combinations of beam sources with different injection geometries.

Due to the unclear result in the development of the sawtooth period in the high power NTM experiments, the magnetic field scans are planned to be performed at higher beam power, representing an intermediate NBI power of the previous experiments. The power should not be high enough to trigger NTMs yet, however, a change in the sawtooth behaviour might be observed.

In the high power experiments NTM prevention was achieved for off-axis co-ECCD deposition. It has to be proven that this important result can be reproduced and thus consolidated. Currently, a new ECRH system is under construction with steerable mirrors. In the future, adjustments of the ECR deposition in the upper or lower midplane instead of the HFS or LFS can be done during a discharge by adjusting the mirror angle. The application of a magnetic field ramp would be no longer necessary.

It still has to be shown, if the prevention of NTMs is possible for central deposition due to the creation of fast small sawteeth.

The sawtooth control is already in use for transport investigations with and without sawteeth [41] and in discharges with pellet induced edge localized modes (ELMs) [44]. Further application is planned in so-called advanced scenario discharges where an early NTM triggering may be a problem.

In summary, a method for sawtooth control was established. The modelling of these results led to the identification of the leading physics mechanisms. The triggering of an NTM could be prevented by successfully applying the gained knowledge in sawtooth control.



# Appendix A

## The Tokamak ASDEX Upgrade

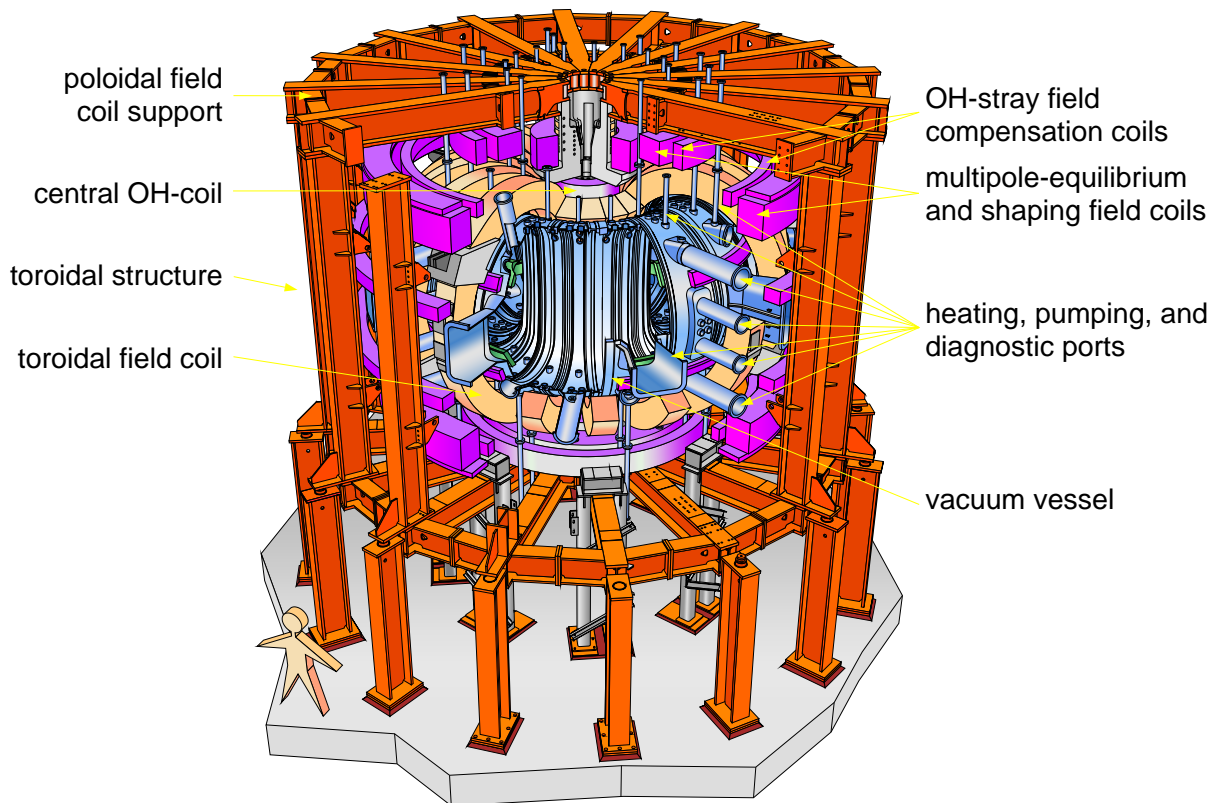


Figure A.1: Outline of the ASDEX Upgrade Tokamak

The tokamak ASDEX Upgrade, an **AxiSymmetric Divertor EXperiment**, has the dimensions of a middle sized tokamak device. A sketch of the vessel can be seen in figure A.1. It is named after its predecessor ASDEX, introducing the very successful divertor concept. A so-called divertor minimizes the interaction of the plasma with the first wall and leads therefore to a better confinement of the plasma. Due to this strongly improved confinement, the principal concept is even transferred to other fusion devices such as stellarators (island divertor). In ASDEX Upgrade, the plasma is controlled via twelve vertical field coils. Usually, the toroidal field is kept constant during a discharge, but it can be varied in the region of 10% of the toroidal field. The set of plasma control coils are connected to a computer with real time control. A large amount of measuring coils are installed in ASDEX Upgrade allowing this computer to find the real values of the plasma position and shape and to correct the current in the main field coils.

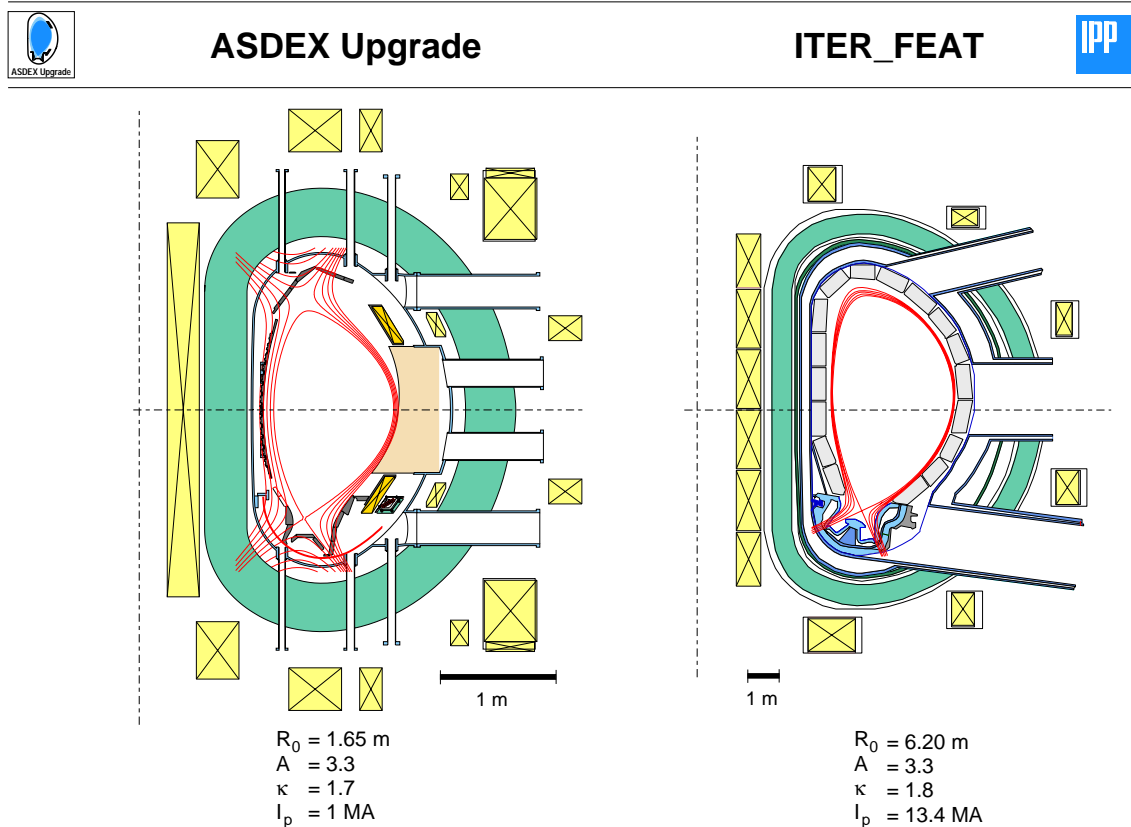


Figure A.2: Comparison of ASDEX Upgrade and the next step fusion device ITER.

A comparison of the poloidal cross sections of ASDEX Upgrade with the recently installed divertor IIb and the future next step fusion device ITER is seen in figure A.2. The cross section of these devices are very similar, showing the ITER relevance of the smaller device ASDEX Upgrade.

The technical data and some typical plasma parameters of ASDEX Upgrade are shown in the following tables.

**Technical data:**

Total height of the experiment	9 m
Total radius over all	5 m
Weight of the experiment	800 t
Material of the first wall	carbon
Number of toroidal field coils	16
Number of poloidal field coils	12
Maximum magnetic field	3.1 T
Plasma current	0.4 MA - 1.6 MA
Pulse duration	< 10 s
Time between pulses	15 - 20 min
Amount of data / pulse	approx. 0.5 GByte
Plasma heating:	up to 27 MW
Ohmical heating	1 MW
Neutral beam injection heating	20 MW (with $^2\text{H} = \text{D}$ )
Injection energy	60 keV and 100 keV
Ion-Cyclotron heating	6 MW (30 MHz - 120 MHz)
Electron-Cyclotron heating	2 x 2 MW (120 GHz)

Table A.1: Technical data of ASDEX Upgrade

**Typical plasma parameters:**

Major plasma radius $R_0$	1.65 m
Minor horizontal plasma radius $a$	0.5 m
Minor vertical plasma radius $b$	0.8 m
Ellipticity $b/a$	1.8
Triangularity (top/bottom)	0.1 / 0.3, since 1999: 0.4 / 0.4
Plasma types	deuterium, hydrogen, helium
Plasma volume	14 m <sup>3</sup>
Plasma mass	3 mg
Electron density	1 x 10 <sup>20</sup> m <sup>-3</sup>
Plasma temperature	60 to 100 million degree

Table A.2: Typical plasma parameters of ASDEX Upgrade



# Appendix B

## Dispersion Relation

The propagation of waves in plasmas is limited due to reflection layers, called cut-offs, and absorption of the wave. The propagation is calculated by combining Faraday's and Ampère's law:

$$\nabla \times \nabla \times \mathbf{E} = -\epsilon_0 \mu_0 \frac{\partial^2 \mathbf{E}}{\partial t^2} - \mu_0 \frac{\partial \mathbf{j}}{\partial t} \quad (\text{B.1})$$

By describing the electric and magnetic fields via plane waves  $\psi = \psi_0 \cdot \exp[i(\mathbf{k} \cdot \mathbf{r} - \omega t)]$  one achieves the wave equation in the  $\omega$ - $\mathbf{k}$  space (with  $\epsilon_0 \mu_0 = 1/c^2$ ):

$$\mathbf{k} \times (\mathbf{k} \times \mathbf{E}) + \frac{\omega^2}{c^2} \cdot \epsilon \cdot \mathbf{E} = 0 \quad (\text{B.2})$$

with the dielectric tensor  $\epsilon$  [45]

$$\epsilon = \begin{bmatrix} S & -iD & 0 \\ iD & S & 0 \\ 0 & 0 & P \end{bmatrix} \quad (\text{B.3})$$

with

$$S = 1/2(R + L) \quad (\text{B.4})$$

$$D = 1/2(R - L) \quad (\text{B.5})$$

$$R = 1 - \sum_{j=e,i} \frac{\omega_{pj}^2}{\omega^2} \left( \frac{\omega}{\omega + q_j \omega_{cj}} \right) \quad (\text{B.6})$$

$$L = 1 - \sum_{j=e,i} \frac{\omega_{pj}^2}{\omega^2} \left( \frac{\omega}{\omega - q_j \omega_{cj}} \right) \quad (\text{B.7})$$

$$P = 1 - \sum_{j=e,i} \frac{\omega_{pj}^2}{\omega^2} \quad (\text{B.8})$$

The cyclotron frequency  $\omega_{cj}$  is defined as

$$\omega_{cj} \equiv \frac{e \cdot B_0}{m_j} \quad (\text{B.9})$$

$q_j$  becomes  $q_e = -1$  and  $q_i = +1$ . The plasma frequency can be written as

$$\omega_{pj}^2 = \frac{q_j^2 n_j}{m_j \epsilon_0} \quad (\text{B.10})$$

with  $j = e, i$ .

If  $\mathbf{k}$  is replaced by the refraction index  $\mathbf{N} = \mathbf{k}c/\omega$  and  $\mathbf{N}$  chosen in the x-z surface,  $\mathbf{N} = (N \sin \theta, 0, N \cos \theta)$ , the following set of equations is achieved by using the wave equation (B.2):

$$\|\mathbf{R}\| \cdot \mathbf{E} = \begin{bmatrix} S - N^2 \cos^2 \theta & -iD & N^2 \cos \theta \sin \theta \\ iD & S - N^2 & 0 \\ N^2 \cos \theta \sin \theta & 0 & P - N^2 \sin^2 \theta \end{bmatrix} \cdot \begin{bmatrix} E_x \\ E_y \\ E_z \end{bmatrix} = 0. \quad (\text{B.11})$$

A solution can be found for  $\|\mathbf{R}\| = 0$ , which can be written as the following equation

$$AN^4 - BN^2 + C = 0 \quad (\text{B.12})$$

with

$$A = S \sin^2 \theta + P \cos^2 \theta \quad (\text{B.13})$$

$$B = RL \sin^2 \theta + PS(1 + \cos^2 \theta) \quad (\text{B.14})$$

$$C = PRL \quad (\text{B.15})$$

The solution of equation B.12 becomes

$$N^2 = \frac{B \pm [(RL - PS)^2 \sin^4 \theta + 4P^2 D^2 \cos^2 \theta]^{1/2}}{2A}. \quad (\text{B.16})$$

Becomes the refraction index  $N \rightarrow 0$ , the wave encounters a cut-off and is reflected. For  $N \rightarrow \infty$ , the resonance condition is fulfilled, the wave is absorbed. Depending on the propagation angle, different types of waves are found. The propagation of these waves can be seen in the Clemmov-Mullaly-Allis diagramme [46] in figure B. The x-axis is density dependent and the y-axis magnetic field dependent. The small diagramme show polar diagrammes, showing the angular dependence of the different wave types.

For parallel propagation with  $\Theta = 0$ , for  $P = 0$  the electron plasma oscillation is described.  $N^2 = R$  becomes the transversal right circular polarized wave with the righthand cut-off for  $R = 0$ . The mode is absorbed for  $R = \infty$ , the electron cyclotron resonance.  $N^2 = L$  gives the left circular polarized wave, reflected at the lefthand cut-off  $L = 0$ . Absorption takes place for  $L = \infty$ , the ion

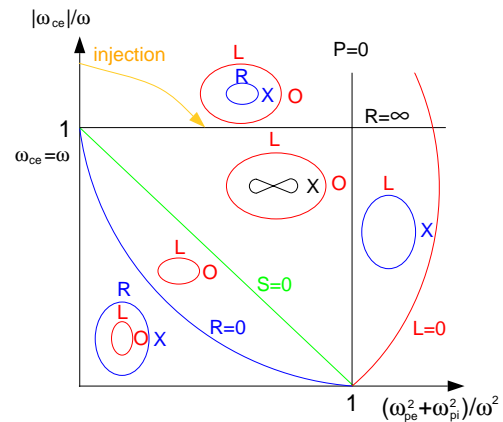


Figure B.1: Clemmov-Mullaly-Allis diagramme

cyclotron resonance.  $N^2 = L$  gives the left circular polarized wave, reflected at the lefthand cut-off  $L = 0$ . Absorption takes place for  $L = \infty$ , the ion

cyclotron resonance.

If the wave propagates in a transversal direction, the solution  $N^2 = P$  gives the ordinary wave (O-mode), reflected at the plasma cut-off  $P = 0$ . The extra-ordinary wave (X-mode)  $N^2 = RL/S$  is reflected at the cut-offs  $R = 0$  or  $L = 0$  and absorbed at  $S = 0$ , the upper hybrid resonance.

The orange curve in figure B.1 outlines the wave propagation in ASDEX Upgrade. The second harmonic of the electron cyclotron wave is launched in X-mode. The wave can penetrate the plasma up to the centre without encountering any cut-offs, until it is absorbed at the electron cyclotron resonance  $R = \infty$ . A wave in X-mode launched in the frequency of the first harmonic would be reflected at righthand cut-off  $R = 0$ . The wave cannot propagate in the region between  $R = 0$  and  $S = 0$ . The wave could not reach the resonance.



# Appendix C

## Kadomtsev Model

Figure 2.9 was created by using examples of the initial and final helical flux function, the corresponding parabolic current profile and the safety factor profile[7]. The magnetic field was chosen as  $B_0 = 2.0$  T,  $R$  as major radius of ASDEX Upgrade  $R = 1.65$  m, the central safety factor as  $q_0(0) = 0.95$  and  $r_s = 0.25$  m.

$$\psi_{initial}(r) = \frac{B_0}{R} \left( \frac{1}{q_0(0)} - 1 \right) \frac{r^2}{2} \left( 1 - \frac{r^2}{2r_s^2} \right) \quad (C.1)$$

$$j_{initial}(r) = \nabla^2 \psi_0 + 2B_0/R = \frac{2B_0}{Rq_0(0)} \left( 1 - 2(1 - q_0(0)) \frac{r^2}{r_s^2} \right) \quad (C.2)$$

$$q_{initial}(0) = \frac{rB_0}{R} \left( \frac{d\psi_0}{dr} + \frac{rB_0}{R} \right)^{-1} = \left[ 1 + \left( \frac{1}{q_0(0) - 1} \right) \left( 1 - \frac{r^2}{r_s^2} \right) \right]^{-1} \quad (C.3)$$

By using area conservation

$$r_1 |dr_1| + r_2 |dr_2| = r |dr| \quad (C.4)$$

with  $dr_1 < 0$  and  $dr_2 > 0$  for  $dr > 0$  (see figure C) equation C.4 can be solved to

$$r_2^2 - r_1^2 = r^2 \quad (C.5)$$

This means, after the completed reconnection and the restoration of the poloidal symmetry, each reconnected surface forms a circle with a radius  $r$ . With equation C.1 in the helical flux conservation  $d\psi^* = \text{const}$ .

$$d\psi^* = \frac{d\psi_0}{dr} \Big|_1 dr_1 = \frac{d\psi_0}{dr} \Big|_2 dr_2 = \frac{d\psi_{final}}{dr} dr \quad (C.6)$$

one obtains the corresponding functions after the sawtooth crash

$$\psi_{final}(r) = \frac{B_0}{R} \left( \frac{1}{q_0(0)} - 1 \right) \frac{r_1^4}{4} \left( 1 - \frac{r^4}{4r_1^4} \right) \quad (C.7)$$

$$j_{final}(r) = \frac{2B_0}{R} \left[ 1 - \frac{1}{2} \left( \frac{1}{q_0(0)} - 1 \right) \frac{r^2}{r_1^2} \right] \quad (C.8)$$

$$q_{final}(r) = \left[ 1 - \left( \frac{1}{q_0(0)} - 1 \right) \frac{r^2}{4r_1^2} \right]^{-1} \quad (C.9)$$

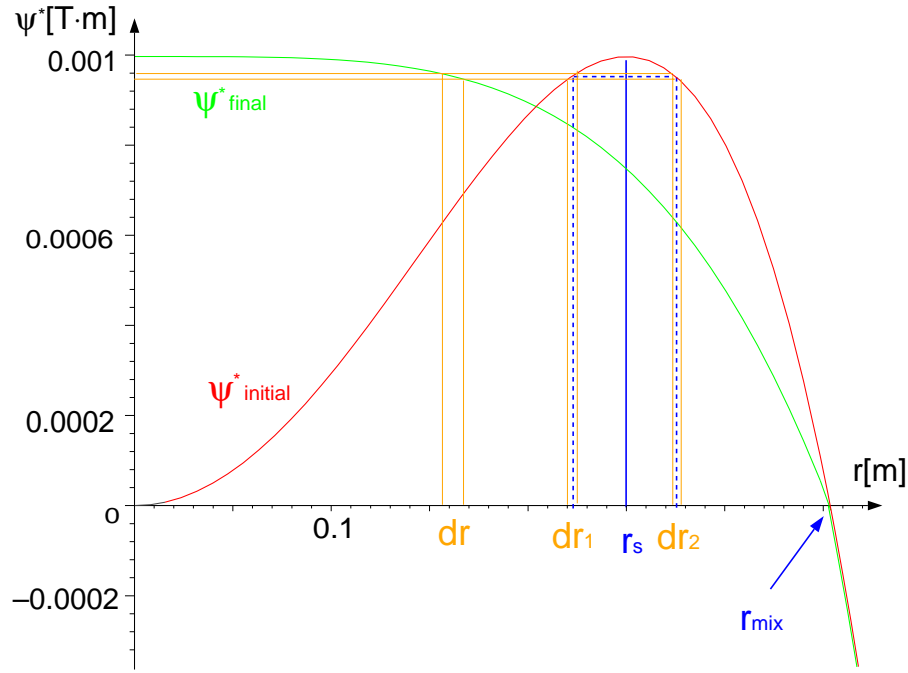


Figure C.1: The flux function  $\psi$  before and after a sawtooth crash

# Appendix D

## Sawtooth Period Scans without Normalization

By ramping the magnetic field, the ECR deposition can be shifted. As presented in chapter 4, three series magnetic field scans are performed: one for co-ECCD, one for counter-ECCD and one as a reference with pure heating. These discharges are mainly neutral beam heated plasmas, using two neutral beam sources, however not always the identical sources. The influence of the injection geometry of different neutral beam sources on the sawtooth period is investigated. It is found that the sources with the most off-axis deposition and most tangential injection have a completely different effect on the sawtooth period than the other beam sources.

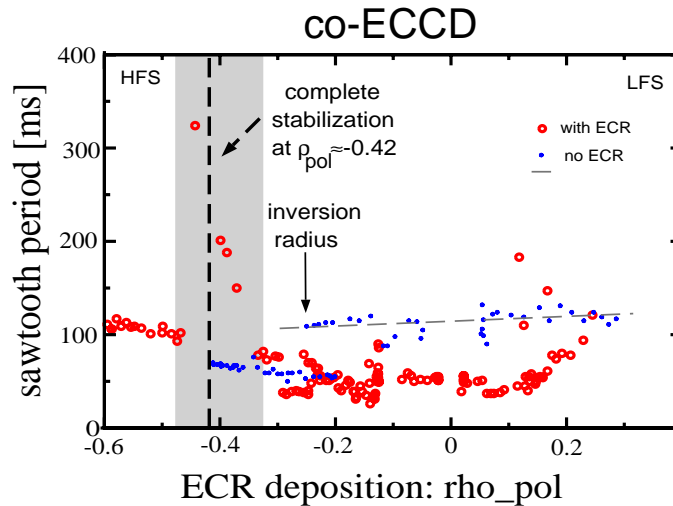


Figure D.1: Magnetic Field Scan with co-ECCD. The sawtooth period in [ms] is drawn over the ECR deposition in  $\rho_{pol}$ .

This change in the sawtooth period motivated the normalization of the sawtooth period, influenced by ECR, with the period of an identical discharge without ECR. Due to this normal-

ization, the effect of the injection geometry is taken out. By the normalization, the absolute value of the sawtooth period in [ms] cannot be seen. In figure D.1, the sawtooth period without normalization is shown over the ECR deposition, driving co-ECCD.

Between two discharges, jumps in the sawtooth period with and in the ones without ECR can be seen. These jumps vanish by the normalization. In the following figures D.1 and D.3, the magnetic field scans are shown for counter-ECCD and pure heating without normalization.

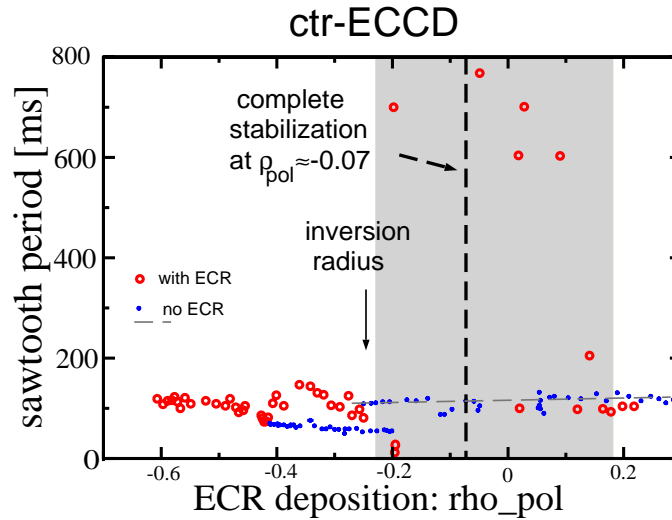


Figure D.2: Magnetic Field Scans showing the sawtooth period over  $\rho_{pol}$  with counter-ECCD.

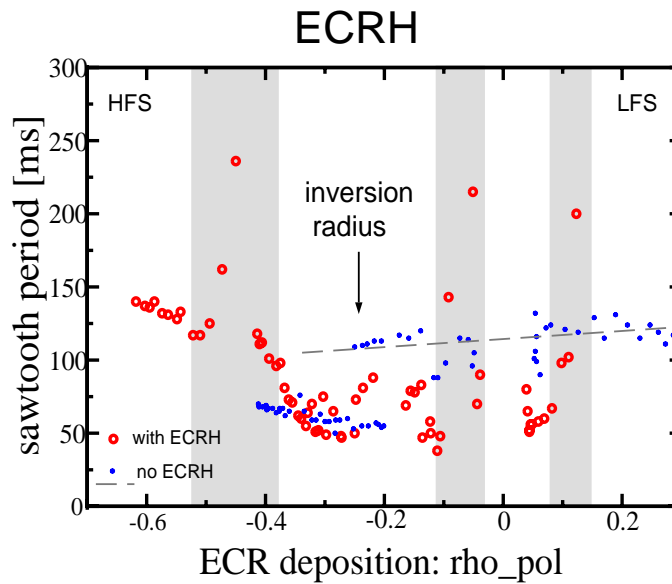


Figure D.3: Magnetic Field Scan with ECRH. One ECR mirror is set for co-ECCD, the second for counter-ECCD. The total current adds up to nearly zero.

# Appendix E

## Mode Amplitude Analysis

The mode amplitudes of some discharges are listed in the following tables. The time point of the analysis is given as well as the mode position, found by SXR analysis. “C” is written for the SXR C camera, as well as “A” for the A camera with lines of sight rectangular to the C camera, and “B” for the B camera. The relative mode amplitude found by using the SXR is given in  $2|fft/fft0|[\%]$  as the ratio of the first and the zero component of a Fast Fourier Transformation (FFT). However, this amplitude is still not absolute, because it does not take the slope of the zero component of the FFT into account, which means the peakedness of the signal. For the C camera, the relative amplitude of the (1,1) mode is divided with the slope of the zero FFT component at the  $q = 1$  position: absolute amplitude = relative amplitude/ $[\Delta FFT0/\Delta\rho_{pol}]|_{q=1}$ .

The mode amplitude calculated with the Mirnov diagnostic is given as  $MTR [T] = \dot{B}[T/s]/\omega[1/s]$ .

Discharge #14987 with complete sawtooth stabilization with co-ECCD (MiniSoX C-camera not yet installed):

time	$\rho_{pol}$	B	A	MTR [ $10^{-3}$ mT]	comment
2.3s	0.20	3.9%	15%	2.5/19000=0.132	before ECR
3.29s	0.20	1.4%	5%	1.7/16500=0.103	with ECR
4.74s	0.15	2.8%			after ECR
4.73s	0.15	3.1%			after ECR

Ctr-ECCD gyrotron power ramp up, discharge #15847:

time	$\rho_{pol}$	C abs.	A	MTR [ $10^{-3}$ mT]	comment
ca. 1.8s	0.25	3.2%	5.5%	no MTR	before ECR
2.51s	0.25	5%	2.6%	no MTR	with ECR
4.1s	0.25	2%	0.8%	no MTR	with ECR

Discharge #16841 with central ctr-ECCD deposition,  $P_{NBI} = 12.5$  MW, no feedback control:

time	$\rho_{pol}$	C abs.
3.37s	0.25	2.3%

Discharge #16842 without ECR deposition:

time	$\rho_{pol}$	C abs.
2.32s	0.25	3.5%

Discharge #16843 with central co-ECCD deposition,  $P_{NBI} = 12.5$  MW, no feedback control:

time	$\rho_{pol}$	C abs.
2.31s	0.25	1.7%
3.25s	0.25	1.1%

Discharge #16862 with co-ECCD deposition,  $P_{NBI} = 12.5$  MW, no feedback control:

time	$\rho_{pol}$	C abs.	A	B	MTR [ $10^{-3}$ mT]	comment
2.12s	0.20	3.9%	13%		9/17300=0.520	before ECR
2.31s	0.18	3.0%	5%		14/17900=0.782	before ECR
2.67s	0.3	0.68%	2%		9/15400=0.584	with ECR
3.04s	0.25	0.96%	1.5%		10/15700=0.637	
3.36s	0.25	0.67%	10%	9%	23/17400=1.322	
3.775s	0.25	0.63%	20%		26/19000=1.368	NTM trigger

Discharge #16863 with ctr-ECCD deposition,  $P_{NBI} = 12.5$  MW, no feedback control:

time	$\rho_{pol}$	C abs.	A	MTR [ $10^{-3}$ mT]	comment
2.31s	0.25	1.4%	5%	15/17600=0.852	before ECR
3.26s	0.2	0.9%	3%	10/17400=0.575	
3.35s	0.25	3.0%	5%	14/17800=0.787	
3.368s	0.25	3.1%	7%	15/16900=0.888	NTM trigger

Reference discharge without ECR #16864,  $P_{NBI} = 12.5$  MW, no feedback control:

time	$\rho_{pol}$	C abs.	A	MTR [ $10^{-3}$ mT]	comment
2.1s	0.2	3.8%			before ECR
2.8s	0.3	2.6%	4.5%	18/16000=1.125	
3.08s	0.22	5.8%	15%	20/19000=1.053	
3.19s	0.3	3.3%	15%	30/17000=1.765	about NTM trigger

Repeat of discharge with successful NTM prevention with half the ECR power. In #17142 NTM was triggered:

time	$\rho_{pol}$	C abs.	comment
1.67s	0.28	2.6%	before ECR
2.82s	0.3	2.1%	with ECR

Discharge #17235 with co-ECCD deposition,  $P_{NBI} = 12.5$  MW, with feedback control, no NTM up to ECR switch-off:

time	$\rho_{pol}$	C abs.	A	MTR [ $10^{-3}$ mT]	comment
1.63s	0.28	2.3%			before ECR
3.16s	0.35	2.3%	3%	27/16000=1.688	with ECR
3.73s	0.35	4.5%	6%	27/17000=1.588	sawtooth after ECR

Reference discharge #17238 with ctr-ECCD deposition,  $P_{NBI} = 12.5$  MW, with feedback control, no NTM up to ECR switch-off:

time	$\rho_{pol}$	C abs.	A	MTR [ $10^{-3}$ mT]	comment
1.63s	0.3	2.7%			before ECR
2.8s	0.25	1.2%	2%	4/17500=0.229	
2.81s	0.25	1.4%	2.5%	4/16000=0.25	
3.143s	0.3	2.3%	2.5%	11/18000=0.611	NTM trigger, low amp.

Discharge #16617 without ECR. All neutral beam sources are switched on separately for about one second each:

time	$\rho_{pol}$	C rel.	comment
2.57s	0.3	3%	NBI source 3
3.30s	0.3	4.5%	NBI source 7
4.11s	0.2	3.5%	NBI source 4
5.09s	0.2	3%	NBI source 8
6.16s	0.25	3.5%	NBI source 1
7.35s	0.2	<b>15%</b>	NBI source 6
8.16s	0.25	2.5%	NBI source 2
9.21s	0.2	2%	NBI source 5

# Bibliography

- [1] U. Schumacher, Fusionsforschung: Eine Einführung, Wissenschaftliche Buchgesellschaft, Darmstadt, 1993
- [2] J. Wesson, Tokamaks, Clarendon Press, Oxford, 1987
- [3] J.P. Freidberg, Ideal Magnetohydrodynamics, Plenum Press, New York, 1987
- [4] F. Troyon et al., Plasma Phys. Control. Fusion **26** (1984)
- [5] R.J.Goldston, P.H.Rutherford, Plasmaphysik, Friedr. Vieweg & Sohn Verlagsgesellschaft mbH, Braunschweig/Wiesbaden, 1998
- [6] G. Bateman, MHD Instabilities, The Massachusetts Institute of Technology, 1978
- [7] D. Biskamp, Nonlinear Magnetohydrodynamics, Cambridge University Press, 1993
- [8] S. Günter et al., Nucl. Fusion 39, 1535 (1999)
- [9] T. Kass, Untersuchungen zum Verhalten hochenergetischer Ionen in magnetisch eingeschlossenen Plasmen, PhD Thesis, IPP Report 1/298, 1996
- [10] F. Porcelli, Plasma Phys. Control. Fusion **33** (1991) 1601-1620
- [11] S. von Goeler, W. Stodiek, N. Sauthoff, Phys.Rev.Lett. **33** (1974) 1201
- [12] B. B. Kadomtsev, Sov. J. Plasma Phys., Vol.1, No. 5, Sept.-Oct. 1975, p 389ff
- [13] Porcelli et al., Plasma Phys. Control. Fusion **38** (1996) 2163-2186
- [14] M.N. Bussac, R.Pellat, D. Edery, J.L. Soule, Phys. Rev. Lett. **35** (1975), 1638
- [15] C. Angioni, Modelling of electron transport and of sawtooth activity in tokamaks, LRP 709/01, CRPP Lausanne, 2001
- [16] M.N. Bussac, R.Pellat, D. Edery, J.L. Soule, Proc. 6th Conf. on Plasma Physics and Controlled Nuclear Fusion Research, Berchtesgaden 1976, IAEA, Vol. 1, 607 (1977)
- [17] T.M. Antonsen, Jr. and A. Bondeson, Phys. Fluids B **5** (11), 1993, 4090-4098

- [18] G. Fogaccia and F. Romanelli, *Phys. Plasmas* **2**, 1995, 227-240
- [19] D.J. Campbell et al., *Phys.Rev.Lett.* **60** (1988) 2148-2151
- [20] F. Pegorano, F. Porcelli and T.J. Schep, *Phys. Fluids* **B 1**, 364 (1989)
- [21] L. Zakharov, B. Rogers, *Phys. Fluids* **B 4**, 3285 (1992)
- [22] L. Zakharov et al., The Theory of Stabilization of Sawtooth Oscillations in TFTR Super-shots, PPPL-2953 UC-420,427, Nov. 1993
- [23] R.J. Buttery, *Plasma Phys. Control. Fusion* **42** Suppl. 12B (2000) B61-B73
- [24] H.Zohm et al., *Phys. Plasmas*, Vol.8, No. 5, May 2001
- [25] A. Gude et al., *Nuclear Fusion* 39, No. 1 (1999) 127-131
- [26] O.Sauter et al., *Phys. Rev. Lett.* **88** (2002) 105001
- [27] N.J. Fisch, A.H. Boozer, *Phys. Rev. Lett.* **45** (1980), 720
- [28] E. Poli et al., *Comput. Phys. Commun.* **136**, 90 (2001)
- [29] G. Pereverzev, P.N. Yushmanov, ASTRA Automated System for TRansport Analysis in a Tokamak, IPP report 5/98, 2002
- [30] A.G. Michette and C.J.Buckley, *X-Ray Science and Technology*, Institute of Physics Publishing, Bristol and Philadelphia
- [31] C. Tanzi, Emission of Soft X-Ray and Microwave Radiation from Tokamak Plasmas, PhD thesis 1996, FOM
- [32] M. Sokoll, MHD-Instabilitäten in magnetisch eingeschlossenen Plasmen und ihre tomographische Rekonstruktion im Röntgenlicht, PhD thesis, IPP Garching, IPP Report 1/309, 1997
- [33] H.R. Griem, *Plasma Spectroscopy*, McGraw-Hill, 1964
- [34] M.Bessenrodt-Weberpals et al., *Soft X-Ray Diagnostics for ASDEX Upgrade*, IPP Report 1/290, 1995
- [35] C. Angioni et al., *Nucl. Fusion* **43** (2003) 455-468
- [36] Private Communication with Prof. Sibylle Günter
- [37] H. Zohm et al., *Phys. Plasmas* **8** No. 5 (2001) 2009-2016
- [38] K. Hanada, et al. *PRL* V.66 No.15 (1991) pp. 1974-1977
- [39] Z.A. Pietrzyk et al., *Nucl. Fusion* **39** No. 5 (1999) 587-611

- [40] A. Mück et al., NTM Control via Sawtooth Tailoring in ASDEX Upgrade, Proc. 30th Eur. Conf. on Plasma Phys. and Contr. Fusion, (St. Petersburg, 2003), P1-131
- [41] R. Dux et al., Plasma Phys. Control. Fusion **45** (2003) 1815-1825
- [42] V.V. Parail and G. Pereverzev, Internal Disruption in a Tokamak, Soviet Journal of Plasma Physics **6**(1), 14 (1980)
- [43] R. Bückse, Tomographische Untersuchung Interner Disruptionen an den Tokamaks ASDEX und TFTR, PhD thesis, IPP Garching, IPP Report IPP III/175, 1991
- [44] P.T. Lang et al., Nuclear Fusion 43 (2003) 1110-1120
- [45] D.G. Swanson, Plasma waves, Academic Press Inc., 1989
- [46] T.H. Stix, Waves in Plasmas, American Institute of Physics, 1992



# Appendix F

## Acknowledgement

Diese Arbeit war nur durch die Zusammenarbeit mit vielen Kollegen möglich. Deshalb möchte ich mich bei allen, die mich in dieser Zeit unterstützt haben, bedanken:

Insbesondere bin ich Prof. Zohm für die hervorragende wissenschaftliche Betreuung der letzten Jahre verpflichtet. Er hat mir sehr viel Vertrauen entgegengebracht und mich unterstützt, wo immer es möglich war. Er war immer erreichbar, wenn ich Hilfe benötigte.

Ich möchte Prof. Wilhelm, meinem Doktorvater, für die wissenschaftliche Betreuung meiner Arbeit und seine Unterstützung danken.

Prof. Günter hat sich immer Zeit genommen, wenn ich Fragen hatte und hat viele neue Ideen von der theoretischen Seite eingebracht.

Dr. Marc Maraschek war mir eine unschätzbare Hilfe, ganz besonders zu Beginn meiner Arbeit, als ich mit der Diagnostik und besonders ihrer Software zu kämpfen hatte. Er hat die ganze Zeit hinweg alle meine Fragen geduldig beantwortet und ist immer bei der Diagnostikbetreuung eingesprungen, wenn ich selbst verhindert war.

Ohne Hans Krippner wäre die SXR Diagnostik nicht funktionsfähig. Seine freundliche und kompetente Unterstützung hat mir die Arbeit sehr erleichtert.

Dr. François Ryter und Dr. Fritz Leuterer für die Hilfe bei der Entwicklung und Durchführung meiner Experimente.

Dr. Anja Gude möchte ich für die klare und strukturierte Einführung in die Diagnostik danken. Ihre übersichtliche Organisation hat mir die Suche nach wichtigen Unterlagen sehr erleichtert.

Dr. Stjepko Sesnic war mir in der weiteren Einweisung in die SXR Diagnostik, mit guten Ratschläge beim Design des neuen Systems und beim Korrekturlesen der Arbeit eine wertvolle Hilfe.

Dr. Sören Klose danke ich für die große Unterstützung, insbesondere bei der Diagnostikbetreuung in der Endphase meiner Arbeit.

Dr. Luis Giannone hat stets meine Fragen zum Programmieren und zur Physik mit sehr viel Geduld beantwortet und die gesamte Arbeit korrekturgelesen.

Lucy Scoones gelang es mein Englisch durch qualifizierte Veränderungen deutlich zu verbessern.

Dr. Grigory Pereverzev hat mich bei der ASTRA Modellierung unterstützt. Er hat sich lange Zeit genommen um meine Fragen zu beantworten.

Dr. Clemente Angioni war mir eine große Hilfe beim Verständnis und der Anwendung des Porcelli Modells.

Many thanks to Dr. Olivier Sauter for saving me a lot of time by implementing his sawtooth analysis program for ASDEX Upgrade and all his support during my JET visits.

Ein große Hilfe war die Unterstützung des gesamten ASDEX Upgrade Teams durch die gute Zusammenarbeit und die Bereitschaft, alle Fragen zu beantworten.

Meinen Kolleginnen Doris Merkl, Jasmine Schirmer, Eilis Quigley und Isabel Nunes möchte ich danken für alle Unterhaltungen und Unternehmungen innerhalb und außerhalb der Fusion und natürlich meinen Kollegen Hans Meister, Thomas Pütterich, Alex Geier, Matthias Reich und Jörg Hobirk für alle fruchtbaren Diskussionen.

Nicht zuletzt möchte ich mich bei meinen Eltern und meinem Bruder bedanken, die mich während der ganzen Zeit unterstützt haben.